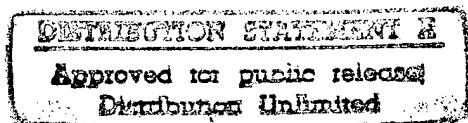


**ANNUAL PROGRESS REPORT
FOR
ONR GRANT N00014-95-1-0848**



Grant Title: Computer Simulation of Interactions Between High-Power
Electromagnetic Fields and Electronic Systems in a
Complex Environment

Institution: Center for Computational Electromagnetics
Department of Electrical and Computer Engineering
University of Illinois at Urbana-Champaign
Urbana, IL 61801-2991

Period Covered: May 1996 — April 1997

Report Title: Annual Progress Report

Principal Investigator: Jianming Jin
Telephone: (217) 244-0756
E-mail: j-jin1@uiuc.edu

19970605 158

REPORT DOCUMENTATION PAGE			FORM APPROVED OMB No. 0704-0188	
1. AGENCY USE ONLY (Leave blank)		2. REPORT DATE May 1997	3. REPORT TYPE AND DATES COVERED Annual Progress	
4. TITLE AND SUBTITLE OF REPORT Computer Simulation of Interactions Between High-Power Electromagnetic Fields and Electronic Systems in a Complex Environment			5. FUNDING NUMBERS	
6. AUTHOR(s) Jianming Jin				
7. PERFORMING ORGANIZATION NAME(S) AND ADDRESS(ES) University of Illinois Dept. of Electrical & Computer Engineering 1406 W. Green Urbana, IL 61801			8. PERFORMING ORGANIZATION REPORT NUMBER:	
9. SPONSORING/MONITORING AGENCY NAME(S) AND ADDRESS(ES) Office of Naval Research 800 N. Quincy Arlington , VA 22217- 5660			10. SPONSORING/MONITORING AGENCY REPORT NUMBER:	
11. SUPPLEMENTARY NOTES:				
12a. DISTRIBUTION AVAILABILITY STATEMENT			12b. DISTRIBUTION CODE	
13. ABSTRACT (Maximum 200 words) <p>This annual report describes our progress during the period from May 1996 to April 1997. Two tasks are described in this report. The first task xx considers the hybridization of the finite-element method (FEM) and the shooting-and-bouncing-ray (SBR) method for scattering by large bodies with small, inhomogeneous protruding scatterers, and the hybridization of the method of moments (MoM) and SBR method for w scattering from conformal slotted waveguide arrays on a large, complex platform. The second task studies a variety of finite-element and boundary-integral (FE-BI) methods for three-dimensional electromagnetic analysis. Several journal articles and conference papers supported by the research are also listed in this report.</p>				
14. SUBJECT TERMS Electromagnetic coupling, scattering, radiation, numerical methods, high-power electromagnetic field.			15. NUMBER OF PAGES: 104	
			16. PRICE CODE	
17. SECURITY CLASSIFICATION OF REPORT	18. SECURITY CLASSIFICATION OF THIS PAGE	19. SECURITY CLASSIFICATION OF ABSTRACT	20. LIMITATION OF ABSTRACT	

TABLE OF CONTENTS

Abstract	1
Progress	2
Task 1: Hybrid SBR/FEM and SBR/MoM methods for large and complex scattering problems	3
Task 2: Hybrid finite-element and boundary-integral method for electromagnetic analysis	4
Future Work	6
Publications Resulting from This Research	7
Appendix 1: Hybrid FEM/SBR method to compute scattering by large bodies with small protruding scatterers	11
Appendix 2: Scattering from a cylindrically conformal slotted- waveguide array antenna	26
Appendix 3: Hybrid MoM/SBR method to compute scattering from a slot array antenna in a complex geometry	49
Appendix 4: On the formulation of hybrid finite-element and boundary-integral method for 3D scattering	62
Appendix 5: Complementary perfectly matched layers to reduce reflection errors	81
Appendix 6: Efficient computation of electromagnetic fields in arbitrarily-shaped, inhomogeneous dielectric bodies using transpose-free QMR and FFT	92

ABSTRACT

This annual report describes our progress during the period from May 1996 to April 1997. Two tasks are described in this report. The first task considers the hybridization of the finite-element method (FEM) and the shooting-and-bouncing-ray (SBR) method for scattering by large bodies with small, inhomogeneous protruding scatterers, and the hybridization of the method of moments (MoM) and SBR method for scattering from conformal slotted waveguide arrays on a large, complex platform. The second task studies a variety of finite-element and boundary-integral (FE-BI) methods for three-dimensional electromagnetic analysis. Several journal articles and conference papers supported by the research are also listed in this report.

PROGRESS

The main goal of our proposed research is to develop numerical methods that can simulate the interaction of electromagnetic fields with complex systems in a large, complex environment. During the second year of the award, we have made significant progress toward this goal. We have worked on several tasks, which form the integral parts of the proposed research and whose successful completion is vital to the development of the proposed technique. Two of these tasks are described in detail in this report.

The first task deals with the development of two hybrid techniques to solve two different classes of electromagnetic scattering problems. The first technique combines the finite-element method (FEM) and the shooting-and-bouncing-ray (SBR) method for scattering by large bodies with small, inhomogeneous protruding scatterers. The second technique combines the method of moments (MoM) and SBR method to characterize the scattering of conformal slotted waveguide antenna arrays in a large, complex platform. This task can be considered as the further extension of the work described in Tasks 1 and 2 in the first year's annual report. It demonstrates further the power of the proposed hybrid technique for complex electromagnetic problems.

The second task studies a variety of finite-element and boundary-integral (FE-BI) methods for three-dimensional electromagnetic analysis. A new formulation is proposed, which is shown to be accurate, efficient, and immune to interior resonance corruption. This work lays a foundation for the development of a very useful and powerful technique, which combines FEM with the multilevel fast multipole method (MLFMM), for a large class of electromagnetic problems.

In addition to the two tasks described above, we have also (i) developed the concept of complementary perfectly matched layers (PML) to significantly improve the accuracy of the FEM solution (Appendix 5); (ii) developed the spectral Lanczos decomposition method (SLDM) for efficient time-domain and frequency-domain FEM solution of Maxwell's equations; (iii) applied the method of asymptotic waveform evaluation (AWE) for multi-frequency scattering analysis; and (iv) developed a new k-space method using the transpose-free quasi minimum residual (TFQMR) method and FFT for solving volume-integral equation arising from the problem of electromagnetic interaction with inhomogeneous objects such as the human body (Appendix 6).

Task 1: Hybrid SBR/FEM and SBR/MoM methods for large and complex scattering problems

Two years ago, our research group developed a hybrid technique for computing scattering by large bodies with cracks and cavities. This technique employs the shooting-and-bouncing-ray (SBR) method to compute the scattering by large bodies and uses the finite-element method (FEM) to characterize the cracks and cavities. The two methods are combined through a coupling scheme based on the electromagnetic equivalence principle and the reciprocity theorem. The coupling scheme is designed in such a manner that it includes all significant interactions between the FEM and the SBR method and it permits the SBR and FEM computations to be done separately. The resulting technique is shown to be efficient and accurate. During the first year of the award, we extended this method to the calculation of the radiation patterns of conformal antennas in a complex environment (see Task 1 of the first year's annual report). Comparison with experimental data showed that the technique can predict accurately the effect of the environment on the radiation of conformal antennas.

During the past year, we further developed a hybrid FEM/SBR method to compute scattering by large bodies with small inhomogeneous protruding scatterers, a problem that is very important, but fundamentally different from those treated before. To be more specific, we first employ the field equivalence principle to replace the protruding scatterers by a set of equivalent electric and magnetic currents. The total scattered field then becomes the superposition of the field scattered by the large body without protrusions, which is calculated using the SBR method, and the field radiated by the equivalent currents in the presence of the large body, which is also calculated using the SBR method with the aid of the reciprocity theorem. The required equivalent currents are computed using the FEM, which permits the handling of complex material composition of the protrusions. The method has been applied to two-dimensional problems, simply to demonstrate the feasibility of the proposed technique. The technical details are given in Appendix 1, which includes some very encouraging results.

In the first year's annual report, we reported our preliminary work on the analysis of cylindrically conformal waveguide slot antennas and arrays. Since then we have completed the analysis and studied the scattering properties of a variety of conformal waveguide slot antennas and arrays (Appendix 2). Furthermore, we have combined the method of analysis

with the SBR method to compute scattering from conformal waveguide slot antennas and arrays in a complex geometry. This extension is important because almost all conformal antennas and arrays are placed on a complex geometry in practice and their scattering characterization is critical for applications such as target identification. The technical details are given in Appendix 3.

Task 2: Hybrid finite-element and boundary-integral method for electromagnetic analysis

In our originally proposed research, we planned to develop hybrid techniques to combine a high-frequency asymptotic method with a numerical method to simulate the interaction of electromagnetic fields with complex systems in a large, complex platform. To date, we have successfully developed several such techniques as described in Task 1 of the first year's annual report and in the Task 1 of this report. Because of the use of the high-frequency method, the source of the electromagnetic fields must be far away from the platform, which is the case for many practical problems. However, there is another class of important problems which involve sources near or on the platform, such as the problem of mutual coupling between two antennas on the same platform and the interaction of a radiating source with a system on the same body. Such a problem cannot be analyzed by the method proposed in this research. We decided to go beyond the originally proposed plan and develop a technique for this class of problems.

The technique which is to be developed combines FEM with the multilevel fast multipole method (MLFMM). It is based on the finite-element and boundary-integral (FE-BI) method pioneered by the PI. The FE-BI method first divides the problem into an interior and exterior problems. The field in the interior region is formulated using FEM, and the field in the exterior region is represented by a boundary-integral equation (BIE). The interior and exterior fields are then coupled by the field continuity conditions. Although the FE-BI method is remarkably more powerful than other numerical techniques in dealing with complex problems, it still has a bottleneck which is the full matrix generated by BIE. This bottleneck severely limits the capability of the FE-BI method in dealing with large problems. Our objective is to apply MLFMM to BIE to completely remove the bottleneck in the FE-BI method for general 3D problems. The first step is to study a variety of FE-BI formulations and identify the most accurate and efficient one.

During the past year, we studied in detail a variety of formulations for the hybrid FE-BI method for 3D electromagnetic scattering by inhomogeneous objects. It is shown that the efficiency and accuracy of the FE-BI method depend highly on the formulation and discretization of the BIE used. A simple analysis of matrix condition identifies the efficiency of the different FE-BI formulations and an analysis of weighting functions shows that the traditional FE-BI formulations cannot produce accurate solutions. A new formulation is then proposed and numerical results show that the resulting solution has a good efficiency and accuracy and is completely immune to the problem of interior resonance. The technical details are given in Appendix 4.

FUTURE WORK

In the coming year, we plan to focus our effort on the development of the FEM/MLFMM for fast and accurate analysis of conformal antennas and other electromagnetic devices on a large, complex platform. Such a technique is urgently needed for many applications, such as EMP due to nearby sources, design of special-purpose antennas taking into consideration of the environment/platform, and characterization of mutual coupling between two antennas on a large, complex body. Currently, MLFMM has been implemented only for conducting and impedance surfaces, both of which contain only one type of integral operator. Its application to the proposed work requires the treatment of two different types of integral operators. In addition, we also plan to develop fast solvers based on the spectral Lanczos decomposition method (SLDM) and the method of asymptotic waveform evaluation (AWE) for the FEM analysis.

PUBLICATIONS RESULTING FROM THIS RESEARCH

Journal articles (published or accepted)

- [1] N. Lu and J. M. Jin, "Application of fast multipole method to finite element-boundary integral solution of scattering problems," *IEEE Trans. Antennas Propagat.*, vol. AP-44, no. 6, pp. 781-786, 1996.
- [2] J. M. Jin, J. A. Berrie, R. Kipp, and S. W. Lee, "Calculation of radiation patterns of microstrip antennas on cylindrical bodies of arbitrary cross section," *IEEE Trans. Antennas Propagat.*, vol. AP-45, no. 1, pp. 126-132, Jan. 1997.
- [3] W. C. Chew and J. M. Jin, "Perfectly matched layers in the discretized space: An analysis and optimization," *Electromagnetics*, vol. 16, no. 4, pp. 325-340, July 1996.
- [4] J. M. Jin and W. C. Chew, "Combining PML and ABC for finite element analysis of scattering problems," *Microwave Opt. Tech. Lett.*, vol. 12, no. 4, pp. 192-197, July 1996.
- [5] G. Fan and J. M. Jin, "Scattering from a cylindrically conformal slotted-waveguide array antenna," *IEEE Trans. Antennas Propagat.*, 1997, in press.
- [6] A. D. Greenwood, S. S. Ni, J. M. Jin, and S. W. Lee, "Hybrid FEM/SBR method to compute the radiation pattern from a microstrip patch antenna in a complex geometry," *Microwave Opt. Tech. Lett.*, vol. 13, no. 2, pp. 84-87, Oct. 1996.
- [7] J. M. Jin and N. Lu, "The unimoment method applied to elliptic boundaries," *IEEE Trans. Antennas Propagat.*, vol. AP-45, no. 3, pp. 564-566, Mar. 1997.
- [8] J. M. Jin, X. Q. Sheng, and W. C. Chew, "Complementary perfectly matched layers to reduce reflection errors," *Microwave Opt. Tech. Lett.*, vol. 14, no. 5, pp. 284-287, Apr. 1997.

[9] F. Ling and J. M. Jin, "Hybridization of SBR and MoM for scattering by large bodies with inhomogeneous protrusions—Summary," *Journal of Electromagnetic Waves and Applications*, in press.

[10] F. Ling and J. M. Jin, "Hybridization of SBR and MoM for scattering by large bodies with inhomogeneous protrusions," *Progress in Electromagnetics Research*, PIER 17, in press.

[11] X. Sheng and J. M. Jin, "Hybrid FEM/SBR method to compute scattering by large bodies with small protruding scatterers," *Microwave Opt. Tech. Lett.*, in press.

[12] M. Zunoubi, J. M. Jin, W. C. Chew, and D. Kennedy, "A spectral Lanczos decomposition method for solving axisymmetric low-frequency electromagnetic diffusion by the finite-element method," *Journal of Electromagnetic Waves and Applications*, in press.

Journal articles (submitted)

[1] J. M. Jin and N. Lu, "Finite element analysis of scattering using coupled basis functions for elliptic boundaries," submitted to *Proc. Inst. Elec. Eng., part H*, 1996.

[2] C. F. Wang and J. M. Jin, "Simple and efficient computation of electromagnetic fields in arbitrarily-shaped, inhomogeneous dielectric bodies using transpose-free QMR and FFT," submitted to *IEEE Trans. Microwave Theory Tech*, 1996.

[3] M. Zunoubi, J. M. Jin, K. Donepudi, and W. C. Chew, "A spectral Lanczos decomposition method for solving 3D low-frequency electromagnetic diffusion by the finite-element method," *IEEE Trans. Antennas Propagat.*, submitted for publication, 1997.

[4] X. Q. Sheng, J. M. Jin, J. M. Song, C. C. Lu, and W. C. Chew, "On the formulation of hybrid finite-element and boundary-integral method for 3D scattering," *IEEE Trans. Antennas Propagat.*, submitted for publication, 1997.

Conference papers

- [1] J. M. Jin, X. Q. Sheng, and W. C. Chew, "Complementary perfectly matched layers for use as an absorbing boundary condition," Progress in Electromagnetic Research Symposium, Hong Kong, Jan. 1997.
- [2] M. Zunoubi, J. M. Jin, and W. C. Chew, "The spectral Lanczos decomposition method for solving low-frequency electromagnetic diffusion by the finite elements method," The 13th Annual Review of Progress in Applied Computational Electromagnetics, Monterey, CA, 1997.
- [3] A. D. Greenwood and J. M. Jin, "Hybrid MoM/SBR method to compute scattering from a slot array antenna in a complex geometry," The 13th Annual Review of Progress in Applied Computational Electromagnetics, Monterey, CA, 1997.
- [4] J. M. Jin, J. Chen, W. C. Chew, R. L. Magin, and P. J. Dimbylow, "3D electromagnetic modeling for high-frequency MRI applications," International Society for Magnetic Resonance in Medicine Fifth Scientific Meeting, Vancouver, Canada, April 1997.
- [5] F. Ling, X. Q. Sheng, and J. M. Jin, "Hybrid MoM/SBR and FEM/SBR methods for scattering by large bodies with inhomogeneous protrusions," The 1997 IEEE Antennas and Propagation Society International Symposium, Montreal, Canada, 1997.
- [6] C. F. Wang and J. M. Jin, "Efficient computation of electromagnetic fields in arbitrarily-shaped, inhomogeneous dielectric bodies using transpose-free QMR and FFT," The 1997 IEEE Antennas and Propagation Society International Symposium, Montreal, Canada, 1997.
- [7] J. Chen and J. M. Jin, "Calculation of SAR and B1-Field within human head excited by MRI birdcage coils," The 1997 IEEE Antennas and Propagation Society International Symposium, Montreal, Canada, 1997.
- [8] J. M. Song, X. Q. Sheng, C. C. Lu, W. C. Chew, and J. M. Jin, "Fast multipole method for large penetrable scatterers," The 1997 URSI Radio Science Meeting, Montreal, Canada, 1997.

- [9] M. Zunoubi, J. M. Jin, and W. C. Chew, "The spectral Lanczos decomposition method for solving 3-D low-frequency electromagnetic diffusion by the finite elements method," The 1997 URSI Radio Science Meeting, Montreal, Canada, 1997.
- [10] A. D. Greenwood and J. M. Jin, "Hybrid MoM/SBR method to compute scattering from a slot array in a complex geometry," The 1997 URSI Radio Science Meeting, Montreal, Canada, 1997.
- [11] J. M. Jin, G. X. Fan, C. C. Lu, J. M. Song, and W. C. Chew, "A hybrid SBR/MoM technique for analysis of scattering from small protrusions on a large conducting surface," Progress in Electromagnetic Research Symposium, Ridgefield, CT, July 1997.

APPENDIX 1

Hybrid FEM/SBR Method to Compute Scattering by Large Bodies with Small Protruding Scatterers

X. Q. Sheng and J. M. Jin

Center for Computational Electromagnetics

Department of Electrical and Computer Engineering

University of Illinois at Urbana-Champaign

Urbana, Illinois 61801-2991, USA

Abstract—A hybrid method that combines the finite-element method (FEM) and the shooting-and-bouncing-ray (SBR) method is presented to compute scattering by large bodies with small protruding scatterers. In the method, the field equivalence principle is employed to replace the protruding scatterers by a set of equivalent electric and magnetic currents. The total scattered field then becomes the superposition of the field scattered by the large body without protrusions, which is calculated using the SBR method, and the field radiated by the equivalent currents in the presence of the large body, which is also calculated using the SBR method with the aid of the reciprocity theorem. The required equivalent currents are computed using the FEM, which permits the handling of complex material composition of the protrusions. Two-dimensional examples are presented to demonstrate the feasibility of the proposed method.

I. INTRODUCTION

Recently, a hybrid technique was developed for computing scattering by large bodies with cracks and cavities [1]. This technique employs the shooting-and-bouncing-ray (SBR) method to compute the scattering by large bodies and uses the finite-element method (FEM) to characterize the cracks and cavities. The two methods are combined through a coupling scheme based on the electromagnetic equivalence principle and the reciprocity theorem. The coupling scheme is designed in such a manner that it includes all significant interactions between the FEM and the SBR method and it permits the SBR and FEM computations to be done separately. The resulting technique is shown to be efficient and accurate and, because of this, it is extended to the calculation of the radiation patterns of conformal antennas in a complex environment [2].

The hybrid FEM/SBR method summarized above belongs to a larger class of hybrid method pioneered by Thiele *et al.* [3]–[11]. A common feature in these methods is that they combine a high-frequency asymptotic technique, such as the geometrical optics (GO), physical optics (PO), or geometrical theory of diffraction (GTD), with a low-frequency numerical technique, such as the method of moments (MoM), FEM, or finite-difference method (FDM). They are specifically designed to tackle three types of problems that cannot be handled accurately and efficiently by either a high-frequency method or a low-frequency method. The first type includes scatterers with a size in the intermediate region between the high and low frequencies [7]–[11]. The second type is the scattering by small objects in the presence of large bodies [3]–[6]. The third type is the scattering by large bodies having small indenting structures such as cracks, gaps, and cavities [1], [2].

In this article, we extend the hybrid FEM/SBR method, developed originally for the third type of problem, to compute scattering by large bodies with small protruding scatterers, a problem that belongs the second type. To be more specific, we first employ the field equivalence principle to replace the protruding scatterers by a set of equivalent electric and magnetic currents. The total scattered field then becomes the superposition of the field scattered by the large body without

protrusions, which is calculated using the SBR method, and the field radiated by the equivalent currents in the presence of the large body, which is also calculated using the SBR method with the aid of the reciprocity theorem. The required equivalent currents are computed using the FEM, which permits the handling of complex material composition of the protrusions. In this article, the formulation and analysis are described for two-dimensional problems, simply to demonstrate the feasibility of the proposed technique.

II. FORMULATION

Consider the problem of wave scattering by a large, perfectly conducting body with a small protruding structure, whose cross-section is illustrated in Fig. 1. The protruding structure can be a perfect conductor or a dielectric/magnetic material or a combination of these. In accordance with the field equivalence principle [12], the protrusion can be removed and its effect in the exterior region can be represented by a set of equivalent electric and magnetic currents on the surface of the protrusion. The equivalent electric and magnetic currents are related to the electric and magnetic fields by

$$\mathbf{J}_s = \hat{n} \times \mathbf{H}, \quad \mathbf{M}_s = \mathbf{E} \times \hat{n} \quad (1)$$

where \hat{n} denotes the outward unit vector normal to the surface of the protrusion. Apparently, the original problem becomes the two equivalent subproblems, depicted in Fig. 2. The first is the scattering by the large body without the protrusion and the second is the radiation of the equivalent currents in the presence of the large body. Whereas the field scattered by the large body without the protrusion can be calculated efficiently and accurately using the SBR method [13]–[15], the calculation of the equivalent currents and their radiation is more involved. In the proposed method, the currents are calculated using the FEM in conjunction with an absorbing boundary condition (ABC) and the radiation is calculated using the SBR method with the aid of the reciprocity theorem. These are discussed below in more detail.

To use the FEM with an ABC to calculate the equivalent electric and magnetic currents, we first enclose the protrusion in a larger artificial surface denoted as Γ_a (see Fig. 3). We then apply the second-order ABC [16] to the scattered field on Γ_a :

$$\frac{\partial \phi^{sca}}{\partial n} = \alpha \phi^{sca} + \beta \frac{\partial^2 \phi^{sca}}{\partial s^2} \quad (2)$$

where $\phi = E_z$ for transverse magnetic (TM) or E_z -polarization, $\phi = H_z$ for transverse electric (TE) or H_z -polarization, \hat{n} denotes the outward unit vector normal to Γ_a , s is the arc length measured along Γ_a , and

$$\alpha = -jk_0 - \frac{\kappa}{2} + \frac{j\kappa^2}{8(j\kappa - k_0)}, \quad \beta = \frac{j}{2(j\kappa - k_0)} \quad (3)$$

where $\kappa(s)$ is the curvature of Γ_a at s . Since the field (ϕ^{sca}) scattered by the protrusion can be considered as the difference between the total field (ϕ) and the incident field in the presence of the large body (ϕ^{sbr}), the ABC can be written as

$$\frac{\partial \phi}{\partial n} - \alpha \phi - \beta \frac{\partial^2 \phi}{\partial s^2} = q \quad (4)$$

where

$$q = \frac{\partial \phi^{sbr}}{\partial n} - \alpha \phi^{sbr} - \beta \frac{\partial^2 \phi^{sbr}}{\partial s^2}. \quad (5)$$

This boundary condition, together with the Helmholtz equation satisfied by ϕ inside Γ_a , defines a unique boundary-value problem, which can be solved using the FEM [16]. Once ϕ inside Γ_a is found, the equivalent electric and magnetic currents on the surface of the protrusion can be obtained using their definition in (1). Note that in (5), ϕ^{sbr} is calculated using the SBR method.

Once the equivalent currents are calculated, their radiated field in the presence of the large body can be calculated using the SBR method with the aid of the reciprocity theorem [1], [2], [17]. To be more specific, for the TM polarization, we place an infinitely long current filament J_0 at the observation point ρ_o . If ρ_o is far from the origin, the free space electric field radiated by this current is given by

$$E'_z(\rho) = -\eta_0 J_0 \sqrt{\frac{jk_0}{8\pi\rho_o}} e^{-jk_0\rho_o} e^{jk_0(x \cos \theta + y \sin \theta)} \quad (6)$$

where η_0 is the free-space intrinsic impedance. Apparently, if we choose

$$J_0 = -\frac{1}{\eta_0} \sqrt{\frac{8\pi\rho_o}{jk_0}} e^{jk_0\rho_o}, \quad (7)$$

$E'_z(\rho)$ then becomes a plane wave incident from the direction of the observation point. If the current filament is placed at the observation point in the presence of the large body without the protrusion, the field can be calculated conveniently using the SBR method. Using the reciprocity theorem, the field radiated by the equivalent currents is then given by

$$E_z^{sca}(\rho) = \frac{1}{J_0} \int_{\Gamma_b} (E_z^{sbr} J_z - H_t^{sbr} M_t) dl \quad (8)$$

where Γ_b denotes the surface of the protrusion, E_z^{sbr} and H_t^{sbr} are the field due to the current filament and are calculated using the SBR method. Similarly, for the TE polarization, the field radiated by the equivalent currents is given by

$$H_z^{sca}(\rho) = \frac{1}{M_0} \int_{\Gamma_b} (H_z^{sbr} M_z - E_t^{sbr} J_t) dl \quad (9)$$

where M_0 is given by

$$M_0 = -\eta_0 \sqrt{\frac{8\pi\rho_o}{jk_0}} e^{jk_0\rho_o}. \quad (10)$$

Note that in the formulation described above, because of the use of an ABC on Γ_a , we neglected the field scattered by the protrusion, reflected and/or diffracted back to the protrusion by the large body, and scattered by the protrusion again. In most problems, this contribution is insignificant. However, when the protrusion is very close to edges and reflecting surfaces, the contribution can become significant and its omission can cause a substantial error in the solution. When this happens, we can use either PO or the SBR method to calculate the field radiated by the equivalent currents and reflected and/or diffracted back to the protrusion. Using this as the secondary incident field, we can update the equivalent currents. This process can be repeated until there is no significant change in the values of the equivalent currents. The field radiated by the currents is then calculated using either (8) or (9).

III. NUMERICAL RESULTS

In this section, we present several examples to demonstrate the validity of the hybrid method described above.

The first example is a circular cylinder with a small conducting protrusion. The radius of the circular cylinder is 5λ and the protrusion is 1λ wide and 1λ high. The monostatic radar cross section (RCS) is given in Fig. 4. As can be seen, the hybrid solution is in good agreement with the MoM solution [18]. In the calculation, the absorbing boundary is placed 0.5λ away from the surface of the protrusion.

The second example is a $16\lambda \times 8\lambda$ rectangular conducting cylinder having a conducting protrusion on its upper surface. The protrusion is 0.8λ wide and 0.8λ high. The monostatic RCS is shown in Fig. 5 and compared to the MoM solution. The accuracy here is slightly worse than that in the first example, and this degradation is due to the error in the PO solution of the scattered field.

The third example, shown in Fig. 6, places a conducting protrusion at the corner of the rectangular cylinder. Again, reasonably good agreement is obtained. Therefore, the method is not limited to the protrusions placed on a locally flat surface.

The last example is an L-shaped conducting body with a protrusion on the surface. This problem differs from the former ones in that both incident and scattered fields can have multiple bounces. The hybrid solution obtained without iteration is given in Fig. 7, from which a noticeable error is observed. This is expected because the protrusion is close to the reflecting surface. The results obtained using the iterative approach are also shown in Fig. 7, which demonstrate clearly the improvement achieved by the iterative approach.

IV. CONCLUSION

In this article, we presented the hybrid FEM/SBR method to compute scattering by large bodies with small protruding scatterers. We first employed the field equivalence principle to replace the protruding scatterers by a set of equivalent electric and magnetic currents. We then used the SBR method to calculate the field scattered by the large body without protrusions and the FEM to compute the equivalent currents. The field radiated by the equivalent currents was also calculated using the SBR method with the aid of the reciprocity theorem and was superimposed to the field scattered by the large body. Two-dimensional problems were given to demonstrate the feasibility of the proposed technique. Its extension to the three-dimensional space is straightforward.

Acknowledgment

This work was supported by the Office of Naval Research under grant N00014-95-1-0848 and the National Science Foundation under grant NSF ECE 94-57735, and by a grant from AFOSR via the MURI Program under contract number F49620-96-1-0025.

References

- [1] J. M. Jin, S. S. Ni, and S. W. Lee, "Hybridization of SBR and FEM for scattering by large bodies with cracks and cavities," *IEEE Trans. Antennas Propagat.*, vol. 43, pp. 1130-1139, Oct. 1995.
- [2] A. D. Greenwood, S. S. Ni, J. M. Jin, and S. W. Lee, "Hybrid FEM/SBR method to compute the radiation pattern from a microstrip patch antenna in a complex geometry," *Microwave Opt. Technol. Lett.*, vol. 13, pp. 84-87, Oct. 1996.
- [3] G. A. Thiele and T. H. Newhouse, "A hybrid technique for combining moment methods with the geometrical theory of diffraction," *IEEE Trans. Antennas Propagat.*, vol. 23, pp. 62-69, Jan. 1975.

- [4] E. P. Ekelman and G. A. Thiele, "A hybrid technique for combining moment method treatment of wire antennas with the GTD for the curved surfaces," *IEEE Trans. Antennas Propagat.*, vol. 28, pp. 813-839, Nov. 1980.
- [5] L. W. Henderson and G. A. Thiele, "A hybrid MM-GTD technique for treatment of wire antennas near a curved surfaces," *Radio Sci.*, vol. 16, pp. 1125-1130, 1981; Also, related paper in *IEEE Trans. Antennas Propagat.*, vol. 30, pp. 1257-1261, Apr. 1982.
- [6] M. Hsu and P. H. Pathak, "Hybrid analysis (MM-UTD) of EM scattering from finned convex objects," *1995 IEEE AP-S Int. Symp. Dig.*, vol. 3, pp. 1456-1459, June 1995.
- [7] W. D. Burnside, C. L. Yu, and R. J. Marhefka, "A technique to combine the geometrical theory of diffraction and the moment method," *IEEE Trans. Antennas Propagat.*, vol. AP-23, pp. 551-557, July 1975.
- [8] L. N. Medgyesi-Mitschang and D. S. Wang, "Hybrid solutions for scattering from perfectly conducting bodies of revolution," *IEEE Trans. Antennas Propagat.*, vol. AP-31, pp. 570-583, July 1983.
- [9] D. S. Wang, "Current-based hybrid analysis for surface-wave effects on large scatterers," *IEEE Trans. Antennas Propagat.*, vol. 39, pp. 839-849, June 1991.
- [10] U. Jakobus and F. M. Landstorfer, "Improved PO-MM hybrid formulation for scattering from three-dimensional perfectly conducting bodies of arbitrary shape," *IEEE Trans. Antennas Propagat.*, vol. 43, pp. 162-169, Feb. 1995.
- [11] F. Obelleiro-Basteiro, J. L. Rodriguez, and R. J. Burkholder, "An iterative physical optics approach for analyzing the electromagnetic scattering by large open-ended cavities," *IEEE Trans. Antennas Propagat.*, vol. 43, pp. 356-362, Apr. 1995.
- [12] R. F. Harrington, *Time-Harmonic Electromagnetic Fields*. New York: McGraw-Hill, 1961.

- [13] H. Ling, R. C. Chou, and S. W. Lee, "Rays versus modes: Pictorial display of energy flow in an open-ended waveguide," *IEEE Trans. Antennas Propagat.*, vol. AP-35, pp. 605-607, May 1987.
- [14] H. Ling, R. C. Chou, and S. W. Lee, "Shooting and bouncing rays: calculating the RCS of an arbitrary shaped cavity," *IEEE Trans. Antennas Propagat.*, vol. AP-37, pp. 194-205, Feb. 1989.
- [15] J. Baldauf, S. W. Lee, L. Lin, S. K. Jeng, S. M. Scarborough, and C. L. Yu, "High frequency scattering from trihedral corner reflectors and other benchmark targets: SBR vs. experiments," *IEEE Trans. Antennas Propagat.*, vol. AP-39, pp. 1345-1351, Sept. 1991.
- [16] J. M. Jin, *The Finite Element Method in Electromagnetics*. New York: Wiley, 1993.
- [17] P. H. Pathak, R. J. Burkholder, "A reciprocity formulation for the EM scattering by an obstacle within a large open cavity," *IEEE Trans. Antennas Propagat.*, vol. 41, pp. 702-707, Apr. 1993.
- [18] J. M. Jin and V. V. Liepa, "Simple moment method program for computing scattering from complex cylindrical obstacles," *Proc. Inst. Elec. Eng.*, part H, vol. 136, no. 4, pp. 321-329, Aug. 1989.

FIGURE CAPTIONS

- Fig. 1** Original problem: A large PEC body with a small protrusion.
- Fig. 2** Equivalent problem: The protrusion is replaced by equivalent electric and magnetic currents.
- Fig. 3** Region for FEM calculation: The protrusion is enclosed in an artificial boundary.
- Fig. 4** Comparison of the monostatic RCS calculated by the hybrid SBR/FEM and the MoM for a circular cylinder with a conducting protrusion.
- Fig. 5** Comparison of the monostatic RCS calculated by the hybrid SBR/FEM and the MoM for a rectangular cylinder with a conducting protrusion.
- Fig. 6** Comparison of the monostatic RCS calculated by the hybrid SBR/FEM and the MoM for a rectangular cylinder with a conducting protrusion at the corner.
- Fig. 7** Comparison of the monostatic RCS calculated by the hybrid SBR/FEM and the MoM for an L-shaped cylinder with a conducting protrusion.

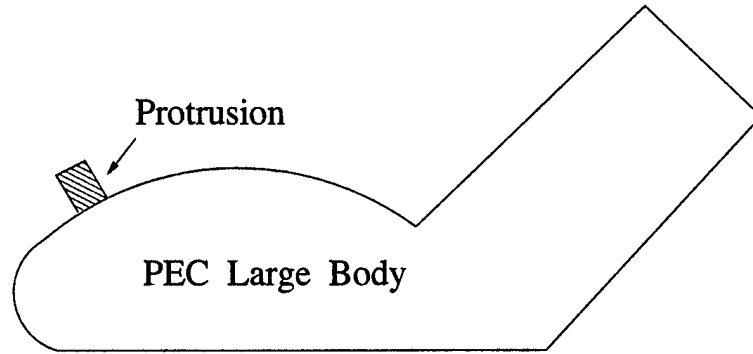


Figure 1: Original problem: A large PEC body with a small protrusion.

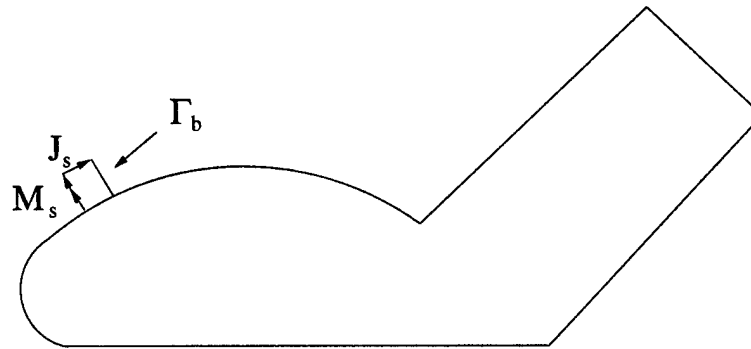


Figure 2: Equivalent problem: The protrusion is replaced by equivalent electric and magnetic currents.

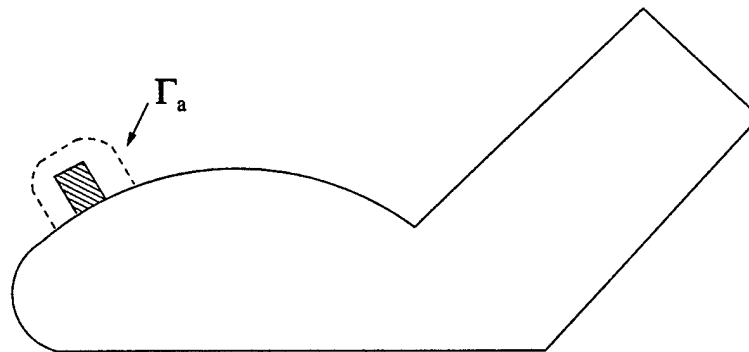


Figure 3: Region for FEM calculation: The protrusion is enclosed in an artificial boundary.

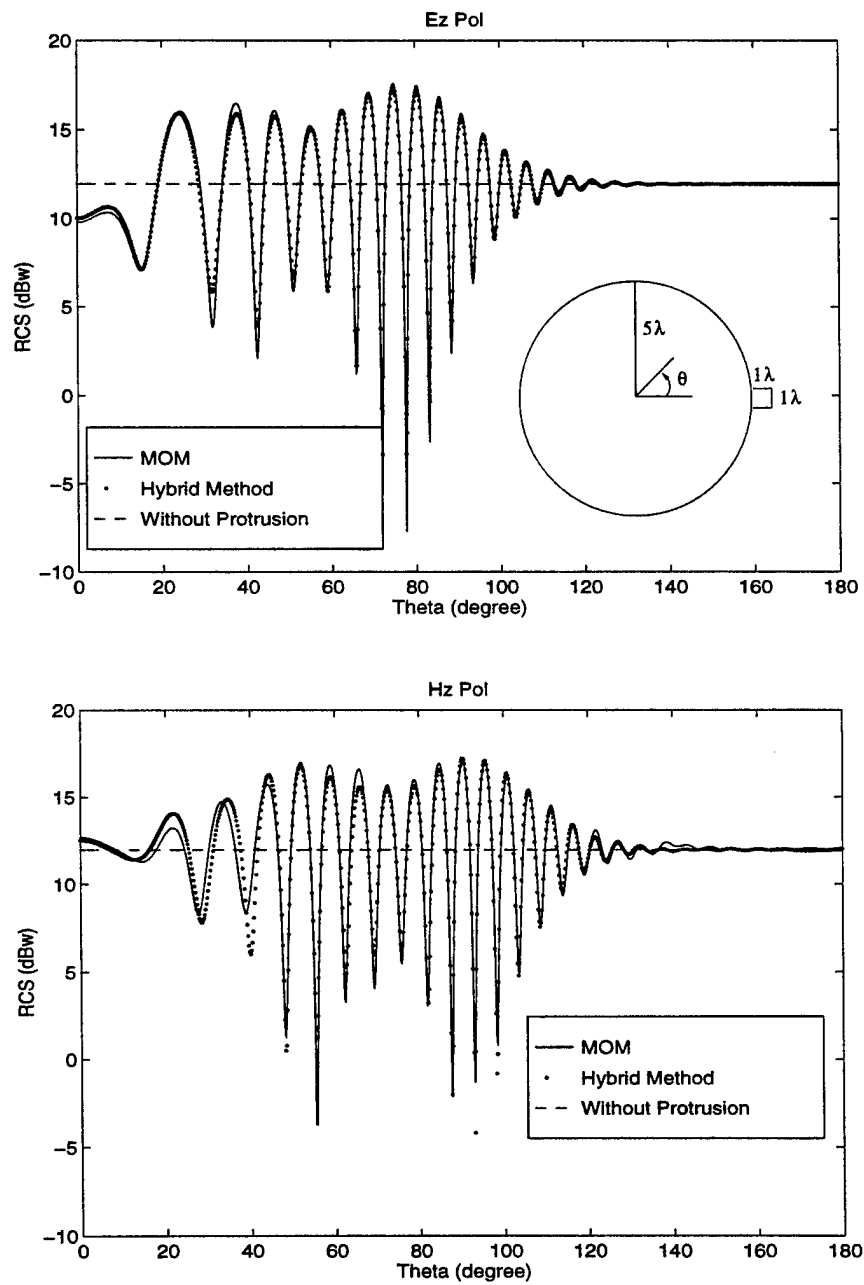


Figure 4: Comparison of the monostatic RCS calculated by the hybrid SBR/FEM and the MoM for a circular cylinder with a conducting protrusion.

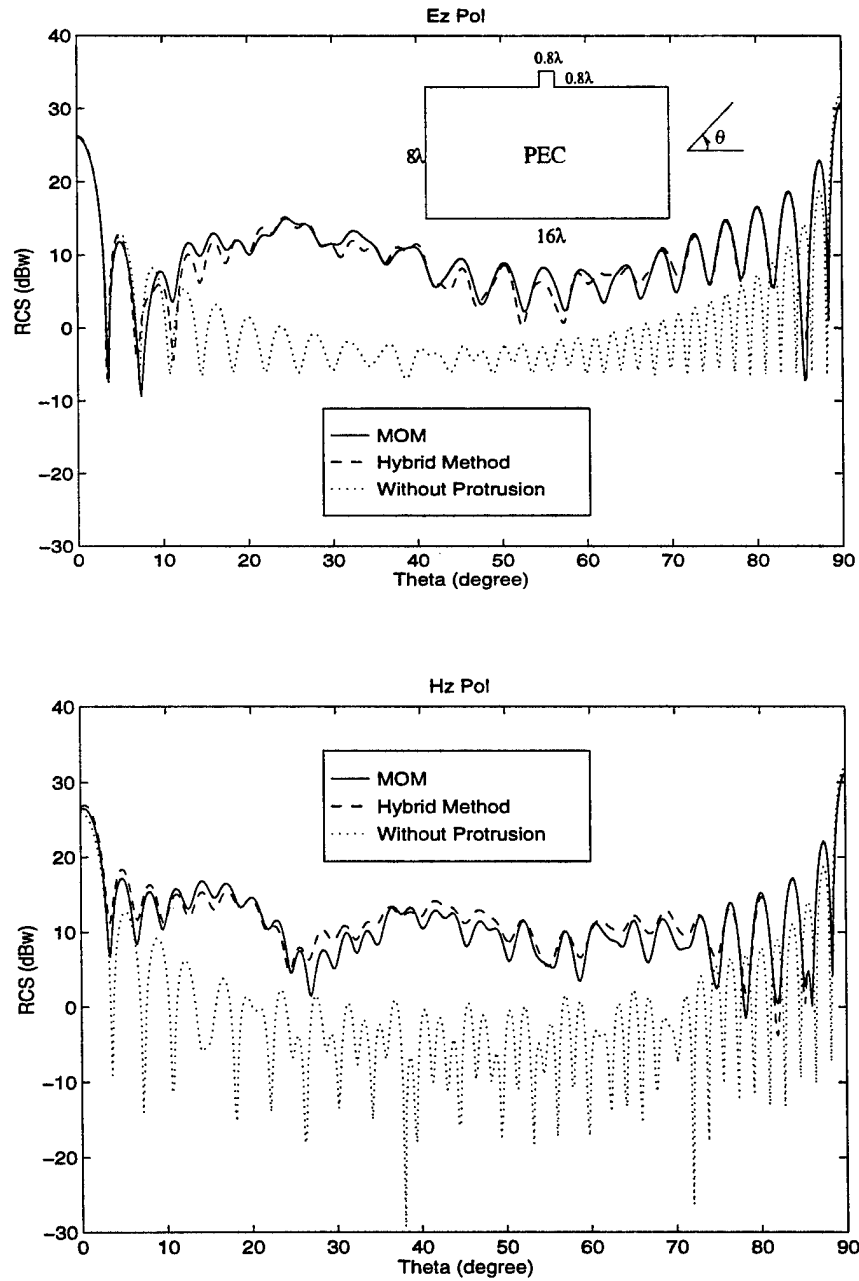


Figure 5: Comparison of the monostatic RCS calculated by the hybrid SBR/FEM and the MoM for a rectangular cylinder with a conducting protrusion.

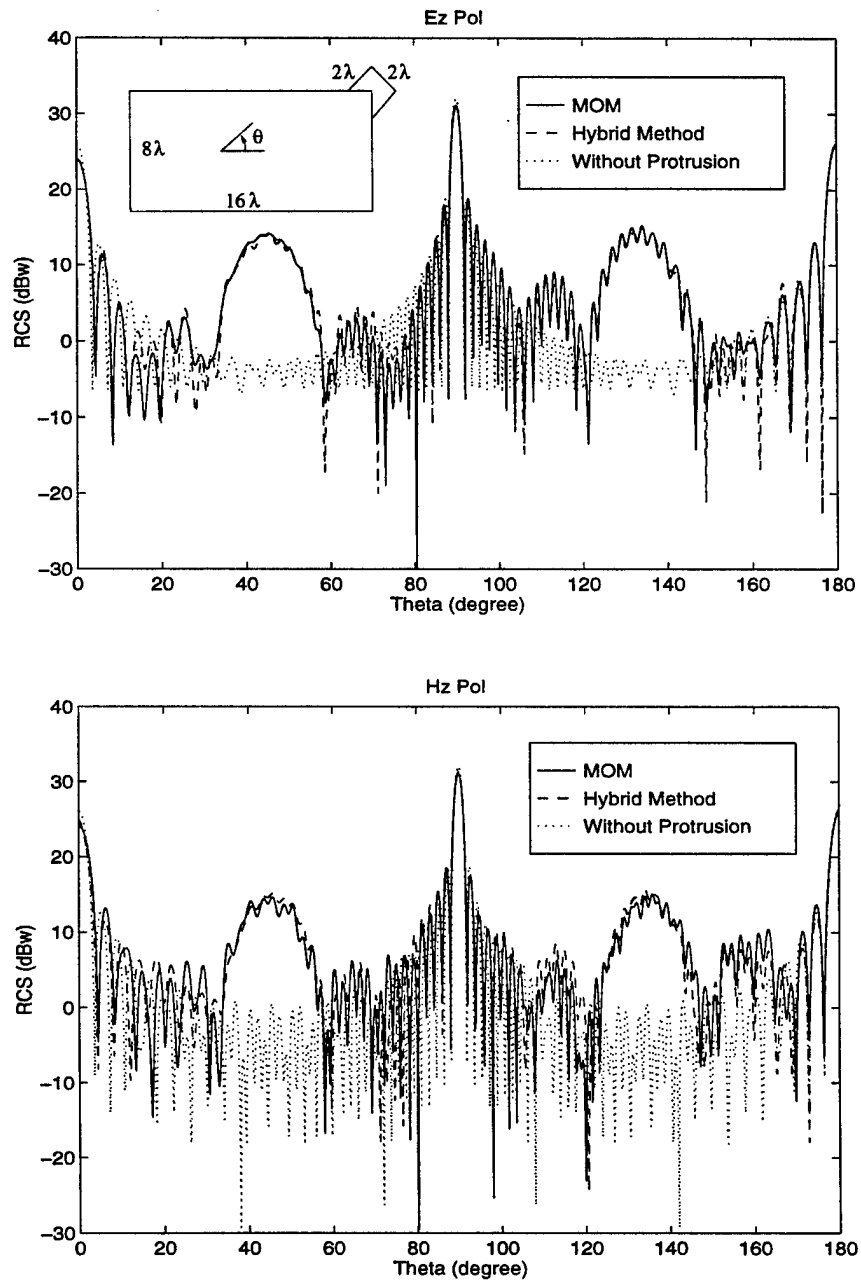


Figure 6: Comparison of the monostatic RCS calculated by the hybrid SBR/FEM and the MoM for a rectangular cylinder with a conducting protrusion at the corner.

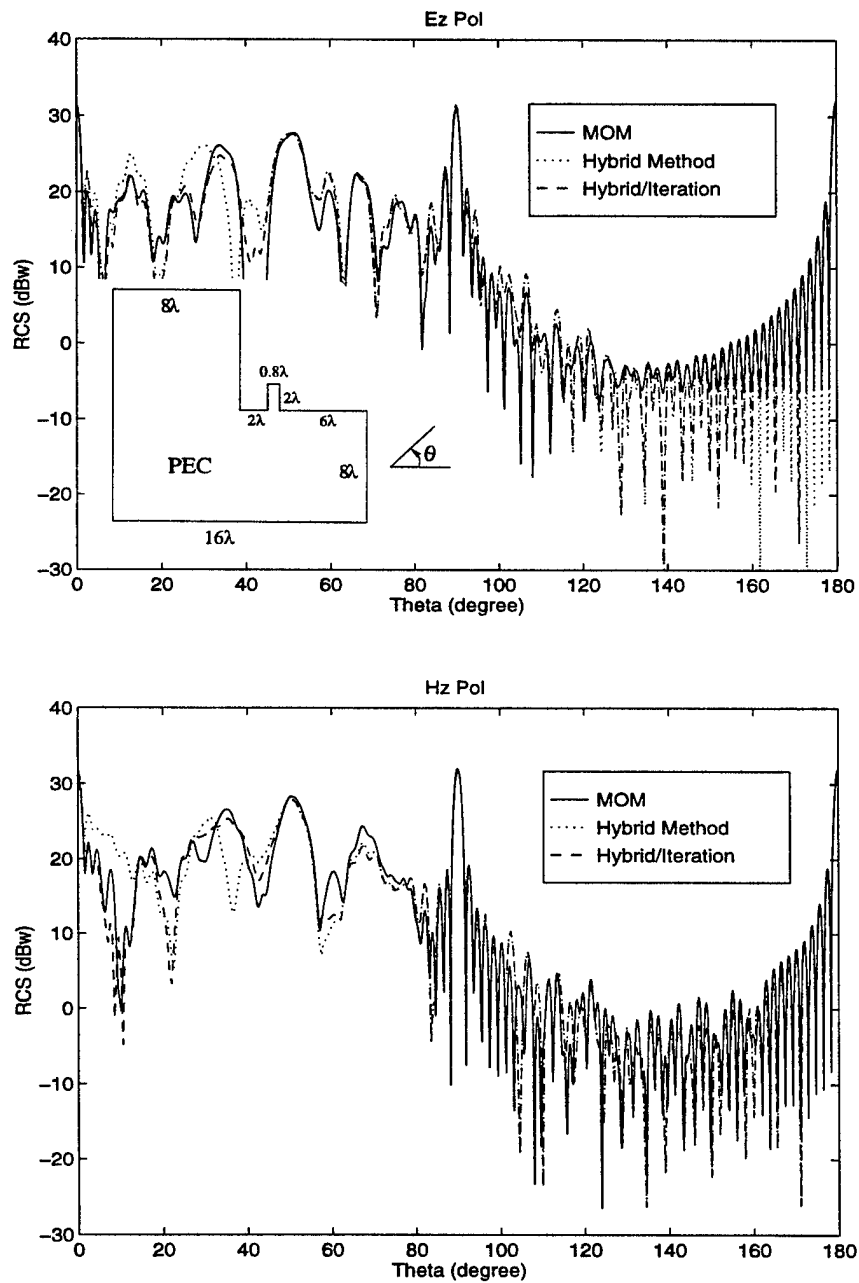


Figure 7: Comparison of the monostatic RCS calculated by the hybrid SBR/FEM and the MoM for an L-shaped cylinder with a conducting protrusion.

APPENDIX 2

SCATTERING FROM A CYLINDRICALLY CONFORMAL SLOTTED-WAVEGUIDE ARRAY ANTENNA

Guo-Xin Fan and Jian-Ming Jin
Electromagnetics Laboratory
Department of Electrical and Computer Engineering
University of Illinois at Urbana-Champaign
Urbana, Illinois 61801-2991

ABSTRACT

A numerical method is developed to investigate electromagnetic scattering by a cylindrically conformal waveguide-fed slot array. The problem is first formulated in terms of integral equations using the equivalence principle. The integral equations are then solved using the method of moments (MoM) in conjunction with global sinusoidal basis functions and Galerkin's testing procedure. The MoM solution requires the evaluation of the generalized admittance matrices involving various dyadic Green's functions. The slow convergence of the series associated with the summation of waveguide modes is accelerated using the Kummer transformation and the slow convergence of the series associated with the summation of the exterior modes is avoided by using the asymptotic solutions with proper treatment for singular integrals. The evaluation of the excitation vector and scattered field is also accelerated using Watson's transformation and asymptotic solutions. Numerical results are presented to illustrate the scattering characteristics of the cylindrically conformal waveguide-fed slot arrays, such as the effects of curvature, slot thickness, and waveguide termination on the radar cross section of the arrays.

This work was supported by the Office of Naval Research under the grant N00014-95-1-0848, NASA under the grant NAG3-1474, the National Science Foundation under grant NSF ECE 94-57735, and a grant from AFOSR via the MURI Program under contract number F49620-96-1-0025.

I. INTRODUCTION

Slotted-waveguide array antennas are widely used on modern airborne radars because of their large power handling capability, high efficiency, light weight, compact structure, and low side lobes. However, being highly efficient radiating structures, by the reciprocity theorem these antennas are also efficient scatterers, which contribute significantly to the overall radar cross section (RCS) of the host vehicle. Usual RCS reduction techniques cannot be applied to these antennas without degrading their performance. Bandpass radomes, made of frequency selective surfaces (FSS), can reflect nearly all the incident energy outside the working frequency band and allow the incident energy within the working frequency band pass through to reach the antennas. However, it is at the working frequency band that the slot arrays have a significantly higher RCS. Therefore, it is necessary to predict the RCS of the slot arrays for applications such as target identification, electromagnetic compatibility, and stealth technology.

Because of a large number of slots and the mutual coupling between the slots through the waveguides and exterior space, a full-wave analysis of slotted waveguide arrays is very difficult. In the past, most work was focused on the radiation analysis of a single slot [1]-[10], one-dimensional arrays and small two-dimensional arrays [11]-[17], all in a planar surface. In particular, Stevenson [1] developed what is now considered the classical theory for a single slot and Oliner [2] presented a variational solution of the problem. Khac and Carson [3] employed the method of moments (MoM) to seek a numerical solution to the slot field using pulse basis functions and point match technique. The efficiency of the MoM solution was improved by Lyon and Sangster [5] and Stern and Elliott [6] by using global and piecewise sinusoidal basis functions and Galerkin's technique. The MoM was also applied to tilted slots [9], dielectric-covered slots [8], [10], edge slots [18], and slots in a sectoral waveguide [19]. Recently, Fan [20] analyzed cylindrically conformal slotted-waveguide array antennas with a curved waveguide as the feeding guide and sectoral guides as the radiating guides. Whereas the literature for the radiation analysis of the slot arrays is abundant, little work was done on the scattering from the planar slot antennas [21]-[23], let alone the curved ones. Josefsson [21] analyzed scattering by a single slot in an infinitely long waveguide and Chen and Jin [23] developed the MoM and finite element method (FEM) solutions for the slots in the waveguides terminated with arbitrary loads. No work was found on the analysis of the scattering characteristics of slotted waveguide arrays on a curved surface. In this paper, we present such an analysis.

The key problem in the analysis of slotted waveguide arrays is to solve for the slot aperture fields. Among various numerical methods, the MoM is most efficient and accurate for this

purpose because only a small number of basis functions are needed to represent the aperture fields. However, the major difficulties in the MoM are (i) its formulation requires the dyadic Green's functions for the waveguide, the exterior space, and the slot if it has a finite thickness, and (ii) the evaluation of its matrix involves highly singular integrals and very slowly converging series. In this paper, we address all these problems. To be more specific, we first formulate the integral equations for the problem and apply the MoM with global basis functions and Galerkin's testing procedure. We then describe in detail the evaluation of the MoM matrix involving various dyadic Green's functions. The slow convergence of the series associated with the summation of waveguide modes is accelerated using the Kummer transformation and the slow convergence of the series associated with the summation of the exterior modes is avoided by using the asymptotic solutions developed by Boersma and Lee [24] and Bird [25]. The evaluation of the excitation vector and scattered field is also accelerated using Watson's transformation and asymptotic solutions. Finally, we present some numerical results to illustrate the scattering characteristics of the cylindrically conformal slotted waveguide arrays, such as the effects of curvature, slot thickness, waveguide termination, and frequency on the RCS of the arrays.

II. THEORY

In this section, we describe in detail the formulation of the problem and its solution by the MoM. Particular attention is given to the computation of the elements of the generalized admittance matrices.

A. Integral Equations and MoM Solution

Consider the problem of electromagnetic wave scattering by a waveguide-fed slot array on a cylindrical surface whose radius is ρ_3 , as depicted in Fig. 1. The cross section of each waveguide is an annular sector with inner radius ρ_1 , outer radius ρ_2 , and subtended angle $\Delta\phi$, and the thickness of the curved walls of the waveguides is $t = \rho_3 - \rho_2$. Each waveguide is terminated at $z = z_1$ and z_2 with an arbitrary load. All radiating slots are longitudinal slots cut in the outer wall of the waveguides, having the same width $2w$ and different length and offset with respect to the center-line of the waveguides.

For the i th slot, its inner and outer apertures, S_i^I and S_i^H , divide the space into three regions: the waveguide region (region a), the region outside the cylinder (region b), and the slot region (region c), as illustrated in Fig. 2. In accordance with the equivalence principle, the fields in the three regions can be decoupled by covering the apertures S_i^I and S_i^H with a perfectly conducting surface and introducing equivalent magnetic currents above and below the perfectly conducting surface. Denoting the equivalent magnetic current below S_i^I as M_i^I and that below S_i^H as M_i^H ,

because of the continuity of the tangential electric fields across the apertures, the equivalent magnetic current above S_i^I is $-\mathbf{M}_i^I$ and that above S_i^H is $-\mathbf{M}_i^H$. Therefore, the field in region a is due to \mathbf{M}_i^I , the field in region b is due to $-\mathbf{M}_i^H$ and the incident field, and the field in region c is due to $-\mathbf{M}_i^I$ and \mathbf{M}_i^H .

By enforcing the continuity of the tangential magnetic fields across S_i^I and S_i^H , we obtain the integral equations satisfied by the equivalent magnetic currents, \mathbf{M}_i^I and \mathbf{M}_i^H , as

$$\sum_j \mathbf{H}_{\tau i}^a(\mathbf{M}_j^I) + \mathbf{H}_{\tau i}^c(\mathbf{M}_i^I) - \mathbf{H}_{\tau i}^c(\mathbf{M}_i^H) = 0 \quad \mathbf{r} \in S_i^I \quad (1)$$

$$\sum_j \mathbf{H}_{\tau i}^b(\mathbf{M}_j^H) + \mathbf{H}_{\tau i}^c(\mathbf{M}_i^H) - \mathbf{H}_{\tau i}^c(\mathbf{M}_i^I) = \mathbf{H}_{\tau i}^{pri} \quad \mathbf{r} \in S_i^H \quad (2)$$

where the subscript τ denotes the tangential component, the summation in (1) is carried out for all inner apertures in the same waveguide, and the summation in (2) is carried out for all outer apertures. The magnetic field is related to the surface magnetic current by

$$\mathbf{H}^\alpha(\mathbf{r}) = \iint_S \bar{\bar{G}}^\alpha(\mathbf{r}, \mathbf{r}') \cdot \mathbf{M}(\mathbf{r}') dS' \quad (3)$$

where $\alpha = a$ for region a , b for region b , and c for region c , respectively, and $\bar{\bar{G}}^\alpha(\mathbf{r}, \mathbf{r}')$ denotes the magnetic-source magnetic-field dyadic Green's function in the corresponding region. Finally, \mathbf{H}^{pri} is the field due to the incident field in the presence of the conducting cylinder without slots.

To seek a numerical solution of (1) and (2), we first expand each equivalent magnetic current using the global sinusoidal basis functions

$$\mathbf{M}_j^{I,H} = \hat{z} M_j^{I,H} = \hat{z} \sum_{q=1}^{N_j^{I,H}} V_{qj}^{I,H} \sin \alpha_{qj} \xi \quad \mathbf{r} \in S_j^{I,H} \quad (4)$$

where $\alpha_{qj} = q\pi/L_j$ with L_j being the length of the j th slot. Applying Galerkin's procedure, the integral equations can be converted into the matrix equation given by

$$\begin{bmatrix} [Y_{pq}^{ij}(a) + Y_{pq}^{ij}(c, S_i^I; S_j^I)] & [-Y_{pq}^{ij}(c, S_i^I; S_j^H)] \\ [-Y_{pq}^{ij}(c, S_i^H; S_j^I)] & [Y_{pq}^{ij}(b) + Y_{pq}^{ij}(c, S_i^H; S_j^H)] \end{bmatrix} \begin{Bmatrix} [V_{qj}^I] \\ [V_{qj}^H] \end{Bmatrix} = \begin{Bmatrix} [0] \\ [I_{pi}] \end{Bmatrix} \quad (5)$$

where $[Y_{pq}^{ij}(a)]$ and $[Y_{pq}^{ij}(b)]$ are the generalized admittance matrix for regions a and b , respectively. $[Y_{pq}^{ij}(c, S_i^f; S_j^s)]$ is the generalized admittance matrix for region c , in which S_i^f is the aperture on which the field point is located and S_j^s is the aperture on which the source point is located. Finally, $[I_{pi}]$ is the generalized excitation vector.

In the remainder of this section, we describe the evaluation of the elements of each generalized admittance matrix and excitation vector, necessary for a numerical solution of (5).

B. Generalized Admittance Matrix Elements for Region a

The admittance matrix elements due to the internal coupling in the sectoral waveguide (region a) are given by

$$Y_{pq}^{ij}(a) = \iint_{S_i^i} \iint_{S_j^j} G_{zz}^a(\mathbf{r}, \mathbf{r}') \sin \alpha_{pi} \xi \sin \alpha_{qj} \xi' dS dS' \quad (6)$$

where G_{zz}^a is the $\hat{z}\hat{z}$ -component of the magnetic-source magnetic-field dyadic Green's function for the sectoral waveguide, which is derived in [26] and given by

$$G_{zz}^a = j\omega\epsilon \sum_{m=0}^{\infty} \sum_{n=0}^{\infty} B(m, n) C_{\varphi} C_{\varphi'} \left\{ \delta(z - z') - \frac{\lambda_{mn}^2}{2jh_{mn}\Delta_{mn}} \left[e^{-jh_{mn}|z-z'|} - R_{mn}^< e^{j2h_{mn}z_1} e^{-jh_{mn}(z+z')} - R_{mn}^> e^{-j2h_{mn}z_2} e^{jh_{mn}(z+z')} + R_{mn}^< R_{mn}^> e^{-jh_{mn}(z_2-z_1)} e^{jh_{mn}|z-z'|} \right] \right\} \quad (7)$$

where

$$B(m, n) = \frac{2}{1 + \delta_{0m}} \frac{B_{\nu}(\lambda_{mn}\rho) B_{\nu}(\lambda_{mn}\rho')}{k^2 N_{\lambda_{mn}} \Delta\phi} \Big|_{\rho=\rho'=\rho_2} \quad (8)$$

in which

$$B_{\nu}(\lambda_{mn}\rho) = J'_{\nu}(\lambda_{mn}\rho_1) Y_{\nu}(\lambda_{mn}\rho) - Y'_{\nu}(\lambda_{mn}\rho_1) J_{\nu}(\lambda_{mn}\rho), \quad (9)$$

$$N_{\lambda_{mn}} = \frac{1}{2\lambda_{mn}^2} \left\{ (\lambda_{mn}^2 \rho^2 - \nu^2) [B_{\nu}(\lambda_{mn}\rho)]^2 \right\}_{\rho_1}^{\rho_2}. \quad (10)$$

Also, in the above, $\nu = m\pi/\Delta\phi$, $C_{\varphi} = \cos \nu\varphi$, $C_{\varphi'} = \cos \nu\varphi'$, $h_{mn} = \sqrt{k^2 - \lambda_{mn}^2}$, λ_{mn} are the roots of $B'_{\nu}(\lambda_{mn}\rho_2) = 0$, $\Delta_{mn} = 1 - R_{mn}^< R_{mn}^> e^{-jh_{mn}(z_2-z_1)}$, and $R_{mn}^<$ and $R_{mn}^>$ are the reflection coefficients for mode (m, n) at $z = z_1$ and $z = z_2$, respectively. For shorted terminals $R_{mn} = -1$, and for matched terminals $R_{mn} = 0$.

The integrals in (6) can be evaluated analytically through the transformation of variables, resulting in

$$Y_{pq}^{ij}(a) = -j\omega\epsilon \sum_{m=0}^{\infty} \sum_{n=0}^{\infty} B(m, n) I_{\varphi}^{ij}(m) \left[I_{z0}^{ij}(m, n) + I_{zim}^{ij}(m, n) \right] \quad (11)$$

where $I_{\varphi}^{ij}(m) = I_{\varphi}^i(m) I_{\varphi}^j(m)$ with $I_{\varphi}^i(0) = 2w$ and

$$I_{\varphi}^i(m) = \frac{\rho_2}{\nu} \sum_{U=\pm\nu} \text{sgn}(U) \sin \left[\frac{\nu}{\rho_2} \left(\frac{\rho_2 \Delta\phi}{2} + \delta_i + U \right) \right] \quad m \neq 0$$

and δ_i denotes the offset of the i th slot from the center of the waveguide. Also,

$$I_{z0}^{ii}(m, n) = C(m, n) [1 + (-1)^{p+q}] [1 - (-1)^p e^{-jh_{mn}L_i}] + \delta_{pq} \frac{(k^2 - \alpha_{pi}^2) L_i}{\alpha_{pi}^2 - h_{mn}^2} \quad (12)$$

$$I_{z0}^{ij}(m, n) = C(m, n) e^{\mp jh_{mn}[(z_{0i}-z_{0j})-(L_i-L_j)/2]} \cdot [1 - (-1)^p e^{\mp jh_{mn}L_i}] [1 - (-1)^q e^{\pm jh_{mn}L_j}] \quad z_{0i} \gtrless z_{0j} \quad (13)$$

with

$$C(m, n) = \frac{\lambda_{mn}^2}{2jh_{mn}\Delta_{mn}} \frac{\alpha_{pi}}{\alpha_{pi}^2 - h_{mn}^2} \frac{\alpha_{qj}}{\alpha_{qj}^2 - h_{mn}^2} \quad (14)$$

and z_{0i} and z_{0j} denote the center of the i th and j th slots, respectively. Finally, $I_{zim}^{ij}(m, n)$ can be written in three parts as

$$I_{zim}^{ij}(m, n) = I_{z1}^{ij}(m, n) + I_{z2}^{ij}(m, n) + I_{z3}^{ij}(m, n) \quad (15)$$

with

$$I_{z1}^{ij}(m, n) = -C(m, n)R_{mn}^< e^{-jh_{mn}[(z_{0i}+z_{0j})-(L_i+L_j)/2-2z_1]} \cdot [1 - (-1)^p e^{-jh_{mn}L_i}] [1 - (-1)^q e^{-jh_{mn}L_j}] \quad (16)$$

$$I_{z2}^{ij}(m, n) = -C(m, n)R_{mn}^> e^{-jh_{mn}[2z_2-(z_{0i}+z_{0j})+(L_i+L_j)/2]} \cdot [1 - (-1)^p e^{jh_{mn}L_i}] [1 - (-1)^q e^{jh_{mn}L_j}] \quad (17)$$

$$I_{z3}^{ii}(m, n) = C(m, n)R_{mn}^< R_{mn}^> e^{-2jh_{mn}(z_2-z_1)} \cdot [1 + (-1)^{p+q}] [1 - (-1)^p e^{jh_{mn}L_i}] \quad (18)$$

$$I_{z3}^{ij}(m, n) = C(m, n)R_{mn}^< R_{mn}^> e^{-2jh_{mn}(z_2-z_1)} e^{jh_{mn}[(z_{0i}-z_{0j})-(L_i-L_j)/2]} \cdot [1 - (-1)^p e^{\mp jh_{mn}L_i}] [1 - (-1)^q e^{\pm jh_{mn}L_j}] \quad z_{0i} \gtrless z_{0j}. \quad (19)$$

While the summation in (11) can be evaluated without any difficulty when $i \neq j$, its evaluation when $i = j$ involves a slowly converging series given by

$$S(m) = \sum_{n=0}^{\infty} B(m, n)I_{z0}^{ii} = S_1(m) + S_2(m) \quad (20)$$

where

$$S_1(m) = \sum_{n=0}^{\infty} B(m, n)C(m, n) [1 + (-1)^{p+q}] [1 - (-1)^p e^{-jh_{mn}L_i}] \quad (21)$$

$$S_2(m) = \sum_{n=0}^{\infty} B(m, n)\delta_{pq} \frac{(k^2 - \alpha_{pi}^2)L_i}{\alpha_{pi}^2 - h_{mn}^2}. \quad (22)$$

To show this, let us examine the asymptotic behavior of the series when $n \rightarrow \infty$. Using the asymptotic expression of the Bessel functions for large arguments, we obtain the approximate solution to the eigenvalue equation $B'_\nu(\lambda_{mn}\rho_2) = 0$ as

$$\lambda_{mn} \sim \frac{n\pi}{\rho_2 - \rho_1} \quad (23)$$

and hence

$$jh_{mn} \sim \frac{n\pi}{\rho_2 - \rho_1}, \quad B(m, \infty) \sim \frac{1}{1 + \delta_{0m}} \frac{2}{k^2(\rho_2 - \rho_1)\rho_2\phi_0}. \quad (24)$$

Clearly, the asymptotic form of the terms in $S_1(m)$ is proportional to n^{-3} and that in $S_2(m)$ is proportional to n^{-2} . To accelerate the convergence of $S_2(m)$, we apply the Kummer transform [27] to (22), resulting in

$$S_2(m) = \delta_{pq}(k^2 - \alpha_{pi}^2)L_i \left\{ \sum_{m=0}^{\infty} \left[\frac{B(m, n)}{\alpha_{pi}^2 - h_{mn}^2} - \left(\frac{\rho_2 - \rho_1}{\pi} \right)^2 \frac{B(m, \infty)}{n^2 + x^2} \right] + \left(\frac{\rho_2 - \rho_1}{\pi} \right)^2 B(m, \infty) \sum_{m=0}^{\infty} \frac{1}{n^2 + x^2} \right\} \quad (25)$$

where

$$x^2 = \left(\frac{\rho_2 - \rho_1}{\pi} \right)^2 \left\{ \alpha_{pi}^2 - k^2 - \left[\frac{2m\pi}{(\rho_2 - \rho_1)\phi_0} \right]^2 \right\}. \quad (26)$$

The first summation in (25) converges rapidly and the second summation can be written in a closed form as

$$\sum_{n=0}^{\infty} \frac{1}{n^2 + x^2} = \begin{cases} \frac{1}{2x} \left[\frac{1}{x} + \pi \coth \pi x \right] & x^2 > 0 \\ \frac{-1}{2|x|} \left[\frac{1}{|x|} + \pi \cot \pi |x| \right] & x^2 < 0. \end{cases} \quad (27)$$

In passing, we note that when ρ_1 and $\rho_2 \rightarrow \infty$, the expressions for sectoral waveguides reduce to those for the corresponding rectangular waveguides [26].

C. Generalized Admittance Matrix Elements for Region b

The admittance matrix elements due to the external coupling in region b are given by

$$Y_{pq}^{ij}(b) = \iint_{S_i^H} \iint_{S_j^H} G_{zz}^b(\mathbf{r}, \mathbf{r}') \sin \alpha_{pi} \xi \sin \alpha_{qj} \xi' dS dS' \quad (28)$$

where G_{zz}^b is the $\hat{z}\hat{z}$ -component of the magnetic-source magnetic-field dyadic Green's function for the conducting cylinder. The rigorous expressions of the dyadic Green's function involve infinite series and infinite integrations of Hankel's functions [28], [29]. Although these expressions can be converted into the forms suitable to numerical calculation [29], it is still very time consuming to compute the matrix elements, especially when the cylinder is large. Therefore, it is necessary to seek the fast converging asymptotic solutions. Several different approximate asymptotic solutions have been developed in the past [24], [25], [30]–[32], and each has its accuracy and range of validity. A comparative study [29] shows that the B-L [24] and TSB [25] solutions offer the best overall accuracy, and these two solutions are complementary to each other. More specifically, the B-L solution is more accurate when the field point is near the source or in the paraxial region while the TSB solution is better when the field point is far from the source and off axis. In this work, the TSB solution is used for two distant slots whose centers have the same z -coordinate, whereas the B-L solution is employed for all other cases.

When $i \neq j$, the integrals in (28) can be evaluated numerically without any difficulty [26]. However, when $i = j$, G_{zz}^b has a t^{-3} singularity as $t \rightarrow 0$, and hence, a regularization is needed to for the evaluation. To do this, we first write G_{zz}^b as

$$G_{zz}^b = G_{zz}^0 + \tilde{G}_{zz} \quad (29)$$

where G_{zz}^0 is the $\hat{z}\hat{z}$ -component of the dyadic Green's function for an infinite conducting ground plane, given by

$$G_{zz}^0 = \frac{k^2}{j\omega\mu} \left(1 + \frac{1}{k^2} \frac{\partial^2}{\partial z^2} \right) \frac{e^{-jkt}}{2\pi t} \quad (30)$$

and \tilde{G}_{zz} can be considered as the perturbation due to the curvature of the cylinder [31], given by

$$\begin{aligned} \tilde{G}_{zz} = G_0(t) \left\{ [v(\tilde{\beta}) - 1] [\cos^2 \tilde{\theta} + \tilde{q}(1 - \tilde{q})(2 - 3\cos^2 \tilde{\theta})] \right. \\ \left. - \tilde{q}\tilde{\beta}v'(\tilde{\beta}) \left[\frac{11}{12} \cos^2 \tilde{\theta} + \tilde{q} \left(\frac{11}{6} + \frac{2}{3} \tan^2 \tilde{\theta} - \frac{187}{64} \cos^2 \tilde{\theta} \right) \right] \right\} \end{aligned} \quad (31)$$

where $G_0(t) = \exp(-jkt)/(4\pi t)$, $t = \sqrt{(z - z')^2 - (\varphi - \varphi')^2}$, $\tilde{\theta} = \arctan[(z - z')/(\varphi - \varphi')]$, $\tilde{q} = j/kt$, $\tilde{\beta} = (k \cos^4 \tilde{\theta}/2R^2)^{1/3}t$, and v is the surface Fock function defined in [24]–[26]. As a result, the self-admittance matrix element can be written as

$$Y_{pq}^{ii}(b) = Y_{pq}^{0ii}(b) + \tilde{Y}_{pq}^{ii}(b). \quad (32)$$

Using integration of part and transformation of variables, $Y_{pq}^{0ii}(b)$ can be written as [8]

$$Y_{pq}^{0ii}(b) = \frac{k^2}{j\omega\mu} \frac{1 + (-1)^{p+q}}{2\pi k^2} \int_0^{L_i} \int_0^{2w} \frac{e^{-jkt}}{t} F(u, v) dv du \quad (33)$$

where $t = \sqrt{u^2 + v^2}$ and

$$F(u, v) = \begin{cases} \frac{2(2w-v)}{\alpha_{pi}^2 - \alpha_{qi}^2} [\alpha_{pi}(k^2 - \alpha_{qi}^2) \sin \alpha_{qi}u - \alpha_{qi}(k^2 - \alpha_{pi}^2) \sin \alpha_{pi}u] & p \neq q \\ (2w - v) [(L_i - u)(k^2 - \alpha_{pi}^2) \cos \alpha_{pi}u + \frac{1}{\alpha_{pi}}(k^2 + \alpha_{pi}^2) \sin \alpha_{pi}u] & p = q. \end{cases} \quad (34)$$

The integral in (33) becomes regular when evaluated in the polar coordinates.

To evaluate the perturbation term in (32), we first let $\eta = \rho_3\varphi$, $\eta' = \rho_3\varphi'$, and write it as

$$\tilde{Y}_{pq}^{ii}(b) = \int_0^{L_i} \int_{-w}^w \int_{-w}^{L_i} \int_{-w}^w \tilde{G}_{zz}(\xi - \xi', \eta - \eta') \sin \alpha_{pi}\xi \sin \alpha_{qi}\xi' d\eta' d\xi' d\eta d\xi. \quad (35)$$

Introducing the transformations $u = \xi - \xi'$, $v = \eta - \eta'$, $u' = \xi + \xi' - L_i$, and $v' = \eta + \eta'$, and observing that $\tilde{G}_{zz}(u, v)$ is an even function of u and v , we obtain

$$\tilde{Y}_{pq}^{ii}(b) = [1 + (-1)^{p+q}] \int_0^{L_i} \int_0^w (2w - v) \tilde{G}_{zz}(u, v) \tilde{F}(u) dv du \quad (36)$$

where

$$\tilde{F}(u) = \begin{cases} \frac{2}{\alpha_{pi}^2 - \alpha_{qi}^2} [(-1)^{p+q} \alpha_{pi} \sin \alpha_{qi} u - \alpha_{qi} \sin \alpha_{pi} u] & p \neq q \\ (L_i - u) \cos \alpha_{pi} u + \frac{1}{\alpha_{pi}} \sin \alpha_{pi} u & p = q. \end{cases} \quad (37)$$

With another transformation $u = t \cos \theta$, and $v = t \sin \theta$, (36) becomes

$$\tilde{Y}_{pq}^{ii}(b) = [1 + (-1)^{p+q}] \left\{ \int_0^{\theta_0} \int_0^{L_i/\cos \theta} + \int_{\theta_0}^{\pi/2} \int_0^{2w/\sin \theta} \right\} \cdot (2w - t \sin \theta) \tilde{G}_{zz}(t, \theta) \tilde{F}(t, \theta) t d\theta dt \quad (38)$$

where $\theta_0 = \tan^{-1}(2w/L_i)$ and $\tilde{G}_{zz}(t, \theta)$ has the same form as (31). The integrals in (38) become regular by letting $t = r^2$, which can be evaluated by expanding the integrand in terms of the power of r and using a Gaussian quadrature. The Fock function can be evaluated using its small-argument expansions.

D. Generalized Admittance Matrix Elements for Region c

It can be shown [26] that the magnetic field in the cavity (region c with a sectoral cross-section), formed by the slot with its two apertures covered by a perfectly conducting surface, due to the surface magnetic current $\hat{z}\delta(\rho - \rho') \sin \alpha_{pi}\xi$ is given by

$$H_z(\rho, \rho') = \frac{\beta C}{j\omega\mu} \sin \alpha_{pi}\xi \begin{cases} B(\rho_2, \rho) B(\rho_3, \rho') & \rho < \rho' \\ B(\rho_3, \rho) B(\rho_3, \rho') & \rho > \rho' \end{cases} \quad (39)$$

where $\beta^2 = |k^2 - \alpha_{pi}^2|$ and

$$C = [B(\rho_2, \rho') B'(\rho_3, \rho') - B(\rho_3, \rho') B'(\rho_2, \rho')]^{-1} \quad (40)$$

$$B(\rho', \rho) = \begin{cases} J'_0(\beta\rho') Y_0(\beta\rho) - Y'_0(\beta\rho') J_0(\beta\rho) & k > \alpha_{pi} \\ I'_0(\beta\rho') K_0(\beta\rho) - K'_0(\beta\rho') I_0(\beta\rho) & k < \alpha_{pi}. \end{cases} \quad (41)$$

Using (39), we obtain the expressions for the generalized admittance matrix elements for region c as

$$Y_{pq}^{ij}(c, S_i^I; S_j^I) = \frac{L_i w \beta}{j\omega\mu} \frac{B(\rho_3, \rho_2)}{B'(\rho_3, \rho_2)} \delta_{ij} \delta_{pq} \quad (42)$$

$$Y_{pq}^{ij}(c, S_i^I; S_j^II) = \frac{L_i w \beta}{j\omega\mu} \frac{-1}{\beta \rho_2 B'(\rho_2, \rho_3)} \delta_{ij} \delta_{pq} \quad (43)$$

$$Y_{pq}^{ij}(c, S_i^II; S_j^I) = \frac{L_i w \beta}{j\omega\mu} \frac{1}{\beta \rho_3 B'(\rho_3, \rho_2)} \delta_{ij} \delta_{pq} \quad (44)$$

$$Y_{pq}^{ij}(c, S_i^II; S_j^II) = \frac{L_i w \beta}{j\omega\mu} \frac{-B(\rho_2, \rho_3)}{B'(\rho_2, \rho_3)} \delta_{ij} \delta_{pq}. \quad (45)$$

Note that when ρ_2 and $\rho_3 \rightarrow \infty$, the expressions above reduce to those for a rectangular cavity [26].

E. Excitation Vector and Scattered Field

Consider an incident plane wave of arbitrary polarization and incidence angle, whose electric field is given by

$$\mathbf{E}^{inc} = (\hat{\theta}^{inc} \cos \psi + \hat{\varphi}^{inc} \sin \psi) e^{-jk \hat{\mathbf{r}}^{inc} \cdot \mathbf{r}} \quad (46)$$

where ψ is the polarization angle, $(\theta^{inc}, \varphi^{inc})$ denote the incidence angles, and $(\hat{\mathbf{r}}^{inc}, \hat{\theta}^{inc}, \hat{\varphi}^{inc})$ are the unit vectors. The primary field, \mathbf{H}^{pri} in (2), is given by

$$H_z^{pri} \Big|_{\rho=\rho_3} = -Y_0 \sin \psi \sin \theta^{inc} e^{jkz \cos \theta^{inc}} M(k\rho_3 \sin \theta^{inc}, \varphi - \varphi^{inc}) \quad (47)$$

where

$$M(x, \varphi) = \frac{2}{j\pi x} \sum_{n=0}^{\infty} \frac{2}{1 + \delta_{0n}} \frac{j^n \cos n\varphi}{H_n^{(2)}(x)} \quad (48)$$

from which we obtain the elements of the excitation vector as

$$\begin{aligned} I_{pi} &= \iint_{S_i^+} H_z^{pri} \Big|_{\rho=\rho_3} \sin \alpha_{pi} \xi \, dS \\ &= 4Y_0 \frac{\Delta\varphi L_i}{p\pi} \sin \psi \sin \theta^{inc} e^{jkz_{0i} \cos \theta^{inc}} f_p(\theta^{inc}) \widetilde{M}(k\rho_3 \sin \theta^{inc}, \varphi_{0i} - \varphi^{inc}, \Delta\varphi) \end{aligned} \quad (49)$$

where

$$f_p(\theta) = \left[1 - \left(\frac{kL_i}{p\pi} \cos \theta \right)^2 \right]^{-1} \begin{cases} -\cos \left(\frac{kL_i}{2} \cos \theta \right) & p = \text{odd} \\ j \sin \left(\frac{kL_i}{2} \cos \theta \right) & p = \text{even} \end{cases} \quad (50)$$

$$\widetilde{M}(x, \varphi, \Delta\varphi) = \frac{2}{j\pi x} \sum_{n=0}^{\infty} \frac{2}{1 + \delta_{0n}} \frac{j^n \cos n\varphi}{H_n^{(2)}(x)} \text{sinc}(n \Delta\varphi) \quad (51)$$

in which $\Delta\varphi = w/\rho_3$. For narrow slots, we can use the midpoint integration to find

$$I_{pi} = 4Y_0 \frac{\Delta\varphi L_i}{p\pi} \sin \psi \sin \theta^{inc} e^{jkz_{0i} \cos \theta^{inc}} f_p(\theta^{inc}) M(k\rho_3 \sin \theta^{inc}, \varphi_{0i} - \varphi^{inc}). \quad (52)$$

When x becomes large, $M(x, \varphi)$ for the lit region can be evaluated more efficiently using the expression [28]

$$M(x, \varphi) \cong 2e^{jx \cos \varphi} \quad (53)$$

which can be considered as the geometrical optics approximation and it has the same accuracy as Gorianov's more complicated expression [33]. For the neighborhood of the shadow boundary and the shadow region, $M(x, \varphi)$ can be evaluated using the expression obtained using the Watson transformation and Fock theory [28],

$$M(x, \varphi) \sim e^{-jx(\varphi - \frac{\pi}{2})} g \left[\left(\varphi - \frac{\pi}{2} \right) \left(\frac{x}{2} \right)^{1/3} \right] + e^{-jx(\frac{3\pi}{2} - \varphi)} g \left[\left(\frac{3\pi}{2} - \varphi \right) \left(\frac{x}{2} \right)^{1/3} \right] \quad (54)$$

where $g(x)$ is the far-zone Fock function, whose definition and evaluation are discussed in [26], [28], [34], and [35].

Once the equivalent magnetic currents on the slot apertures are found, we can compute the scattered field using the reciprocity theorem.

III. NUMERICAL RESULTS

The formulation described above has been implemented in a computer program and a variety of numerical results have been obtained to study the effects of various factors on RCS. Because of limited space, we present only some typical results; more results can be found in [26].

For all the examples considered, the cross-section of sectoral waveguides is given by $\frac{1}{2}(\rho_1 + \rho_2)\Delta\phi = 21$ mm and $\rho_2 - \rho_1 = 10.16$ mm. The distance between the center-lines of the adjacent waveguides is 22 mm, measured on the surface of the cylinder. The adjacent slots on the same waveguide are spaced $\lambda_{g0}/2$ apart in the z direction, where λ_{g0} is the waveguide wavelength at the working frequency (the center frequency of design). The shorted planes are placed $\lambda_{g0}/4$ away from the first and last slots, respectively. In order to avoid the numerical overflow in the computation of the generalized admittance elements for the shorted waveguides at the working frequency, the position of the shorted planes is displaced by Δz , which can be considered as an acceptable manufacturing tolerance. All other parameters, unless otherwise specified, are given by: $2w = 1.6$ mm, $L_i = 16$ mm, $\delta_i = 1.5$ mm, $\Delta t = 0.8$ mm, $\Delta z = 0.01$ mm, $\psi = 90^\circ$, and the working frequency $f_0 = 9.1$ GHz. The normal at the center of the array is $\theta = 90^\circ$ and $\phi = 0^\circ$ in the spherical coordinate system.

The computer program was first validated by comparing its solution to those obtained by MoM and FEM [23] for a single slot and for four slots on a planar surface. Good agreement was observed between the three solutions.

To demonstrate the effect of the curvature of the host cylinder on the RCS of a conformal slot array, Figs. 3 and 4 show the RCS for $\rho_1 = \infty$, $\rho_1 = 500$ cm, $\rho_1 = 200$ cm, $\rho_1 = 100$ cm, and $\rho_1 = 50$ cm in both E- and H-planes. As can be seen, the cylinder's curvature has a significant effect on the patterns and values of the RCS in the E-plane. When ρ_1 becomes large, the RCS approaches that for a planar array. When ρ_1 decreases, the grating lobes begin to disappear and the maximum RCS decreases. In contrast, the pattern of the RCS in the H-plane remains the same and only the value of the RCS is decreased as ρ_1 decreases.

To further demonstrate the effect of the cylinder's curvature on the RCS, Fig. 5 presents the space distribution of the RCS for $\rho_1 = \infty$, $\rho_1 = 200$ cm, $\rho_1 = 100$ cm, and $\rho_1 = 30$ cm. As can be seen clearly, as ρ_1 decreases the grating lobes in the E-plane is dilated where the pattern

in the H-plane remains the same.

To show the effect of the waveguide terminals on the RCS, Fig. 6 gives the RCS of a 8×8 conformal slot array ($\rho_1 = 100$ cm) when the waveguide terminals are matched and shorted. It can be seen that when the plane wave is incident normally on the cylinder ($\theta = 90^\circ$), the RCS is very small for the array with shorted terminals. This is because at the working frequency, the wave entered the waveguide is reflected by the shorted terminals and the reflected wave cancels the incident wave at the slot. Thus, the total electric field or the total equivalent magnetic current is zero at the aperture of the slot. An alternative explanation is that with the shorted terminals, the equivalent impedance looking at the aperture of the slots is zero. Therefore, when the shorted planes are displaced, the equivalent impedance will be changed and so is the RCS. This is clearly demonstrated in [26].

The effect of the slot thickness on the RCS is also investigated in [26]. It is observed that, at the working frequency, the slot thickness has no effect on the RCS when the waveguides are matched and when the waveguides are shorted, it has a significant effect. This effect can also be explained using the concept of the equivalent impedance.

Finally, Fig. 7 shows the frequency responses of a 8×8 array ($\rho_1 = 100$ cm) with matched and shorted terminals, respectively. It is very interesting to note that the RCS of the slot array is almost identical no matter the waveguides are matched or shorted when the frequency is not close to the working frequency. At the working frequency, the RCS is substantially different. This implies that when the frequency of the incident wave is not close to the working frequency of the slot array, the energy entering the waveguides is very trivial and the main contribution to the RCS is the wave scattered by the slots directly. Therefore, in this case the dominant factor is the geometry of the slots, instead of the structures behind the slots. Figure 8 shows the space distribution of the RCS of a 16×16 array ($\rho_1 = 100$ cm) at three different frequencies.

IV. CONCLUSION

In this paper, a method of moments (MoM) solution was developed for electromagnetic scattering by a cylindrically conformal waveguide-fed slot array. Numerical results were presented to illustrate the scattering characteristics of the cylindrically conformal waveguide-fed slot arrays, such as the effects of curvature, slot thickness, and waveguide termination on the radar cross section of the arrays. It was observed that (i) as the curvature of the host cylinder increases, the grating lobes in the E-plane dilate and eventually disappear and the maximum RCS is reduced; (ii) the internal structure of the waveguides such as the waveguide terminals has negligible effect on the RCS when the frequency of the incident wave is not close to the

working frequency of the slot array; (iii) at the working frequency the RCS of the slot array with a shorted terminals at normal incidence changes significantly with the position of the shorted terminals; and (iv) at the working frequency the slot thickness has no effect on the RCS of the array with matched terminals whereas for the array with shorted terminals its effect is noticeable.

References

- [1] A. F. Stevenson, "The theory of slots in rectangular waveguides," *J. Appl. Phys.*, vol. 19, pp. 24-38, Jan. 1948.
- [2] A. A. Oliner, "The impedance properties of narrow radiating slots in the broad face of rectangular waveguide," *IRE Trans. Antennas Propagat.*, vol. 5, pp. 4-20, Jan. 1957.
- [3] T. Vu Khac and C. T. Carson, "Impedance properties of a longitudinal slot antenna in the broad face of rectangular waveguide," *IEEE Trans. Antennas Propagat.*, vol. 21, pp. 708-710, Sept. 1973.
- [4] H. Y. Yee, "Impedance of a narrow longitudinal shunt slot in a slotted waveguide array," *IEEE Trans. Antennas Propagat.*, vol. 22, pp. 589-592, July 1974.
- [5] R. W. Lyon and A. J. Sangster, "Efficient moment method analysis of radiating slots in thick-walled rectangular waveguide," *IEE Proc., Pt. H*, vol. 128, pp. 197-205, Aug. 1981.
- [6] G. J. Stern and R. S. Elliott, "Resonant length of longitudinal slots and validity of circuit representation: Theory and experiment," *IEEE Trans. Antennas Propagat.*, vol. 33, pp. 1264-1271, Nov. 1985.
- [7] L. G. Josefsson, "Analysis of a longitudinal slot in rectangular waveguide," *IEEE Trans. Antennas Propagat.*, vol. 35, pp. 1351-1357, Dec. 1987.
- [8] K. Xia and Q.-J. Yang, "Study on characteristics of dielectric-covered waveguide slots," *Chinese J. Appl. Sci.*, vol. 7, no. 2, pp. 115-123, 1989.
- [9] S. R. Rengarajan, "Compound radiating slots in a broad wall of a rectangular waveguide," *IEEE Trans. Antennas Propagat.*, vol. 37, pp. 1116-1123, Sept. 1989.
- [10] P. B. Katehi, "Dielectric-covered waveguide longitudinal slots with finite wall thickness," *IEEE Trans. Antennas Propagat.*, vol. 38, pp. 1039-1045, July 1990.

- [11] R. S. Elliott, "An improved design procedure for small array of shunt slots," *IEEE Trans. Antennas Propagat.*, vol. 31, pp. 48-53, Jan. 1983.
- [12] A. J. Sangster and A. H. I. McCormick, "Theoretical design/synthesis of slotted waveguide arrays," *IEE Proc., Pt. H*, vol. 136, pp. 39-46, Feb. 1989.
- [13] J. Zheng and Q.-J. Yang, "Dielectric-covered conformal slot array antenna on a large conducting cylinder," *Acta Electronica Sinica*, vol. 18, no. 1, pp. 57-63, 1990.
- [14] J. J. Gulick and R. S. Elliott, "The design of linear and planar array of waveguide-fed longitudinal slots," *Electromagnetics*, vol. 10, pp. 327-347, Oct.-Dec. 1990.
- [15] H. Y. Yee, "The design of large waveguide arrays of shunt slots," *IEEE Trans. Antennas Propagat.*, vol. 40, pp. 775-781, July 1992.
- [16] S. R. Rengarajan and A. G. Derneryd, "Application of compound coupling slots in the design of shaped beam antenna patterns for array application," *IEEE Trans. Antennas Propagat.*, vol. 41, pp. 59-65, Jan. 1993.
- [17] Q.-J. Yang and X. Tian, "Computer-aided-design of planar slot antennas," *Chinese J. Radio Sci.*, vol. 9, no. 1, pp. 1-11, 1994.
- [18] K. Xia and Q.-J. Yang, "Study on the inclined slots in the narrow wall of a rectangular waveguide," *Acta Electronica Sinica*, vol. 20, no. 2, pp. 45-52, 1992.
- [19] S. -W. Lue, Y. Zhang and S. -M. Cao, "The equivalent parameters for the radiating slot on a sectoral waveguide," *IEEE Trans. Antennas Propagat.*, vol. 42, pp. 1577-1581, Nov. 1994.
- [20] G.-X. Fan, "Cylindrically conformal slotted-waveguide array antenna," Ph.D. dissertation, Tsinghua University, Beijing, China, Apr. 1995.
- [21] L. G. Josefsson, "Slot coupling and scattering," *1990 IEEE Antennas Propagat. Int. Symp.*, pp. 942-945, Dallas, TX, June 1990.
- [22] L. C. Trintinalia and H. Ling, "Electromagnetic scattering from 3-D arbitrary coated cavities via a connection scheme using triangular patches," *J. Electromag. Waves Appl.*, vol. 8, pp. 1411-1423, Nov. 1994.
- [23] J. Chen and J.-M. Jin, "Electromagnetic scattering from slot antennas on waveguides with arbitrary terminations," *Microwave Opt. Tech. Lett.*, vol. 10, no. 5, pp. 286-291, Dec. 1995.

- [24] J. Boersma and S. W. Lee, "Surface field due to a magnetic dipole on a cylinder: Asymptotic expansions of exact solution," Univ. of Illinois at Urbana-Champaign, Electromagnetics Lab. Rep. 78-17, 1978.
- [25] T. S. Bird, "Accurate asymptotic solution for the surface field due to aperture in a conducting cylinder," *IEEE Trans. Antennas Propagat.*, vol. 33, pp. 1108-1117, Oct. 1985.
- [26] G. X. Fan and J. M. Jin, "Scattering from a cylindrically conformal slotted-waveguide array antenna," Univ. of Illinois at Urbana-Champaign, CCEM Tech. Rep. 17-96, 1996.
- [27] M. Abramowitz and I. A. Stegun, *Handbook of Mathematical Functions*. New York: Dover Publications, 1965, ch. 3.
- [28] J. R. Wait, *Electromagnetic Radiation from Cylindrical Structure*. New York: Pergamon, 1959.
- [29] T. S. Bird, "Comparison of asymptotic solution for the surface field excited by a magnetic dipole on a cylinder," *IEEE Trans. Antennas Propagat.*, vol. 32, pp. 1237-1244, Nov. 1984.
- [30] Z. W. Chang, L. B. Felsen and A. Hessel, "Surface ray methods for mutual coupling in conformal arrays on cylinder and conical surface," Polytech Inst. New York, Final Rep., 1976 (prepared under Contract N00123-76-C-0236).
- [31] S. W. Lee and S. Safavi-Naini, "Approximate asymptotic solution of surface field due to a magnetic dipole on a cylinder," *IEEE Trans. Antennas Propagat.*, vol. 26, pp. 593-597, July 1978.
- [32] P. H. Pathak and N. Wang, "Ray analysis of mutual coupling between antennas on a convex surface," *IEEE Trans. Antennas Propagat.*, vol. 29, pp. 911-922, Nov. 1981.
- [33] A. S. Goriainov, "An asymptotic solution of the problem of diffraction of a plane electromagnetic wave by a conducting cylinder," *Radio Eng. Electron.*, vol. 3, pp. 23-29, May 1958. (English translation. of *Radiotekh. i Elektron.*, vol. 3, pp. 603-614, 1958.)
- [34] N. A. Logan, "General research in diffraction theory," vols. 1 and 2, LMSD-288087, LMSD-288088, Dec. 1959.
- [35] V. A. Fock, *Electromagnetic Diffraction and Propagation Problems*. New York: Pergamon, 1965.

FIGURE CAPTIONS

Figure 1. Conformal slotted-waveguide array.

Figure 2. Division of three regions and surface magnetic currents.

Figure 3. The effect of the cylinder's curvature on the RCS in the E-plane for a 16×16 slot array with matched terminals at $f = 9.1$ GHz. (a)--- planar, — $\rho_1 = 500$ cm, (b) $\rho_1 = 200$ cm, (c) $\rho_1 = 100$ cm, (d) $\rho_1 = 50$ cm.

Figure 4. The effect of the cylinder's curvature on the RCS in the H-plane for a 16×16 slot array with matched terminals at $f = 9.1$ GHz. (a)--- planar, — $\rho_1 = 500$ cm, (b) $\rho_1 = 200$ cm, (c) $\rho_1 = 100$ cm, (d) $\rho_1 = 50$ cm.

Figure 5. RCS (dBsw) of a 16×16 slot array with shorted terminals at $f = 9.1$ GHz. (a) planar; (b) $\rho_1 = 200$ cm; (c) $\rho_1 = 100$ cm; (d) $\rho_1 = 30$ cm.

Figure 6. The effect of the terminals on the RCS of a 8×8 conformal slot array ($\rho_1 = 100$ cm). ... matched terminals, — shorted terminals. (a) E-plane pattern; (b) H-plane pattern.

Figure 7. RCS of a 8×8 conformal slot array ($\rho_1 = 50$ cm) as a function of frequency. $\theta^{inc} = 90^\circ$, $\varphi^{inc} = 45^\circ$.

Figure 8. RCS (dBsw) of a 16×16 conformal slot array ($\rho_1 = 100$ cm) at three frequencies. (a) $f = 8$ GHz; (b) $f = 9.1$ GHz; (c) $f = 12$ GHz.

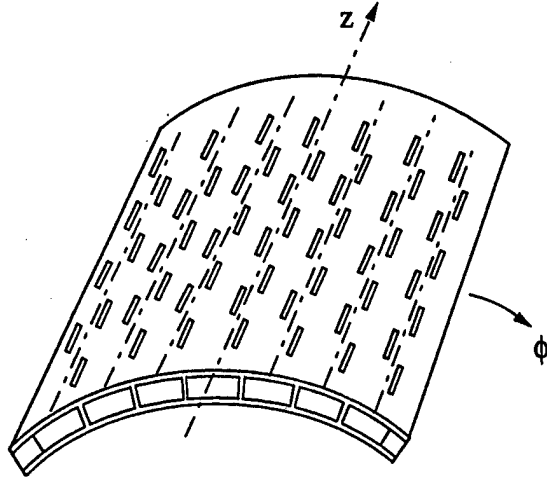


Figure 1: Conformal slotted-waveguide array.

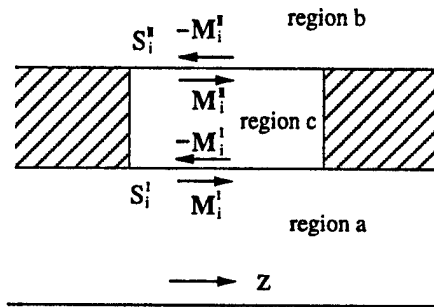
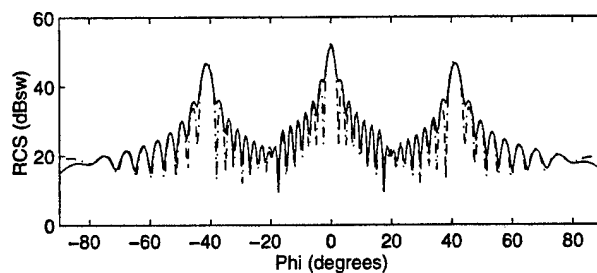
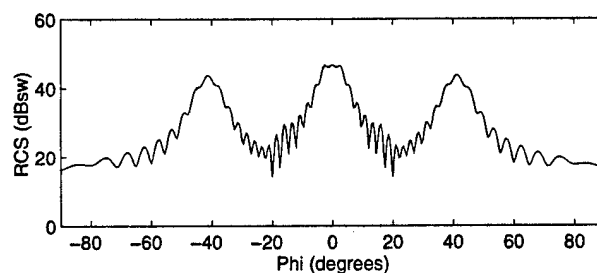


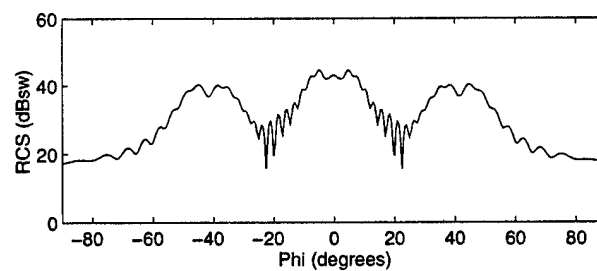
Figure 2: Division of three regions and surface magnetic currents.



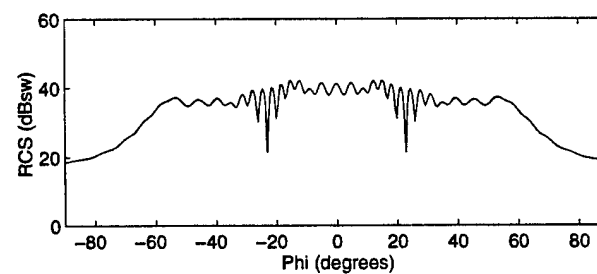
(a)



(b)

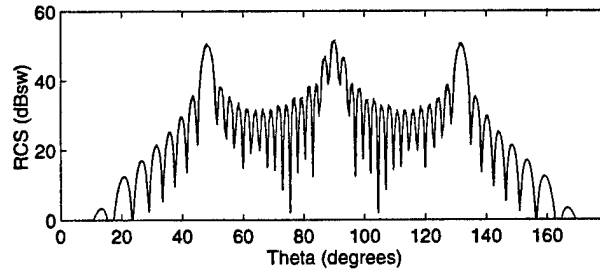


(c)

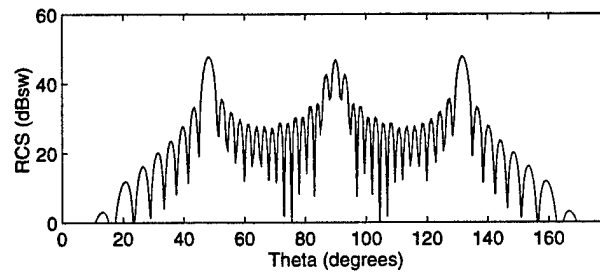


(d)

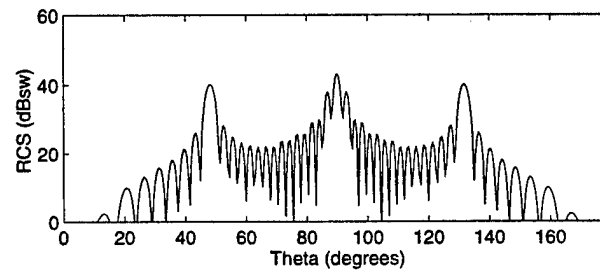
Figure 3: The effect of the cylinder's curvature on the RCS in the E-plane for a 16×16 slot array with matched terminals at $f = 9.1$ GHz. (a) \cdots planar, --- $\rho_1 = 500$ cm, (b) $\rho_1 = 200$ cm, (c) $\rho_1 = 100$ cm, (d) $\rho_1 = 50$ cm.



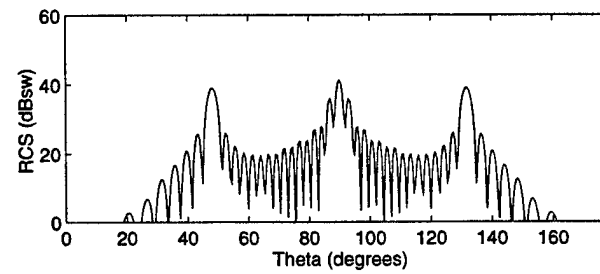
(a)



(b)



(c)



(d)

Figure 4: The effect of the cylinder's curvature on the RCS in the H-plane for a 16×16 slot array with matched terminals at $f = 9.1$ GHz. (a)--- planar, — $\rho_1 = 500$ cm, (b) $\rho_1 = 200$ cm, (c) $\rho_1 = 100$ cm, (d) $\rho_1 = 50$ cm.

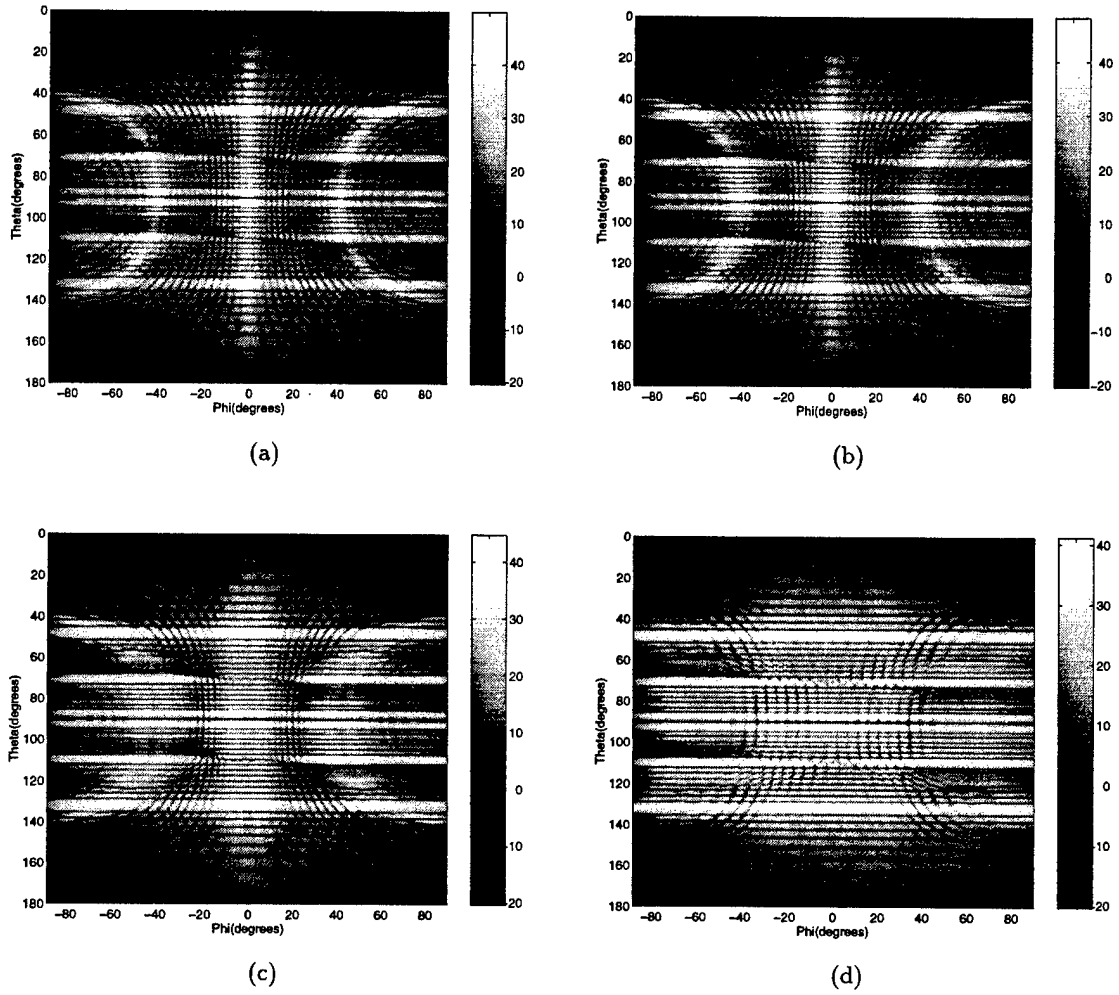
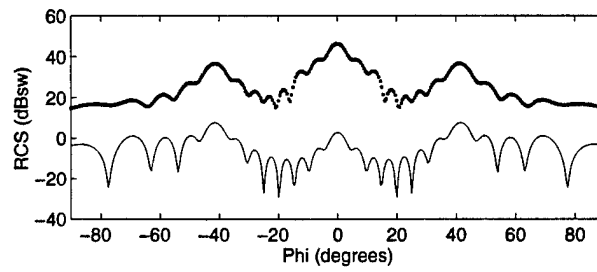
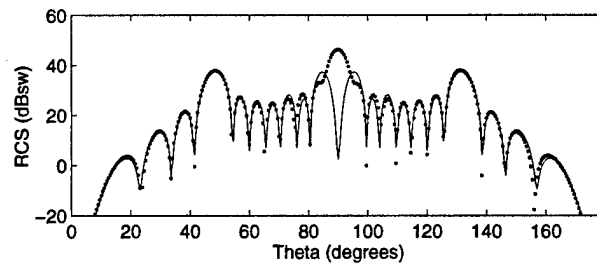


Figure 5: RCS (dBsw) of a 16×16 slot array with shorted terminals at $f = 9.1$ GHz. (a) planar; (b) $\rho_1 = 200$ cm; (c) $\rho_1 = 100$ cm; (d) $\rho_1 = 30$ cm.

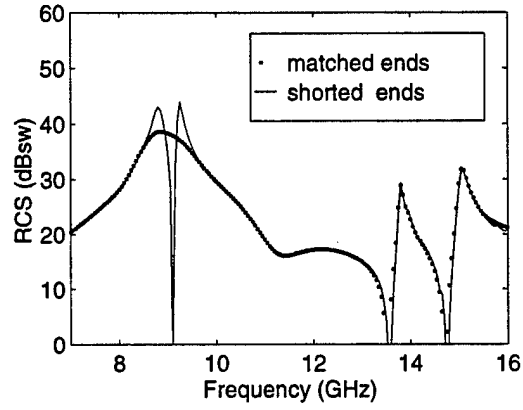


(a)

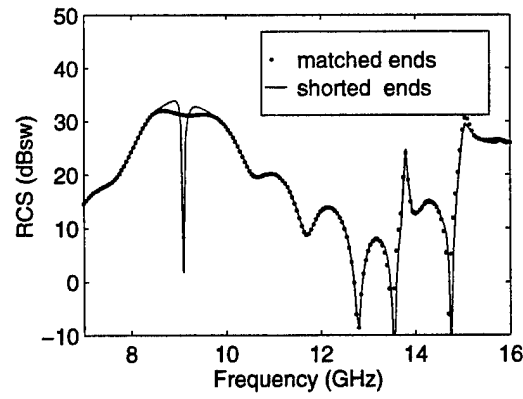


(b)

Figure 6: The effect of the terminals on the RCS of a 8×8 conformal slot array ($\rho_1 = 100$ cm). \cdots matched terminals, $—$ shorted terminals. (a) E-plane pattern; (b) H-plane pattern.

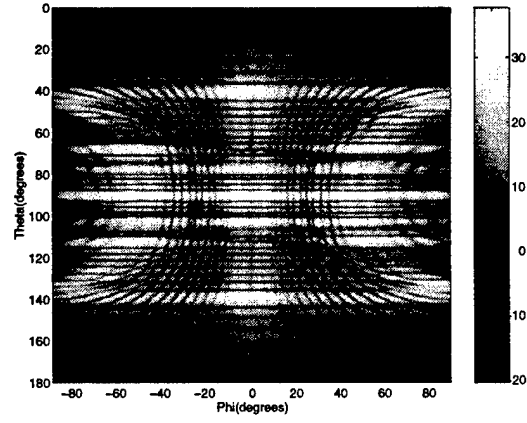


(a)

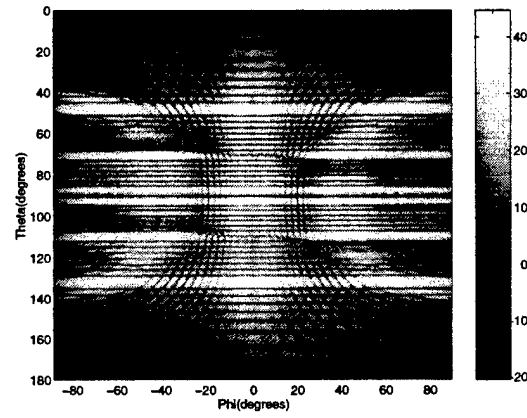


(b)

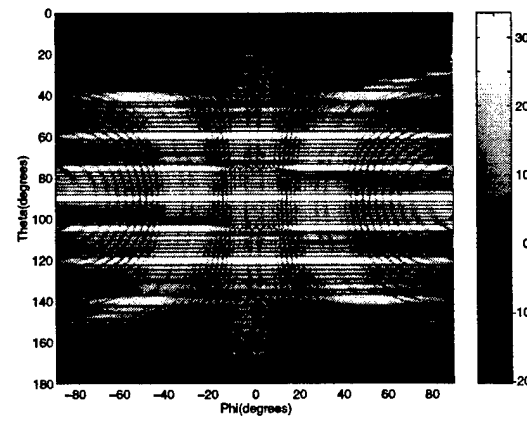
Figure 7: RCS of a 8×8 conformal slot array ($\rho_1 = 50$ cm) as a function of frequency. (a) $\theta^{inc} = 90^\circ$, $\varphi^{inc} = 0^\circ$; (b) $\theta^{inc} = 90^\circ$, $\varphi^{inc} = 45^\circ$.



(a)



(b)



(c)

Figure 8: RCS (dBsw) of a 16×16 conformal slot array ($\rho_1 = 100$ cm) at three frequencies. (a) $f = 8$ GHz; (b) $f = 9.1$ GHz; (c) $f = 12$ GHz.

APPENDIX 3

Hybrid MoM/SBR Method to Compute Scattering from a Slot Array Antenna in a Complex Geometry

Andrew D. Greenwood and Jian-Ming Jin

Center for Computational Electromagnetics

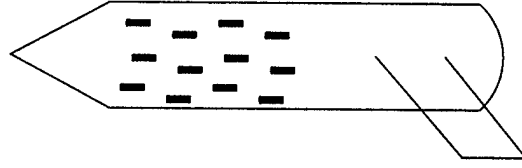
University of Illinois

Urbana, Illinois 61801

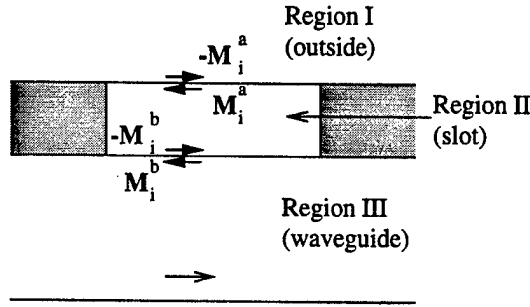
1 Introduction

The presence of a slotted waveguide array antenna on a radar target may have a significant contribution to the overall radar cross-section (RCS) of the target. Therefore, the computation of the RCS should include the scattering from the slot array. Recently, a method of moments (MoM) procedure has been introduced to compute the scattering from a cylindrically conformal slotted-waveguide array antenna [1, 2]. However, this procedure does not take into account the geometry in which the slot array is located. If the slot array is located in a complex, three dimensional (3-D) geometry, the MoM cannot efficiently account for the effect of the geometry. A more efficient method to compute the scattering from a large, 3-D body is the high frequency shooting and bouncing ray (SBR) method. However, this method cannot accurately account for the slots, each of which is typically smaller than an electromagnetic wavelength in size. In this paper, the MoM computation of the scattering from a slot array is hybridized with the SBR method to compute the electromagnetic scattering from a large, 3-D target which includes a slot array antenna.

The basis of the hybrid method is the field equivalence principle, which allows the scattering geometry to be decomposed into separate regions. The MoM is applied to the slotted waveguides, while the SBR method is applied to the region outside the waveguides, which includes the complex, 3-D target. By using the hybrid method, the scattering from a large, 3-D target, which includes a slotted-waveguide array antenna, can be efficiently and accurately computed.



(a) Large target



(b) Local slot geometry

Figure 1: Example of a complex, 3-D target with a slot array antenna and the local slot geometry.

The remainder of this paper is divided into five sections. Section 2 describes the formulation of the problem, including the use of the MoM, the use of the SBR method, and techniques to decouple the computations of the two methods. Section 3 describes briefly how the method has been tested, and Section 4 gives some numerical results which show the capability of the method. The results in Section 4 also demonstrate the need to include the slot array in scattering computations. Finally, Section 5 gives a brief conclusion.

2 Formulation

Consider the example target shown in Figure 1a. The target is complex and 3-D, and it includes a slotted waveguide array antenna on its surface. The slotted waveguide array antenna may be planar, or it may conform to the surface of a cylinder. The first step to compute the scattering from this target is to analyze the slotted waveguides using the MoM. Then, the scattering from the target with the slot apertures covered by perfect electric conductor (PEC) is computed using

the SBR method. During the SBR calculation, the incident field on the slot array antenna is computed and stored. This incident field is combined with the MoM analysis to find an equivalent magnetic current on the outer aperture of each slot. Finally, the radiation of these equivalent magnetic currents in the presence of the complex, 3-D target is computed using the reciprocity theorem. This result is added to the previously computed SBR scattering result.

2.1 Use of MoM

The first step in the formulation of the problem is to analyze the slotted waveguides using the MoM. There are two main steps in the application of the MoM. First, the problem must be described in terms of an integral equation. Then, the integral equation is discretized to find a numerical solution. The steps are outlined here, and more detail is given in [1, 2].

To derive the integral equation, the apertures of each slot are first covered with PEC, and equivalent magnetic currents over each aperture are introduced. Figure 1b depicts the situation for the i^{th} slot. The region outside of the antenna is denoted Region I, the region inside the slot is Region II, and the region outside of the slot but inside the waveguide is Region III. An equivalent magnetic current \mathbf{M}_i^a is introduced on the inside of the outer slot aperture (between Regions I and II), and the equivalent current \mathbf{M}_i^b is introduced on the waveguide side of the inner aperture (between Regions II and III). Because the electric field must be continuous across each aperture, $-\mathbf{M}_i^a$ must be introduced on the outside of the outer aperture, and $-\mathbf{M}_i^b$ must be introduced on the slot side of the inner aperture. Note that when the analysis is complete, $-\mathbf{M}_i^a$ are the currents that radiate in the presence of the complex, 3-D body as discussed above.

To derive the integral equation, the continuity of the tangential magnetic field across each aperture is enforced. Denoting the tangential magnetic field in Region III on the i^{th} slot aperture due to the magnetic current on the j^{th} aperture as $\mathbf{H}_{\tau i}^{III}(\mathbf{M}_j^b)$, the following must hold on each inner aperture:

$$\sum_j \mathbf{H}_{\tau i}^{III}(\mathbf{M}_j^b) + \mathbf{H}_{\tau i}^{II}(\mathbf{M}_i^b) - \mathbf{H}_{\tau i}^{II}(\mathbf{M}_i^a) = 0. \quad (1)$$

Further, denoting the tangential incident field on the i^{th} slot aperture as $\mathbf{H}_{\tau i}^{SBR}$,

$$\sum_j \mathbf{H}_{\tau i}^I(\mathbf{M}_j^a) + \mathbf{H}_{\tau i}^{II}(\mathbf{M}_i^a) - \mathbf{H}_{\tau i}^{II}(\mathbf{M}_i^b) = \mathbf{H}_{\tau i}^{SBR} \quad (2)$$

must hold on each outer slot aperture. Note that the incident fields are calculated using the SBR method, and the magnetic field due to a magnetic current is found from

$$\mathbf{H}^\alpha(\mathbf{M}) = \iint_S \overline{\overline{\mathbf{G}}}^\alpha(\mathbf{r}, \mathbf{r}') \cdot \mathbf{M}(\mathbf{r}') dS' \quad (3)$$

where α is I, II, or III, depending on the region of interest, $\overline{\overline{\mathbf{G}}}^\alpha(\mathbf{r}, \mathbf{r}')$ is the magnetic source-magnetic field dyadic Green's function in the appropriate region, and \mathbf{r} corresponds to the point at which the magnetic field is to be evaluated. Combining Equations 1, 2, and 3 gives an integral equation for the magnetic currents.

The second main step in application of the MoM is to discretize the integral equation to find a numerical solution for the currents. To accomplish this step, the currents are expanded in terms of sinusoidal basis functions. Defining $\hat{\xi}$ to be the direction parallel to the lengths of the slots and using a local coordinate system in which $\xi_j = 0$ at one end of the j^{th} slot, the current on the j^{th} slot aperture is expanded as

$$\mathbf{M}_j^\beta = \hat{\xi} \sum_{q=1}^N V_{qj}^\beta \sin\left(\frac{q\pi}{L_j} \xi_j\right) \quad (4)$$

where N is the number of terms in the expansion, and β represents a for the current on the outer aperture or b for the current on the inner aperture. Equation 4 is valid for points on the j^{th} slot aperture; for points outside of the aperture, the expansion is defined to be zero. Assuming the width of a slot is much less than its length, the $\hat{\xi}$ component of the current is the only component of interest.

Substituting the expansion given in Equation 4 into the integral equation allows the integral equation to be converted to a matrix equation which can be solved numerically. For the more details about solving the integral equation, the reader is referred to [1, 2]. However, one important step that should be mentioned here is the derivation of the dyadic Green's functions for the various regions. The Green's functions given in [1, 2] for Regions II and III are applicable to the present problem. For Region I, the dyadic Green's function can be written as

$$\overline{\overline{\mathbf{G}}}^I(\mathbf{r}, \mathbf{r}') = \overline{\overline{\mathbf{G}}}^{\text{cyl}}(\mathbf{r}, \mathbf{r}') + \overline{\overline{\mathbf{G}}}^{\text{diff}}(\mathbf{r}, \mathbf{r}'). \quad (5)$$

The Green's function given in [1, 2] for the exterior region corresponds to $\overline{\overline{\mathbf{G}}}^{\text{cyl}}(\mathbf{r}, \mathbf{r}')$, and $\overline{\overline{\mathbf{G}}}^{\text{diff}}(\mathbf{r}, \mathbf{r}')$ is a perturbation term due to diffraction and reflection by the

complex target in which the slot array is embedded. Neglecting $\overline{\overline{G}}^{\text{diff}}(\mathbf{r}, \mathbf{r}')$ neglects fields which are scattered by the slots, diffracted or reflected by the large body back to the slots, and scattered by the slots again [3]. These fields are usually an insignificant part of the scattering, and this term is neglected in the computations. Thus, the Green's function given in [1,2] for Region I is used for the present problem.

2.2 Use of SBR

As previously mentioned, the MoM is used to analyze the slot array antenna while the SBR method is used for the remainder of the problem. Thus, there are three main tasks to be accomplished by the SBR method: to compute the scattering from the complex, 3-D target, to compute the incident magnetic fields on the slot apertures, and to compute the radiation of the equivalent currents on the slot apertures in the presence of the complex, 3-D target. In all of these cases, the slot apertures are covered with PEC.

In the SBR method, a dense grid of rays, corresponding to a plane wave, is launched toward the target, and each ray is traced as it bounces around the target. The bounces are governed by Geometrical Optics (GO), and as each ray leaves the target, its contribution to the scattering is computed by a Physical Optics (PO) integration. If more accuracy is desired, the first order edge diffracted terms are computed using the Geometrical Theory of Diffraction (GTD) and added to the result [3-6]. For the present problem, this SBR procedure is followed to compute the scattering from the complex, 3-D target with the slot apertures closed by PEC. The SBR procedure is implemented using the XPATCH software package [4,5].

The incident magnetic field on the slot apertures is computed using SBR at the same time the scattering from the complex, 3-D target is computed. While tracing the rays to find the scattering, some rays will hit on or near a slot aperture. The field contributions from each of these rays are combined with appropriate phase shifts to find the incident magnetic field on each slot aperture. The incident magnetic fields on the slot apertures are used by the MoM to compute the equivalent magnetic currents on the apertures.

The remaining step in the problem is to compute the radiation of the magnetic currents in the presence of the large body. The SBR method together with the

reciprocity theorem is employed for this task [3, 6]. Consider an infinitesimal dipole placed at the scattering observation point. If the target containing the slot array is in the far field of the dipole, the dipole launches a plane wave toward this target. Recall that for the SBR method, the grid of rays launched toward the target corresponds to a plane wave. Note also that the reciprocity theorem states

$$\iiint_V \mathbf{E}^{\text{Slot}} \cdot \mathbf{J} dV = \iint_S \mathbf{H}_\tau^{\text{SBR}} \cdot \mathbf{M}^a \quad (6)$$

where $\mathbf{H}_\tau^{\text{SBR}}$ is the incident field on the slot apertures due to the dipole at the scattering observation point, \mathbf{M}^a is the current on the outer slot apertures, which is found using the MoM, \mathbf{E}^{Slot} is the radiation due to $-\mathbf{M}^a$, and \mathbf{J} is the dipole current. Thus, if the dipole current (\mathbf{J}) is appropriately chosen and monostatic scattering is being computed, all components to find \mathbf{E}^{Slot} using reciprocity are computed already. If bistatic scattering results are desired, $\mathbf{H}_\tau^{\text{SBR}}$ resulting from a dipole at the scattering observation point must be computed first, then \mathbf{E}^{Slot} can be computed.

2.3 Decoupling the MoM from the SBR Method

As they are presented in Section 2.1, the MoM computations are coupled to the SBR method computations. This is due to the fact that the incident magnetic field on the slot apertures, which is computed using the SBR method, is required for the MoM computations. To avoid having to repeat the MoM computations in order to analyze the scattering from many different incidence angles, it is desirable to decouple the computations of the two methods. There are two ways of doing this. The first method preserves the coupling interactions between different slots; the second involves an approximation which neglects the coupling between different slots to achieve lower computational complexity.

To decouple the MoM computations from the SBR computations while preserving the coupling between the various slots, the incident magnetic field on the slot apertures can be expanded in terms of basis functions. Assuming that the width of a slot is much less than its length, the component of the incident magnetic field along the length of a slot is the only component of interest. A convenient basis set is the set of pulse basis functions, where the i^{th} basis function is defined to be one on the i^{th} slot aperture and zero elsewhere. There will be n basis functions

in the set, where n is the number of slots in the array. The magnetic currents on each slot aperture are then computed with the incident field on the slot array set equal to each of the n basis functions in turn. A matrix-vector multiply is then carried out during the SBR computations. This matrix-vector multiply converts the incident magnetic fields on the slot apertures to the equivalent currents on the apertures.

The second method of decoupling the MoM computations from the SBR computations neglects the coupling between the individual slots. One slot on the slot array is chosen, and it is assumed that this slot is the only slot present. The MoM computation is carried out with a magnetic field of unit amplitude on this slot, and the result is a magnetic current for the slot. It is then assumed that all of the slots in the array are equivalent; the magnetic current on each slot is set equal to the magnetic field on that slot times the single magnetic current which is computed by the MoM. This approximation reduces the computational complexity and the sizes of data files. However, it does not produce accurate results when the frequency is near the working frequency of the slot array. This is demonstrated in Section 4.

3 Testing

Before using any new numerical technique, the technique should be tested against existing techniques to ensure its validity. The validity of the MoM computation involving the coupling between the different slots in the array is validated by comparison with previous MoM and finite element method (FEM) techniques [2, 7]. The SBR method is also validated through extensive, previous testing [4, 5]. The hybrid technique is validated by comparison with a previous hybrid method to compute the scattering from complex targets with cracks and cavities on their surfaces [3]. This is accomplished by considering a waveguide with a single slot on its surface. The slotted waveguide is placed on a large plate, and the problem is modeled both with the hybrid MoM/SBR method discussed in this paper and with the hybrid FEM/SBR method presented in [3]. The two solutions show good agreement.

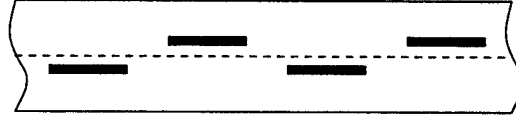


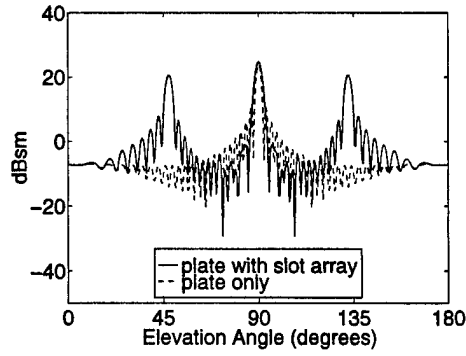
Figure 2: Configuration of the slots on the surface of a waveguide.

4 Numerical Examples

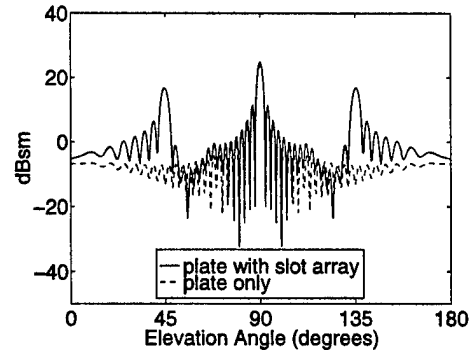
To show the validity and utility of the proposed technique, several numerical results are presented. For all of the numerical examples, the slot array contains 16 waveguides with 16 slots on each waveguide, and the array is designed to radiate at 9.1 GHz. In addition, the following parameters apply to all of the examples presented: the upper waveguide wall in which the slots are cut is 0.08 cm thick, the waveguides are separated by walls 0.1cm thick, each slot is 1.6 cm long and 0.16 cm wide, and the slots are positioned on the waveguide surface as shown in Figure 2, where the offset of each slot from the center of the waveguide is 0.15 cm. Unless otherwise noted, the coupling between individual slots in the array is included in the results.

The first example is a planar slot array which is in a simple ground plane geometry. The waveguides are 2.230 cm wide by 1.016 cm high, the slot centers are 2.444 cm apart, and the first and last slots centers are 1.222 cm from the ends of the waveguides. Thus, the entire slot array and the ground plate are 37.3 cm wide by 39.1 cm long. In Figure 3, the radar cross-section (RCS) of the plate with the slots is superimposed on the scattering from the plate alone. The scattering frequency is 9.1 GHz, which is the working frequency of the slot array. Figure 3 shows results in both the H -plane and the E -plane and for waveguides which are terminated both with matched loads and with short circuits. For some incidence angles, the slot array has a dominant effect on the scattering.

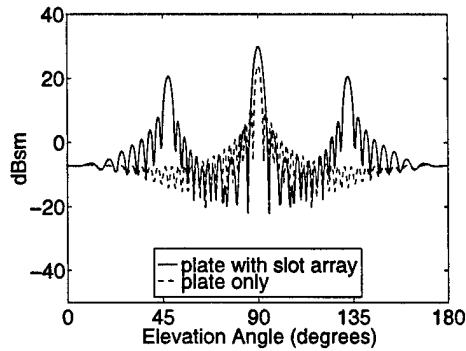
The second example is a slot array on a cylinder with a nose cone. The radius of the cylinder is 16.096 cm, and the length without the nose cone is 100 cm. The nose cone is 30 cm long. The waveguide cross-sections are sectoral in shape and are 1.016 cm thick. Along the slotted surface, the waveguides are 2.230 cm wide. The slots are 2.573 cm apart, and the first and last slots are 1.287 cm from the ends of the waveguides. The entire slot array is 37.3 cm along the circumference of the cylinder and 41.2 cm along the axis of the cylinder. In Figure 4, the H -plane



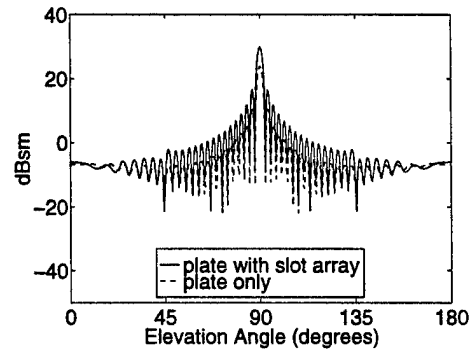
(a) *H*-plane, matched waveguide loads



(b) *E*-plane, matched waveguide loads



(c) *H*-plane, short-circuit waveguide loads

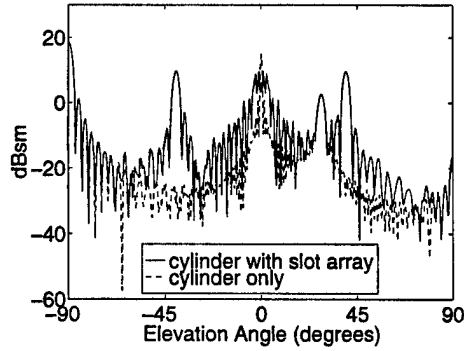


(d) *E*-plane, short-circuit waveguide loads

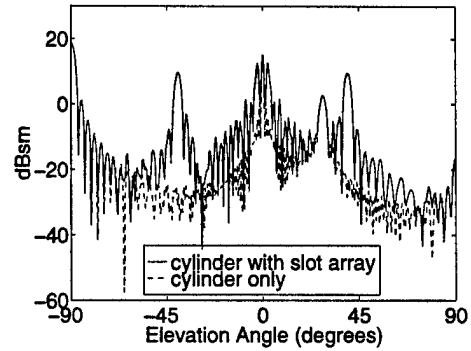
Figure 3: RCS of a planar slot array on a ground plate at 9.1 GHz, the working frequency of the slot array.

RCS of the cylinder alone and the RCS of the cylinder with the slot array are compared. Again, the scattering frequency is 9.1 GHz, the working frequency of the slot array, and again, there are scattering directions for which the slot array dominates the return.

The next example is intended to show the effect of the uncoupled slot approximation which was discussed in Section 2.3. Figure 5 shows the RCS of the same geometry considered in the second example, but as a function of frequency. The incident direction is 40° in the *H*-plane. The RCS computed considering the coupling between individual slots is plotted with the RCS computed by neglecting the slot coupling. The approximation neglecting slot coupling is reasonably accurate

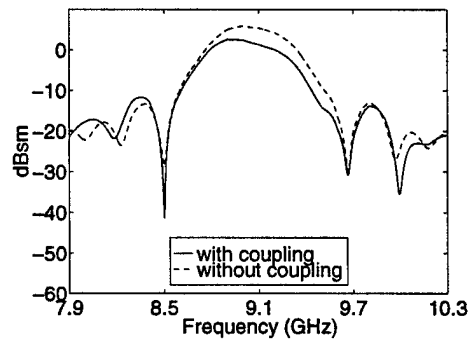


(a) Matched waveguide loads

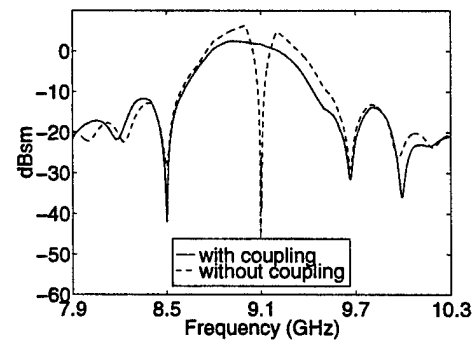


(b) Short-circuit waveguide loads

Figure 4: RCS of a conformal slot array on a cylinder with a nose cone at 9.1 GHz, the working frequency of the slot array.



(a) Matched waveguide loads



(b) Short-circuit waveguide loads

Figure 5: RCS of a conformal slot array on a cylinder with a nose cone. The scattering is computed with and without including the coupling between individual slots. Near the working frequency of the slot array (9.1 GHz), the slot coupling must be included.

away from the working frequency of the slot array antenna, but there is significant error near the working frequency. Thus, this approximation must be applied with care.

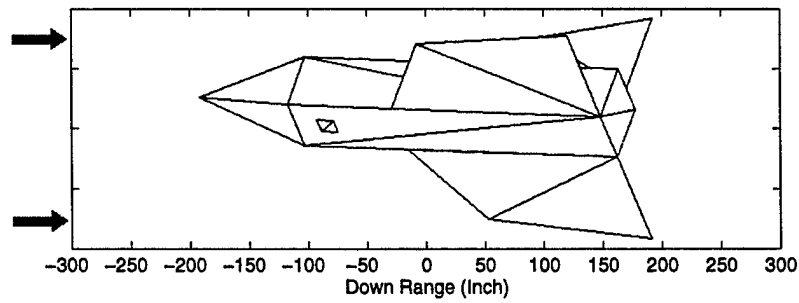
The final example shows the usefulness of the method. The slot array antenna from the first example is mounted on the belly of an f309 aircraft, with the lengths of the slots perpendicular the the length of the aircraft body (see Figure 6a). Figure 6b shows the VV -polarized range profile of the airplane both with and without the slot array. The range profile is the time domain response to an incident sinc pulse. The sinc pulse in this example has a center frequency of 10 GHz and a bandwidth of 2 GHz, and the slot array has matched waveguide loads. The slot scattering dominates the range profile.

5 Conclusion

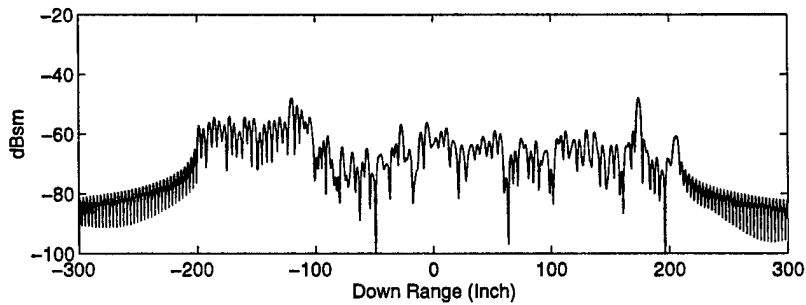
A hybrid MoM/SBR method is developed to compute the scattering from a complex, 3-D target with a slotted waveguide array antenna. Because the target is large and 3-D, the MoM alone cannot efficiently compute the scattering, and because the slots on the waveguides are small features, the SBR method alone is not accurate. The hybrid method combines the two individual methods in such a manner that the scattering can be efficiently and accurately computed. In the hybrid method, the MoM is used to model the details of the slot array, and the SBR method is used to model the electromagnetic interactions with the large, complex target. The method is validated by comparison to previously published methods. Numerical examples show the need to include a slot array model when computing the scattering from a complex target with a slotted waveguide array. The examples also illustrate the capability of the method.

Acknowledgements: This work was supported by the Office of Naval Research under grant N00014-95-1-0848 and by NASA under grant NAG3-1474.

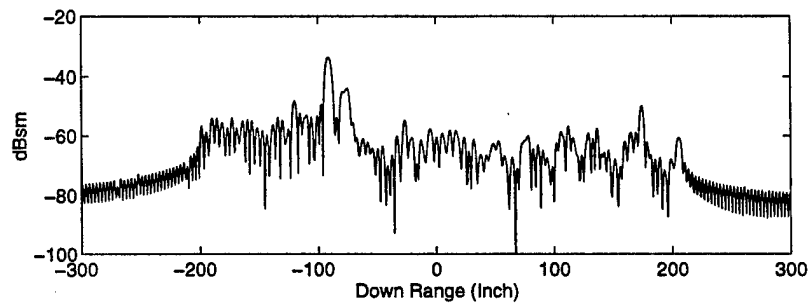
Dr. G. X. Fan's contribution to the development of the computer code for slot array scattering is acknowledged.



(a) f309 with slot array



(b) Range profile without slot array.



(c) Range profile with slot array.

Figure 6: Range profile of an f309, VV-polarization, 10 GHz center frequency, 2 GHz bandwidth. The slot array has matched waveguide loads.

References

- [1] G. Fan and J. M. Jin, "Scattering from a cylindrically conformal slotted-waveguide array antenna," *IEEE Antennas and Propagation Society International Symposium Digest*, pp. 1394-1397, 1996.
- [2] G. X. Fan and J. M. Jin, "Scattering from a cylindrically conformal slotted-waveguide array antenna," *IEEE Trans. Antennas Propagat.*, 1996, Submitted to.
- [3] J. M. Jin, S. S. Ni, and S. W. Lee, "Hybridization of sbr and fem for scattering by large bodies with cracks and cavities," *IEEE Trans. Antennas Propagat.*, vol. 43, no. 10, pp. 1130-1139, Oct. 1995.
- [4] S. W. Lee, D. J. Andersh, D. D. Reeves, S. K. Jeng, H. Ling, Y. Chu, D. P. Sullivan, and C. L. Yu, "User manual for xpatch," DEMACO, Inc., Champaign, IL, 1993.
- [5] D.J. Andersh, M. Hazlett, S. W. Lee, D. D. Reeves, D. P. Sullivan, and Y. Chu, "Xpatch: A high-frequency electromagnetic-scattering prediction code and environment for complex three-dimensional objects," *IEEE Antennas Propagat. Mag.*, vol. 36, no. 1, pp. 65-69, Feb. 1994.
- [6] A. D. Greenwood, S. S. Ni, J. M. Jin, and S. W. Lee, "Hybrid fem/sbr method to compute the radiation pattern from a microstrip patch antenna in a complex geometry," *Microwave and Optical Technology Letters*, vol. 13, no. 2, pp. 84-87, Oct. 1996.
- [7] J. Chen and J. M. Jin, "Electromagnetic scattering from slot antennas on waveguides with arbitrary terminations," *Microwave and Optical Technology Letters*, vol. 10, no. 5, pp. 286-291, Dec. 1995.

APPENDIX 4

On the Formulation of Hybrid Finite-Element and Boundary-Integral Method for 3D Scattering

X. Q. Sheng, J. M. Jin, J. M. Song, C. C. Lu, and W. C. Chew

Center for Computational Electromagnetics

Department of Electrical and Computer Engineering

University of Illinois at Urbana-Champaign

Urbana, Illinois 61801-2991

Abstract—This paper studies in detail a variety of formulations for the hybrid finite-element and boundary-integral (FE-BI) method for three-dimensional (3D) electromagnetic scattering by inhomogeneous objects. It is shown that the efficiency and accuracy of the FE-BI method depend highly on the formulation and discretization of the boundary-integral equation (BIE) used. A simple analysis of matrix condition identifies the efficiency of the different FE-BI formulations and an analysis of weighting functions shows that the traditional FE-BI formulations cannot produce accurate solutions. A new formulation is then proposed and numerical results show that the resulting solution has a good efficiency and accuracy and is completely immune to the problem of interior resonance.

I. INTRODUCTION

The hybrid finite-element and boundary-integral (FE-BI) method is a powerful numerical technique for computing scattering by inhomogeneous objects. The method first divides the problem into an interior and exterior problems. The field in the interior region is formulated using the finite-element method (FEM), and the field in the exterior region is represented by a boundary-integral equation (BIE). The interior and exterior fields are then coupled by the field continuity conditions.

The hybrid FE-BI method has been first applied to two-dimensional (2D) scattering problems [1]–[6] and later extended to more challenging three-dimensional (3D) scattering problems [7]–[14]. To be more specific, Paulsen *et al* [7] developed the first FE-BI formulation for a general 3D scattering problem, which employed node-based FEM to discretize the interior fields and used either the electric-field integral equation (EFIE) or the magnetic-field integral equation (MFIE) as BIE to represent the exterior field. The formulation, however, exhibited two major drawbacks. First, it inherited all the difficulties caused by the use of node-based elements to discretize the electric and magnetic fields directly [15]. These difficulties include the treatment of dielectric interfaces and sharp conducting edges and corners and the appearance of spurious solutions. Second, it failed at the interior resonant frequencies, which are defined as the resonant frequencies of a cavity formed by covering the surface where BIE applies with a perfect conductor and filling its interior with the exterior medium. The first difficulty was removed by the use of edge-based FEM [8], [9], [12]–[14] and the second difficulty was alleviated by the use of the combined field integral equation (CFIE), which is a linear combination of EFIE and MFIE [10]–[12], [14].

Although the FE-BI method with the implementation of edge-based elements and CFIE is remarkably more powerful than other numerical techniques in dealing with inhomogeneous objects, it still has a bottleneck which is the full matrix generated by BIE. As pointed out in [16], this bottleneck severely limits the capability of the FE-BI method in dealing with large objects. Although this problem can be circumvented in some special problems [9], [16] or partially alleviated using special surfaces to separate the interior and exterior regions [11], [14], no efficient method has been developed for general 3D problems so far.

Our renewed interest in the FE-BI method originated from the recent development of the fast multipole method (FMM) [17] and the multilevel fast multipole algorithm (MLFMA) [18]. Our objective is to apply MLFMA to BIE to completely remove the bottleneck in the FE-BI method for general 3D problems. During the

course of pursuing this goal, we have encountered several problems associated with the efficiency and accuracy of the FE-BI method implemented using the edge-based elements and CFIE. This paper reports our study of these problems.

In this paper, we first formulate the general FE-BI method for 3D scattering problems. We then show that there are several different approaches to the discretization of CFIE, yielding solutions of different efficiency and accuracy. However, none of the traditional approaches produces satisfactory results. The cause is determined and a new formulation is proposed. Furthermore, we show that, contrary to the common belief, not all CFIE formulations are immune to the problem of interior resonance; however, the new one is.

II. FORMULATION AND ANALYSIS

Consider the problem of electromagnetic wave scattering by an arbitrarily-shaped and inhomogeneous body characterized by relative permittivity and permeability (ϵ_r, μ_r) , which can be complex if the body is lossy. To solve this problem using the FE-BI method, we first introduce an artificial surface S (which can be the surface of the body) to enclose the body and divide the problem into an interior and exterior ones. The field inside S can be formulated into an equivalent variational problem with the functional given by [15]

$$F(\mathbf{E}) = \frac{1}{2} \int_V \left[\frac{1}{\mu_r} (\nabla \times \mathbf{E}) \cdot (\nabla \times \mathbf{E}) - k_0^2 \epsilon_r \mathbf{E} \cdot \mathbf{E} \right] dV + jk_0 \int_S (\mathbf{E} \times \bar{\mathbf{H}}) \cdot \hat{n} dS \quad (1)$$

where V denotes the volume enclosed by S , \hat{n} denotes the outward unit normal to S , k_0 is the free-space wavenumber, and $\bar{\mathbf{H}} = Z_0 \mathbf{H}$ with Z_0 being the free-space intrinsic impedance. Using FEM with edge elements, we obtain the matrix equation

$$\begin{bmatrix} K_{II} & K_{IS} & 0 \\ K_{SI} & K_{SS} & B \end{bmatrix} \begin{Bmatrix} E_I \\ E_S \\ \bar{H}_S \end{Bmatrix} = \begin{Bmatrix} 0 \\ 0 \\ 0 \end{Bmatrix} \quad (2)$$

where $\{E_I\}$ is a vector containing the discrete electric fields inside V , $\{E_S\}$ and $\{\bar{H}_S\}$ are the vectors containing the discrete electric and magnetic fields on S , respectively. Furthermore, $[K_{II}]$, $[K_{IS}]$, $[K_{SI}]$, $[K_{SS}]$, and $[B]$ are sparse matrices and, in particular, $[K_{II}]$ and $[K_{SS}]$ are symmetric and $[K_{IS}] = [K_{SI}]^T$, where the superscript T denotes the transpose.

Equation (2) cannot be solved unless a relation between $\{E_S\}$ and $\{\bar{H}_S\}$ is specified. Such a relation is provided by BIE for the exterior field, whose discretization yields

$$[P]\{E_S\} + [Q]\{\bar{H}_S\} = \{b\} \quad (3)$$

where $\{b\}$ is a vector related to the incident field. Combining (2) and (3), we obtain the complete system

$$\begin{bmatrix} K_{II} & K_{IS} & 0 \\ K_{SI} & K_{SS} & B \\ 0 & P & Q \end{bmatrix} \begin{Bmatrix} E_I \\ E_S \\ \bar{H}_S \end{Bmatrix} = \begin{Bmatrix} 0 \\ 0 \\ b \end{Bmatrix} \quad (4)$$

which can be solved for the field inside V and on S .

Whereas the generation of (2) using FEM is standard, the generation of (3) using MoM can take many different forms. The basic equations for generating (3) are the electric-field integral equation (EFIE) given by

$$\mathbf{L}(\bar{\mathbf{J}}) - \mathbf{K}(\mathbf{M}) = \mathbf{E}^i \quad (5)$$

and the magnetic-field integral equation (MFIE) given by

$$\mathbf{K}(\bar{\mathbf{J}}) + \mathbf{L}(\mathbf{M}) = \bar{\mathbf{H}}^i \quad (6)$$

where $\bar{\mathbf{J}}$ and \mathbf{M} are related to the fields on S by $\mathbf{J} = \hat{n} \times \bar{\mathbf{H}}$ and $\mathbf{M} = \mathbf{E} \times \hat{n}$, respectively, and $(\mathbf{E}^i, \bar{\mathbf{H}}^i)$ denote the incident fields. The operators \mathbf{L} and \mathbf{K} are defined as

$$\mathbf{L}(\mathbf{X}) = jk_0 \int_S \left[\mathbf{X}(\mathbf{r}') + \frac{1}{k_0^2} \nabla \nabla' \cdot \mathbf{X}(\mathbf{r}') \right] G(\mathbf{r}, \mathbf{r}') dS' \quad (7)$$

$$\mathbf{K}(\mathbf{X}) = T\mathbf{Y}(\mathbf{r}) + \oint_S \mathbf{X}(\mathbf{r}') \times \nabla G(\mathbf{r}, \mathbf{r}') dS' \quad (8)$$

where \mathbf{Y} is related to \mathbf{X} by $\mathbf{X} = \hat{n} \times \mathbf{Y}$ and

$$G(\mathbf{r}, \mathbf{r}') = \frac{e^{-jk_0 R}}{4\pi R} \quad (9)$$

in which $R = |\mathbf{r} - \mathbf{r}'|$. The bar integral symbol is used to denote the principal value and the parameter T is given by $T = 1 - \Omega/4\pi$ where Ω is the solid angle subtended by the observation point [19]. For a smooth surface, $\Omega = 2\pi$ and $T = 1/2$.

Equations (5) and (6) can be discretized by first expanding \mathbf{J} and \mathbf{M} as

$$\bar{\mathbf{J}} = \sum_{i=1}^{N_S} \mathbf{g}_i \bar{H}_i \quad (10)$$

$$\mathbf{M} = \sum_{i=1}^{N_S} \mathbf{g}_i E_i \quad (11)$$

where N_S denotes the total number of edges on S and \mathbf{g}_i denotes the RWG vector basis functions [20], which are completely compatible with the vector basis functions for the edge elements. Substituting (10) and (11) into (5) and using \mathbf{g}_i as the weighting function, we obtain the TE formulation (short for $\hat{\mathbf{t}} \cdot \mathbf{E}$ where $\hat{\mathbf{t}}$ denotes a unit vector tangential to S)

$$[P^{TE}]\{E_S\} + [Q^{TE}]\{\bar{H}_S\} = \{b^{TE}\} \quad (12)$$

where

$$P_{ij}^{TE} = - \int_S \mathbf{g}_i \cdot \mathbf{K}(\mathbf{g}_j) dS \quad (13)$$

$$Q_{ij}^{TE} = \int_S \mathbf{g}_i \cdot \mathbf{L}(\mathbf{g}_j) dS \quad (14)$$

$$b_i^{TE} = \int_S \mathbf{g}_i \cdot \mathbf{E}^i dS. \quad (15)$$

Similarly, from (6) we obtain the TH formulation (short for $\hat{\mathbf{t}} \cdot \mathbf{H}$)

$$[P^{TH}]\{E_S\} + [Q^{TH}]\{\bar{H}_S\} = \{b^{TH}\} \quad (16)$$

where

$$P_{ij}^{TH} = \int_S \mathbf{g}_i \cdot \mathbf{L}(\mathbf{g}_j) dS = Q_{ij}^{TE} \quad (17)$$

$$Q_{ij}^{TH} = \int_S \mathbf{g}_i \cdot \mathbf{K}(\mathbf{g}_j) dS = -P_{ij}^{TE} \quad (18)$$

$$b_i^{TH} = \int_S \mathbf{g}_i \cdot \bar{\mathbf{H}}^i dS. \quad (19)$$

Alternatively, we may choose $\hat{\mathbf{n}} \times \mathbf{g}_i$ as the weighting function and obtain from (5) the NE formulation (short for $\hat{\mathbf{n}} \times \mathbf{E}$)

$$[P^{NE}]\{E_S\} + [Q^{NE}]\{\bar{H}_S\} = \{b^{NE}\} \quad (20)$$

where

$$P_{ij}^{NE} = - \int_S \hat{\mathbf{n}} \times \mathbf{g}_i \cdot \mathbf{K}(\mathbf{g}_j) dS \quad (21)$$

$$Q_{ij}^{NE} = \int_S \hat{\mathbf{n}} \times \mathbf{g}_i \cdot \mathbf{L}(\mathbf{g}_j) dS \quad (22)$$

$$b_i^{NE} = \int_S \hat{\mathbf{n}} \times \mathbf{g}_i \cdot \mathbf{E}^i dS \quad (23)$$

and from (6) the NH formulation (short for $\hat{\mathbf{n}} \times \mathbf{H}$)

$$[P^{NH}]\{E_S\} + [Q^{NH}]\{\bar{H}_S\} = \{b^{NH}\} \quad (24)$$

where

$$P_{ij}^{NH} = \int_S \hat{n} \times \mathbf{g}_i \cdot \mathbf{L}(\mathbf{g}_j) dS = Q_{ij}^{NE} \quad (25)$$

$$Q_{ij}^{NH} = \int_S \hat{n} \times \mathbf{g}_i \cdot \mathbf{K}(\mathbf{g}_j) dS = -P_{ij}^{NE} \quad (26)$$

$$b_i^{NH} = \int_S \hat{n} \times \mathbf{g}_i \cdot \bar{\mathbf{H}}^i dS. \quad (27)$$

Equations (20) and (24) can also be obtained by taking the cross product of \hat{n} with (5) and (6) and then use \mathbf{g}_i as the weighting function (That is the reason we used the abbreviations NE and NH for the two equations).

Theoretically, any of (12), (16), (20), and (24) can be used as (3). However, each of them suffers from the problem of interior resonance and fails to produce accurate solution at and near certain frequencies corresponding to the resonant frequencies of the cavity formed by covering S with a perfect electric or magnetic conductor and filling it with the exterior medium. To eliminate this problem, one has to combine an equation from EFIE to another equation from MFIE to obtain a combined equation (that is, CFIE) [21]. For example, one can combine (12) with (16) to obtain the TETH formulation or (12) with (24) to obtain the TENH formulation. One can also combine (20) with (16) to obtain the NETH formulation or (20) with (24) to obtain the NENH formulation which is the one employed in [12]. Among the four CFIE combinations, TENH and NETH are used most widely. However, it is not clear which combination would produce the most efficient and accurate solution.

Let us consider the issue of efficiency first. It is known that the FEM matrices in (4) are diagonally dominant. Hence, (4) would be better conditioned if $[Q]$ is diagonally dominant. An analysis of the matrix property shows that $[P^{NE}]$ and $[Q^{NH}]$ are most diagonally dominant, $[Q^{TE}]$ and $[P^{TH}]$ are diagonally dominant, and $[P^{TE}]$, $[Q^{TH}]$, $[Q^{NE}]$, and $[P^{NH}]$ are least diagonally dominant. These facts can be denoted as

$$\begin{aligned} [P^{NE}] = -[Q^{NH}] &\sim \begin{bmatrix} \ddots & & \\ & 2 & \\ & & \ddots \end{bmatrix}, & [Q^{TE}] = [P^{TH}] &\sim \begin{bmatrix} \ddots & & \\ & 1 & \\ & & \ddots \end{bmatrix}, \\ [P^{TE}] = -[Q^{TH}] &\sim \begin{bmatrix} \ddots & & \\ & 0 & \\ & & \ddots \end{bmatrix}, & [Q^{NE}] = [P^{NH}] &\sim \begin{bmatrix} \ddots & & \\ & 0 & \\ & & \ddots \end{bmatrix}. \end{aligned} \quad (28)$$

From these, we obtain the matrix structure for the TETH formulation as

$$[P|Q] \sim \left[\begin{array}{ccc|ccc} \ddots & & & \ddots & & \\ & 1 & & & 1 & \\ & & \ddots & & & \ddots \end{array} \right]. \quad (29)$$

For the TENH formulation, we have

$$[P|Q] \sim \left[\begin{array}{ccc|ccc} \ddots & & & \ddots & & \\ & 0 & & & 3 & \\ & & \ddots & & & \ddots \end{array} \right]. \quad (30)$$

For the NETH formulation, we have

$$[P|Q] \sim \left[\begin{array}{ccc|ccc} \ddots & & & \ddots & & \\ & 3 & & & 0 & \\ & & \ddots & & & \ddots \end{array} \right]. \quad (31)$$

Finally, for the NENH formulation, we have

$$[P|Q] \sim \left[\begin{array}{ccc|ccc} \ddots & & & \ddots & & \\ & 2 & & & 2 & \\ & & \ddots & & & \ddots \end{array} \right]. \quad (32)$$

Considering the properties of the FEM matrices in (4), heuristically, it is apparent that the TENH formulation would produce the best conditioned matrix for (4), the NETH formulation would yield the worst conditioned matrix, and both TETH and NENH formulations have condition numbers between those of TENH and NETH.

To verify the above predictions, we consider the problem of plane-wave scattering by a coated sphere. The coated sphere has a radius r_2 and its conducting core has a radius r_1 . The dielectric coating has a relative permittivity $\epsilon_r = 4$ and a free-space permeability and its thickness is chosen large enough so that there is an appreciable tangential electric field on the surface. Equation (4) is solved using the conjugate gradient (CG) method. Figure 1 displays the residual norm versus the number of iterations, from which we see clearly that TENH converges most quickly, NETH has the worst convergence, and the convergence of TETH and NENH lies between those of TENH and NETH. This observation agrees perfectly with our earlier prediction.

Next, we consider the issue of accuracy. Examining (12)–(27) carefully, we find that in the TE formulation, where \mathbf{g}_i is used as the weighting function, the first term in (8) has no contribution to (13) when $i = j$, or in other words, the first term in (8) is not tested. The same observation can be made for the TH formulation. However, in the NE formulation, where $\hat{\mathbf{n}} \times \mathbf{g}_i$ is used as the weighting function, the first term in (7) cannot be tested, and thus has no contribution to (22) when $i = j$. The same observation can be made for the NH formulation. Clearly, neither \mathbf{g}_i nor $\hat{\mathbf{n}} \times \mathbf{g}_i$ forms a complete set of weighting function for (5) or (6). Therefore, when \mathbf{g}_i or $\hat{\mathbf{n}} \times \mathbf{g}_i$ is used alone, the solution can become inaccurate. Since all the formulations described earlier (TETH, TENH, NETH, and NENH) are the result of using either \mathbf{g}_i or $\hat{\mathbf{n}} \times \mathbf{g}_i$ as the weighting function, their solutions can be inaccurate as well.

The above analysis on accuracy is also verified by the numerical analysis of the problem described earlier. Figure 2 shows the bistatic radar cross section (RCS) of the coated sphere. It is obvious that all the four formulations have a significant error in their solutions. Our further numerical experiments show that such errors cannot be reduced significantly by using finer discretization. It is interesting to note that both TETH and NENH have a similar error and both TENH and NETH also have a similar error. However, the error in TETH and NENH is smaller than that in TENH and NETH. We note that this problem of inaccuracy occurs only when there exist simultaneously nontrivial tangential electric and magnetic fields on the surface S ; therefore, it disappears when one deals with a bare conducting body or a conducting body with a very thin coating where the tangential electric field is very small. This is why the problem was not observed in [12]. We also note that this problem was not observed in [10], [11], and [14] because none of them employed the RWG functions as both the expansion and weighting functions.

To alleviate the inaccuracy discussed above, it is clear that a more complete set of weighting functions has to be used. A natural choice is a combination of \mathbf{g}_i and $\hat{\mathbf{n}} \times \mathbf{g}_i$. When this is applied to (5), we obtain a matrix equation, which is equivalent to the sum of (12) and (20) and is referred to as the TENE formulation. When this is applied to (6), we obtain a matrix equation, which is equivalent to the sum of (16) and (24) and is referred to as the THNH formulation. However, since TENE comes from EFIE and THNH comes from MFIE, both would suffer from the problem of interior resonance. One remedy is to combine TENE and THNH. A more efficient alternative is to combine TENE with either the NH or TH formulation. A simple analysis of matrix condition shows that among NH and

TH, NH is a better choice for the combination with TENE. Figure 3 shows the result of TENENH, from which we see that TENENH has a significantly better accuracy than those in Fig. 2. The remaining error in TENENH can be reduced by using a finer discretization. The corresponding convergence curves are given in Fig. 4.

The results presented above are obtained at the frequency that does not coincide with the frequency of interior resonance. To ensure the validity of our analysis, we consider the same coated sphere at a frequency of interior resonance. Figure 5 displays the residual norm versus the number of iterations, from which we observe a similar convergence behavior that agrees with our prediction. However, compared to Fig. 1, the number of iterations for TETH and NENH in this case has increased significantly whereas that for TENH and NETH remains the same. To investigate this problem further, we recorded the number of iterations at the frequencies near the frequency of interior resonance and the result is given in Fig. 6. To our surprise, both TETH and NENH have a sharp peak at the frequency of interior resonance. This implies that both TETH and NENH yield an ill-conditioned matrix and still suffer from the problem of interior resonance, although they are derived from the CFIE formulation. However, the bandwidth of the ill-conditioned peaks is extremely narrow (less than 1%), compared to those resulting from either the EFIE or the MFIE (about 10%), and this is probably the reason that this problem was not detected before. The results for the RCS are given in Fig. 7. As expected, both TETH and NENH yield a result drastically different from the exact solution whereas both TENH and NETH produce a stable result with an error similar to that in Fig. 2. The result obtained using TENENH is presented in Fig. 8, from which a good agreement is observed. The number of iterations at the frequencies near the frequency of interior resonance is also given in Fig. 6, showing a very stable behavior.

Next, we present several other examples to demonstrate the accuracy and capability of the proposed formulation for other geometries. Figure 9 shows the bistatic RCS of a finite dielectric cylinder and Fig. 10 displays the result for a dielectric cube. All the results are compared with those obtained from MoM and excellent agreement is observed in each case. We note that the MoM solutions shown in Figs. 9 and 10 are obtained from the PMCHW formulation [22], which is a combined-source integral equation (CSIE). The PMCHW formulation is known to produce accurate solution [23], [24]; however, it can be applied to only homogeneous objects.

III. CONCLUSION

In this paper, we studied in detail a variety of formulations for the hybrid FE-BI method for calculating 3D electromagnetic scattering by inhomogeneous objects. We showed that the efficiency and accuracy of the FE-BI method depend highly on the formulation and discretization of BIE used. We considered four formulations (TETH, TENH, NETH, and NENH) obtained from the discretization of the CFIE, and we found from analysis and verified numerically that

- TENH produces the best conditioned FE-BI matrix equation and NETH produces the worst conditioned matrix equation. Therefore, when an iterative solver such as the CG algorithm is employed to solve the matrix equation, TENH is the most efficient formulation.
- None of the four formulations produces accurate FE-BI solution because neither the RWG vector basis functions (\mathbf{g}_i) nor its cross product with the unit normal ($\hat{\mathbf{n}} \times \mathbf{g}_i$) form a complete set of weighting functions for EFIE or MFIE on a general surface where nontrivial equivalent electric and magnetic currents exist simultaneously.
- Both TETH and NENH suffer from the problem of interior resonance although the bandwidth of the bad solution is extremely narrow, compared to those resulting from EFIE and MFIE. However, TENH and NETH are immune to the problem of interior resonance although their results are inaccurate.

Based on the analysis, we proposed a formulation (TENENH) that has a good efficiency and a good accuracy and is completely immune to the corruption of interior resonance. The TENE part of this formulation is equivalent to testing the pertinent EFIE twice, or equivalent to testing an equation with N unknowns $2N$ times, yielding $2N$ equations. This is an overdetermined system whose solution can be sought by the least square approach. However, we find that by adding the equations, which is equivalent to testing EFIE by $\mathbf{g}_i + \hat{\mathbf{n}} \times \mathbf{g}_i$, good result is also obtained. Our next step is then to apply MLFMA to the proposed FE-BI method to enhance its capability to deal with larger objects.

Acknowledgment

This work was supported by the Office of Naval Research under grant N00014-95-1-0848, by a grant from the Air Force Office of Scientific Research via the MURI

Program under contract number F49620-96-1-0025, and by the National Science Foundation under grant NSF ECE 94-57735.

References

- [1] S. P. Marin, "Computing scattering amplitudes for arbitrary cylinders under incident plane waves," *IEEE Trans. Antennas Propagat.*, vol. AP-30, pp. 1045-1049, Nov. 1982.
- [2] J. M. Jin and V. V. Liepa, "Application of hybrid finite element method to electromagnetic scattering from coated cylinders," *IEEE Trans. Antennas Propagat.*, vol. AP-36, pp. 50-54, Jan. 1988.
- [3] J. M. Jin and V. V. Liepa, "A note on hybrid finite element method for solving scattering problems," *IEEE Trans. Antennas Propagat.*, vol. AP-36, pp. 1486-1490, Oct. 1988.
- [4] Z. Gong and A. W. Glisson, "A hybrid equation approach for the solution of electromagnetic scattering problems involving two-dimensional inhomogeneous dielectric cylinders," *IEEE Trans. Antennas Propagat.*, vol. AP-38, pp. 60-68, Jan. 1990.
- [5] K. L. Wu, G. Y. Delisle, D. G. Fang, and M. Lecours, "Coupled finite element and boundary element methods in electromagnetic scattering," in *Finite Element and Finite Difference Methods in Electromagnetic Scattering*. New York: Elsevier, 1990.
- [6] X. Yuan, D. R. Lynch, and J. W. Strohbehn, "Coupling of finite element and moment methods for electromagnetic scattering from inhomogeneous objects," *IEEE Trans. Antennas Propagat.*, vol. AP-38, pp. 386-393, Mar. 1990.
- [7] K. D. Paulsen, D. R. Lynch, and J. W. Strohbehn, "Three-dimensional finite, boundary, and hybrid element solutions of the Maxwell equations for lossy dielectric media," *IEEE Trans. Microwave Theory Tech.*, vol. MTT-36, pp. 682-693, Apr. 1988.
- [8] X. Yuan, "Three-dimensional electromagnetic scattering from inhomogeneous objects by the hybrid moment and finite element method," *IEEE Trans. Microwave Theory Tech.*, vol. MTT-38, pp. 1053-1058, Aug. 1990.

- [9] J. M. Jin and J. L. Volakis, "A hybrid finite element method for scattering and radiation by microstrip patch antennas and arrays residing in a cavity," *IEEE Trans. Antennas Propagat.*, vol. AP-39, pp. 1598-1604, Nov. 1991.
- [10] J.-J. Angelini, C. Soize, and P. Soudais, "Hybrid numerical method for harmonic 3-D Maxwell equations: Scattering by a mixed conducting and inhomogeneous anisotropic dielectric medium," *IEEE Trans. Antennas Propagat.*, vol. AP-41, pp. 66-76, May 1993.
- [11] W. E. Boyes and A. A. Seidl, "A hybrid finite element method for 3-D scattering using nodal and edge elements," *IEEE Trans. Antennas Propagat.*, vol. AP-42, pp. 1436-1442, Oct. 1994.
- [12] G. E. Antilla and N. G. Alexopoulos, "Scattering from complex three-dimensional geometries by a curvilinear hybrid finite-element-integral equation approach," *J. Opt. Soc. Am. A*, vol. 11, no. 4, pp. 1445-1457, Apr. 1994.
- [13] T. Eibert and V. Hansen, "Calculation of unbounded field problems in free space by a 3D FEM/BEM-hybrid approach," *J. Electromag. Waves Appl.*, vol. 10, no. 1, pp. 61-77, 1996.
- [14] T. Cwik, C. Zuffada, and V. Jamnejad, "Modeling three-dimensional scatterers using a coupled finite element-integral equation formulation," *IEEE Trans. Antennas Propagat.*, vol. AP-44, pp. 453-459, Apr. 1996.
- [15] J. M. Jin, *The Finite Element Method in Electromagnetics*. New York: Wiley, 1993.
- [16] N. Lu and J. M. Jin, "Application of fast multipole method to finite-element boundary-integral solution of scattering problems," *IEEE Trans. Antennas Propagat.*, vol. AP-44, pp. 781-786, June 1996.
- [17] R. Coifman, V. Rokhlin, and S. Wandzura, "The fast multipole method for the wave equation: A pedestrian prescription," *IEEE Trans. Antennas Propagat. Mag.*, vol. 35, pp. 7-12, June 1993.
- [18] J. M. Song and W. C. Chew, "Multilevel fast-multipole algorithm for solving combined field integral equations of electromagnetic scattering," *Microwave Opt. Tech. Lett.*, vol. 10, no. 1, pp. 14-19, Sept. 1995.

- [19] A. J. Poggio and E. K. Miller, "Integral equation solutions of three dimensional scattering problems," in *Computer Techniques for Electromagnetics*. Oxford, UK: Permagon, 1973, ch-4.
- [20] S. M. Rao, D. R. Wilton, and A. W. Glisson, "Electromagnetic scattering by surfaces of arbitrary shape," *IEEE Trans. Antennas Propagat.*, vol. AP-30, pp. 409-418, May 1982.
- [21] S. M. Rao and D. R. Wilton, "*E*-field, *H*-field, and combined field solution for arbitrarily shaped three-dimensional dielectric bodies," *Electromagnetics*, vol. 10, no. 4, pp. 407-421, 1990.
- [22] J. R. Mautz and R. F. Harrington, "Electromagnetic scattering from a homogeneous material body of revolution," *AEU*, vol. 33, pp. 71-80, 1979.
- [23] L. N. Medgyesi-Mitschang, J. M. Putnam, and M. B. Gedera, "Generalized method of moments for three-dimensional penetrable scatterers," *J. Opt. Soc. Am. A*, vol. 11, no. 4, pp. 1383-1398, Apr. 1994.
- [24] S. M. Rao, C. C. Cha, R. L. Cravey, and D. Wilkes, "Electromagnetic scattering from arbitrary shaped conducting bodies coated with lossy materials of arbitrary thickness," *IEEE Trans. Antennas Propagat.*, vol. AP-39, pp. 627-631, May 1991.

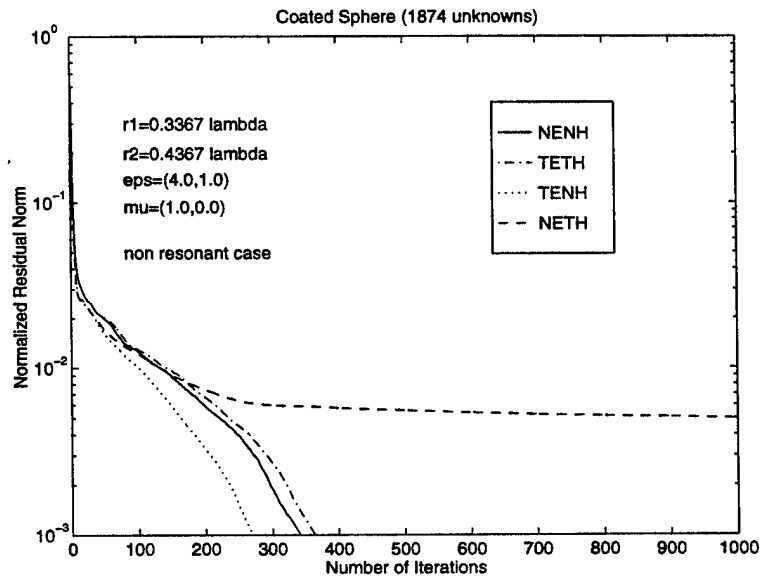


Figure 1: The normalized residual norm versus the number of iterations in the CG solution of scattering by a coated sphere.

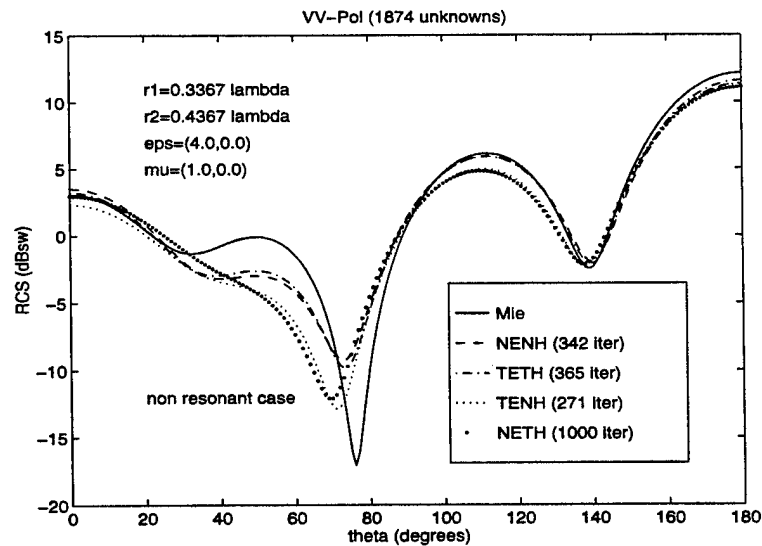


Figure 2: The bistatic RCS of a coated sphere. Neither of the four formulations produces accurate results.

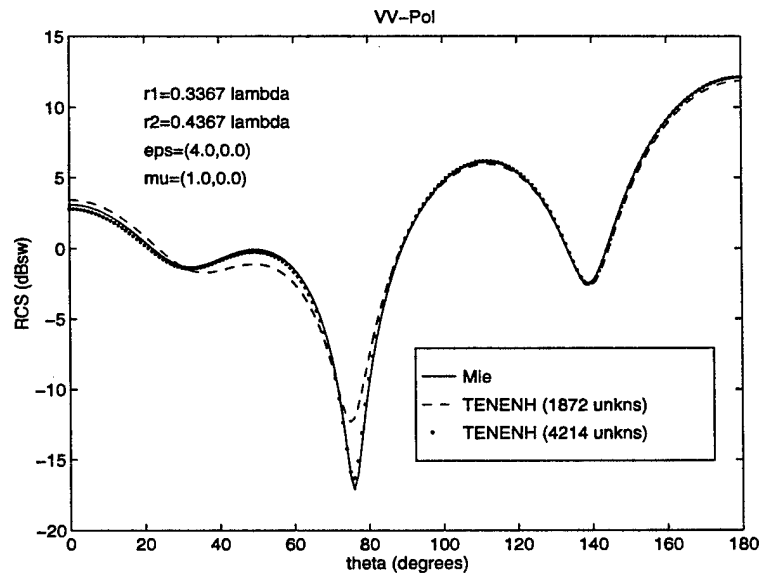


Figure 3: The bistatic RCS of a coated sphere. Good results are obtained using the TENENH formulation.

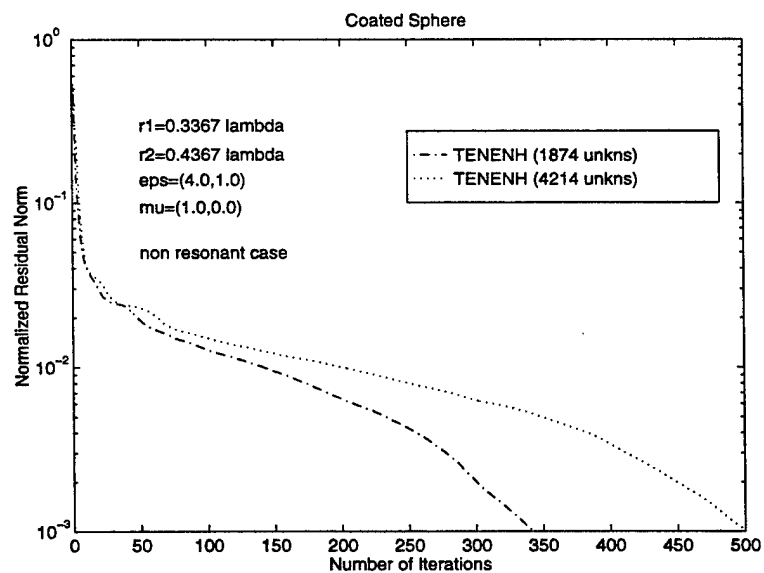


Figure 4: The normalized residual norm versus the number of iterations for the TENENH formulation.

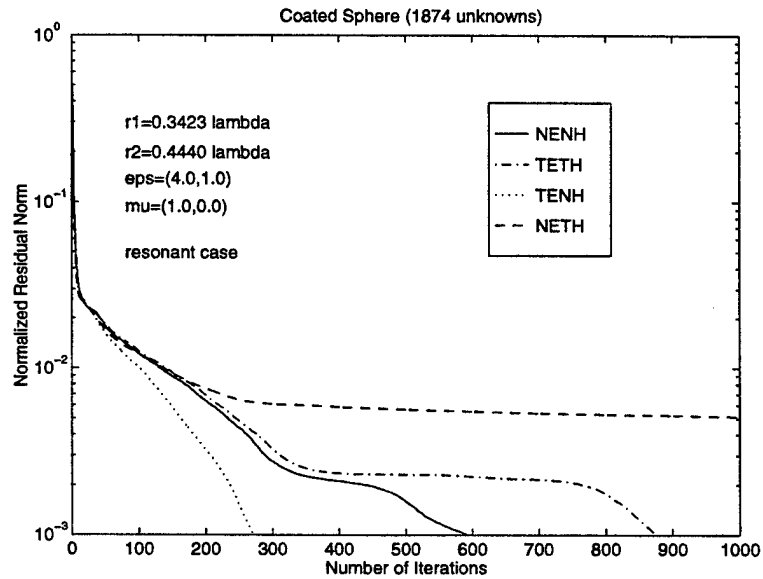


Figure 5: The normalized residual norm versus the number of iterations in the CG solution of scattering by a coated sphere at the frequency of interior resonance.

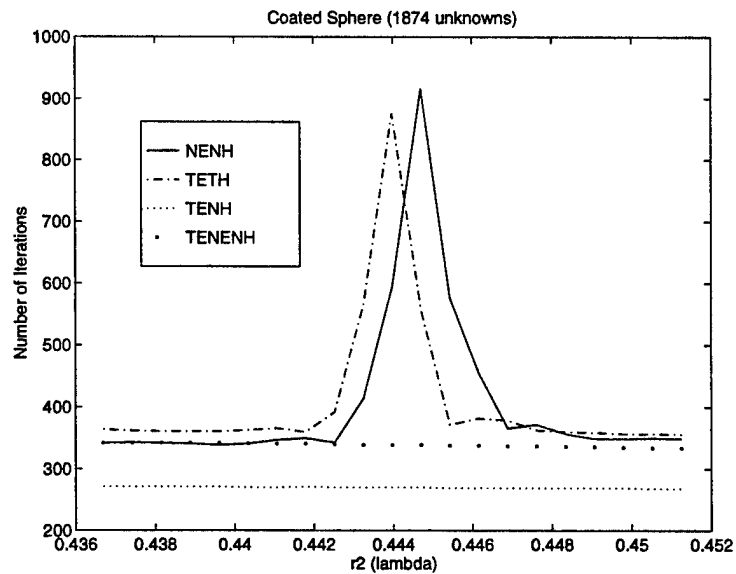


Figure 6: The number of iterations versus frequency (equivalently, the size of the scatterer in terms of wavelength). Both NENH and TETH exhibit singular behavior near the frequency of interior resonance whereas both TENH and TENENH display a stable behavior.

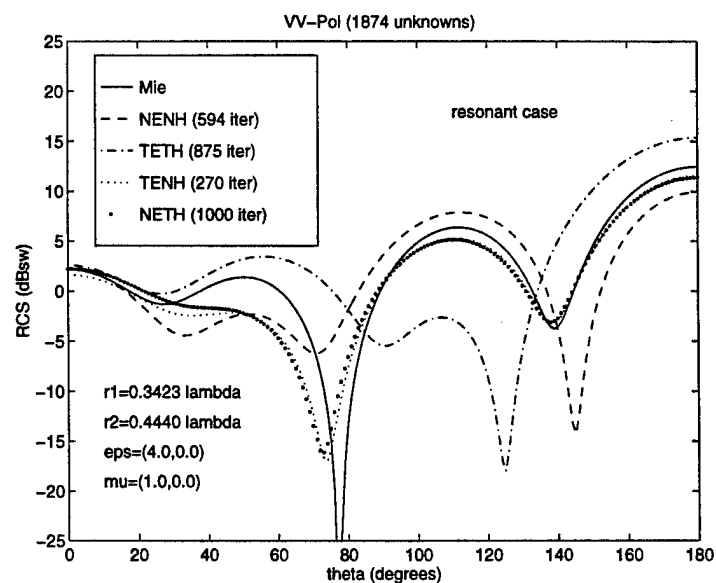


Figure 7: The bistatic RCS of a coated sphere. Neither of the four formulations produces accurate results. In particular, both NENH and TETH yield erroneous results.

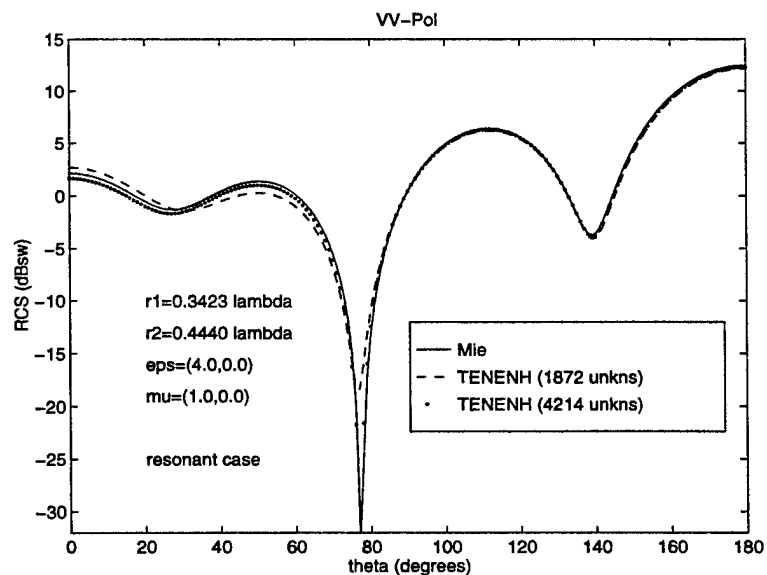
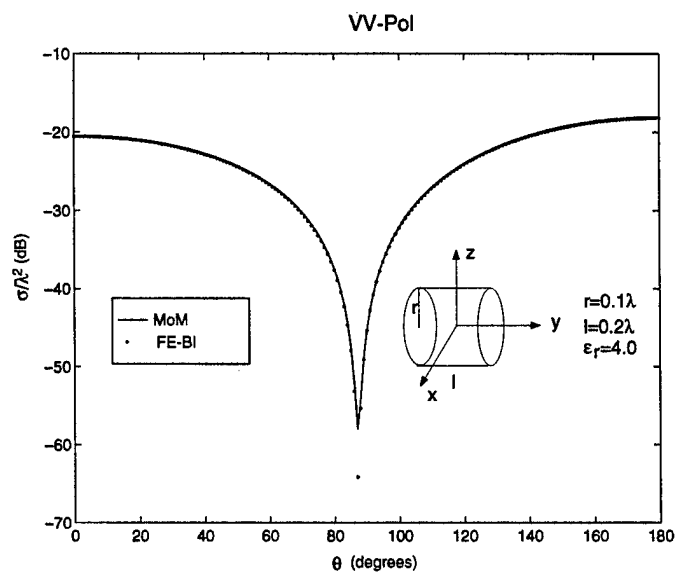
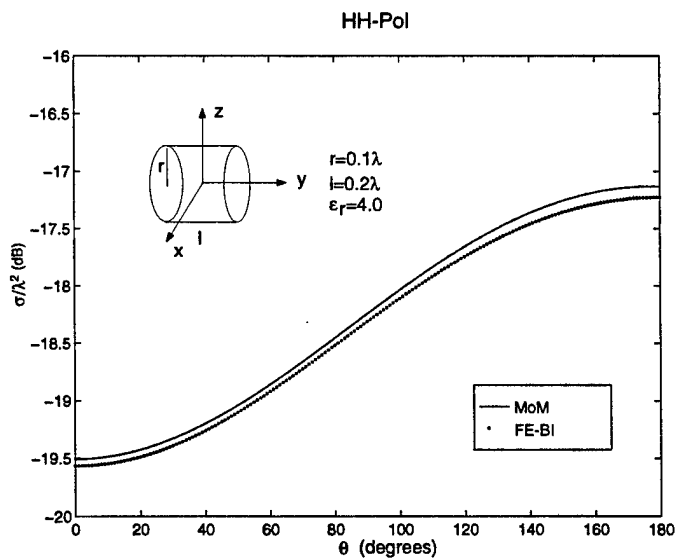


Figure 8: The bistatic RCS of a coated sphere at the frequency of interior resonance. Again, good results are obtained using the TENENH formulation.

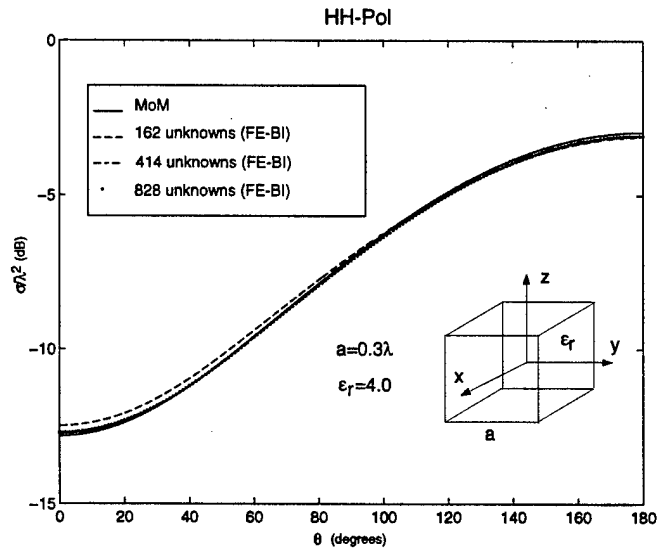
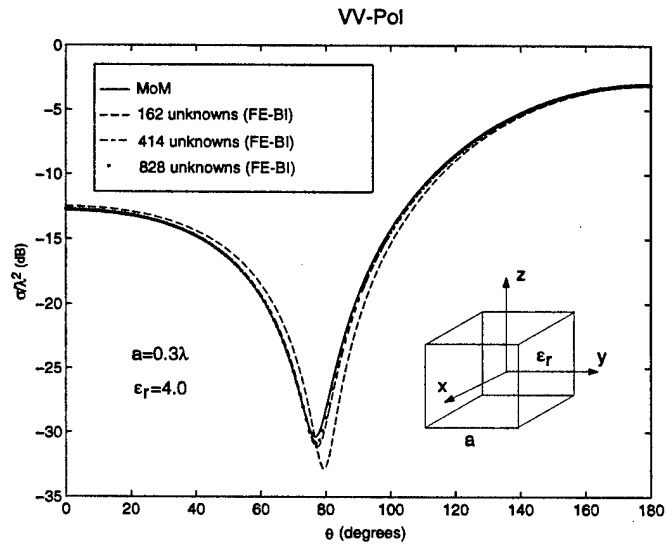


(a)



(b)

Figure 9: The bistatic RCS of a finite dielectric cylinder in the x - z plane for a plane wave incident along the z -axis. (a) VV-polarization. (b) HH-polarization.



(b)

Figure 10: The bistatic RCS of a dielectric cube in the x - z plane for a plane wave incident along the z -axis. (a) VV-polarization. (b) HH-polarization.

APPENDIX 5

Complementary Perfectly Matched Layers to Reduce Reflection Errors

Jian-Ming Jin, Xin-Qing Sheng, and Weng Cho Chew *

May 8, 1997

KEY TERMS

Perfectly matched layer, finite-element method, absorbing boundary condition

Abstract

A new approach is proposed to reduce the reflection error of a perfectly matched layer (PML) in the frequency-domain finite-element solution of electromagnetics problems. The approach is based on the complementary nature of a PML backed by a perfect electric conductor (PEC) and one backed by a perfect magnetic conductor (PMC). By averaging the solutions obtained by PEC- and PMC-backed PML, the error is reduced by $20\log|R|$ dB where R is the reflection coefficient of the PEC- or PMC-backed PML. Numerical results are presented to demonstrate the accuracy of the complementary PMLs.

1 Introduction

The perfectly matched layer (PML) has recently been introduced by Berenger [1] as a material absorbing boundary condition (ABC) for electromagnetics problems. An infinitely thick PML has no reflection for all incident angles and all frequencies at its interface with another medium. However, when the PML is used to truncate the finite difference or finite element solution domain, it must be terminated or backed by a perfectly conducting or impedance surface. As a result, the PML does not possess zero reflection for all incident angles. Instead, the reflection coefficient increases as the incident angle and reaches 1 at grazing. To reduce the error from this artificial reflection, one must either place the PML at some distance away from the object or increase the PML thickness. Both would result in a large solution domain and reduce the efficiency of the numerical solution. Recently, we have studied the optimization of the PML [2] and proposed a combination of the PML with ABC to reduce the artificial reflection [3].

*The authors are with the Center for Computational Electromagnetics, Department of Electrical and Computer Engineering, University of Illinois at Urbana-Champaign, Urbana, Illinois 61801-2991 USA.

In this paper, we propose a new approach to reduce the numerical error associated with the artificial reflection of the PML. This approach employs a pair of PMLs that have exactly the same material composition or parameters, but one is backed by a perfect electric conductor (PEC) and the other by a perfect magnetic conductor (PMC). As a result, the PEC-backed PML has a reflection coefficient negative to that of the PMC-backed PML, or in other words, the PEC- and PMC-backed PMLs are complementary to each other. Assuming that the PEC-backed PML has a reflection coefficient R , the numerical solution obtained with this PML has an error proportional to R . When the same problem is solved using the PMC-backed PML, the error is proportional to $-R$. Averaging the two solutions eliminates the error proportional to R and the remaining error is proportional to R^2 , which is due to the double reflections of waves. The use of the complementary PMLs is demonstrated by both two- and three-dimensional waveguide discontinuity problems. We note that a similar idea was employed before for the finite-difference time-domain (FDTD) solution of partial differential equations [4-6].

2 Analysis

To demonstrate the application of complementary PMLs, consider a parallel-plate waveguide discontinuity problem, sketched in Fig. 1(a). To solve this problem using the finite-element method (FEM) in conjunction with the PML, we terminate both ends with the PML and place a magnetic current sheet to excite the desired incident field, as illustrated in Fig. 1(b). Using the coordinate-stretching approach proposed in [7] and extended in [3], we can show that for a TM mode incidence, the magnetic field satisfies the differential equation

$$\frac{1}{\sqrt{e_x}} \frac{\partial}{\partial x} \left(\frac{1}{e_x \epsilon_r} \frac{\partial H_y}{\partial x} \frac{1}{\sqrt{e_x}} \right) + \frac{1}{\sqrt{e_z}} \frac{\partial}{\partial z} \left(\frac{1}{e_z \epsilon_r} \frac{\partial H_y}{\partial z} \frac{1}{\sqrt{e_z}} \right) + k_0^2 \mu_r H_y = j k_0 Y_0 M_y \quad (1)$$

where e_x and e_z are coordinate stretching variables. For a PML normal to the x axis, $e_x = s_x(x)$ and $e_z = 1$, and for a PML normal to the z axis, $e_z = s_z(z)$ and $e_x = 1$, where s_x and s_z are parameters for the PML. In this case, there is no PML normal to the x axis and for the PML normal to the z axis, we choose

$$s_z(z) = 1 - j \delta_{max} (l/L)^2 \quad (2)$$

where δ_{max} denotes the maximum loss tangent, l is the distance from the air/PML interface, and L is the thickness of the PML.

To illustrate the accuracy of the complementary PMLs, we first considered the parallel-plate waveguide without the discontinuity and calculated the field distribution for the TEM incidence at 15 GHz. For the calculation, $L = 5$ mm and $\delta_{max} = 30/f$ where f denotes the frequency in GHz. For such a PML, the

reflection coefficient is 6.3% (−24 dB). The FEM discretization is 1 element per 1 mm. The relative error in the solution obtained with the PEC-backed PML (PEC-PML) and complementary PMLs (COM-PML) is given in Fig. 2. The error in the PMC-PML solution is similar to that in the PEC-PML solution. As can be seen, the maximum error in the PEC-PML solution is about 6.6% and that in the COM-PML solution is about 0.33% (−50 dB), which agrees with our earlier prediction, that is, about the square of 6.6%.

The reflection coefficient due to the discontinuity for the TEM incidence is given in Fig. 3, where we have plotted the results obtained with PEC-PML, PMC-PML, and COM-PML, compared to the solution obtained using the exact ABC [8]. Excellent agreement is observed between the COM-PML and exact ABC solutions, whereas those obtained with PEC-PML and PMC-PML deviate from the exact solution significantly. We note that with the COM-PML, we can place the PML as close as 3 mm away from the nearest edge of the discontinuity (resulting in 226 unknowns) with an accuracy comparable to that obtained with a 20-layer PEC-backed PML placed 10 mm away from the discontinuity (resulting in 710 unknowns) [2]. Therefore, although the COM-PML requires solving the problem twice, it is still more efficient than the PEC-PML because of the reduced number of unknowns.

Next, we consider a three-dimensional waveguide discontinuity problem, illustrated in Fig. 4. To numerically solve this problem, we again terminate both ends of the waveguide with the PML and introduce an electric current to excite the desired incident field. The differential equation for the electric field is given by [3]

$$\nabla_e \times \left[\frac{1}{\mu_r} (\nabla_e \times \mathbf{E}) \right] - k_0^2 \epsilon_r \mathbf{E} = -jk_0 Z_0 \mathbf{J} \quad (3)$$

where

$$\nabla_e = \hat{x} \frac{1}{\sqrt{e_x}} \frac{\partial}{\partial x} \frac{1}{\sqrt{e_x}} + \hat{y} \frac{1}{\sqrt{e_y}} \frac{\partial}{\partial y} \frac{1}{\sqrt{e_y}} + \hat{z} \frac{1}{\sqrt{e_z}} \frac{\partial}{\partial z} \frac{1}{\sqrt{e_z}} \quad (4)$$

in which e_x , e_y , and e_z are defined in the same way as above.

Again, to illustrate the accuracy of the COM-PML, we calculated the field in the empty waveguide due to the TE_{10} incidence at 10 GHz. For the calculation, $L = 6$ mm and $\delta_{max} = 30/f$, and the FEM discretization is 1 element per 2 mm. The relative error is given in Fig. 5, where the maximum error in the PEC-PML solution is about 15%, in contrast to 1.4% in the COM-PML solution.

The reflection coefficient due to the discontinuity for the TE_{10} incidence is shown in Fig. 6. For the calculation, the PML is placed only 2 elements away from the nearest edge of the dielectric obstacle. The results are compared to the data obtained using the method of orthogonal expansions [9]. Excellent agreement is observed between the COM-PML and reference data.

3 Conclusion

A new and simple approach was proposed to significantly reduce the PML reflection error in the finite element solution of electromagnetics problems. The approach was validated by numerical examples for both two- and three-dimensional waveguide discontinuity problems. It was shown that the reflection error can be reduced from $20\log|R|$ dB to $40\log|R|$ dB.

Acknowledgments

This work was supported by the National Science Foundation under grants NSF ECE 94-57735 and 93-02145, and the Office of Naval Research under grants N00014-95-1-0848 and N00014-95-1-0872.

References

- [1] J.-P. Berenger, "A perfectly matched layer for the absorption of electromagnetic waves," *J. Computational Phys.*, vol. 114, pp. 185-200, 1994.
- [2] W. C. Chew and J. M. Jin, "Perfectly matched layers in the discretized space: An analysis and optimization," *Electromagnetics*, vol. 16, pp. 325-340, July 1996.
- [3] J. M. Jin and W. C. Chew, "Combining PML and ABC for finite element analysis of scattering problems," *Microwave Opt. Tech. Lett.*, vol. 12, pp. 192-197, July 1996.
- [4] K. K. Mei and J. Fang, "Superabsorption - A method to improve absorbing boundary conditions," *IEEE Trans. Antennas Propagat.*, vol. AP-40, pp. 1001-1010, Sept. 1992.
- [5] O. M. Ramahi, "Complementary operators: A method to annihilate artificial reflections arising from the truncation of the computational domain in the solution of partial differential equations," *IEEE Trans. Antennas Propagat.*, vol. AP-43, pp. 697-704, July 1995.
- [6] W. L. Ko and R. Mittra, "Extremely low frequency modeling in lossy media using FDTD with application in seafloor characterization," *Electromagnetics*, vol. 15, pp. 587-602, Nov.-Dec. 1995.
- [7] W. C. Chew and W. H. Weedon, "A 3D perfectly matched medium from modified Maxwell's equations with stretched coordinates," *Microwave Opt. Tech. Lett.*, vol. 7, pp. 599-604, 1994.
- [8] J. M. Jin, *The Finite Element Method in Electromagnetics*. New York: Wiley, 1993, pp. 105-107.
- [9] H. Katzier, "Streuverhalten elektromagnetischer Wellen bei sprunghaften Ubergangen geschirmter dielektrischer Leitungen," *Arch. Elek. Ubertragung.*, vol. 38, pp. 290-296, 1984.

FIGURE CAPTIONS

Figure 1. (a) Parallel-plate waveguide discontinuity problem. (b) PML truncation.

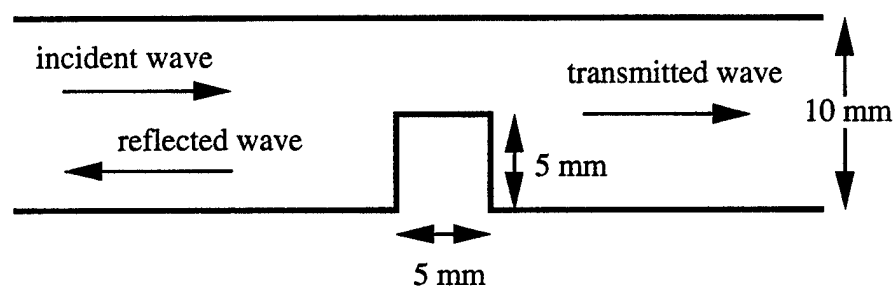
Figure 2. Relative error in the field of an empty parallel-plate waveguide when the waveguide is terminated by (a) PEC-PML and (b) COM-PML.

Figure 3. Reflection coefficient for the dominant-mode incidence.

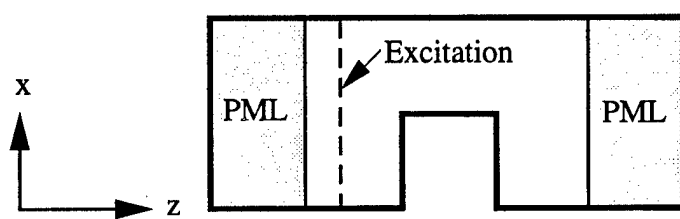
Figure 4. Rectangular waveguide loaded with a dielectric obstacle having $\epsilon_r = 6$. For numerical simulation, the waveguide is terminated with a PML.

Figure 5. Relative error in the field of an empty rectangular waveguide when the waveguide is terminated by (a) PEC-PML and (b) COM-PML.

Figure 6. Reflection coefficient for different dielectric lengths. (a) $d = 1.2$ cm. (b) $d = 0.8$ cm.

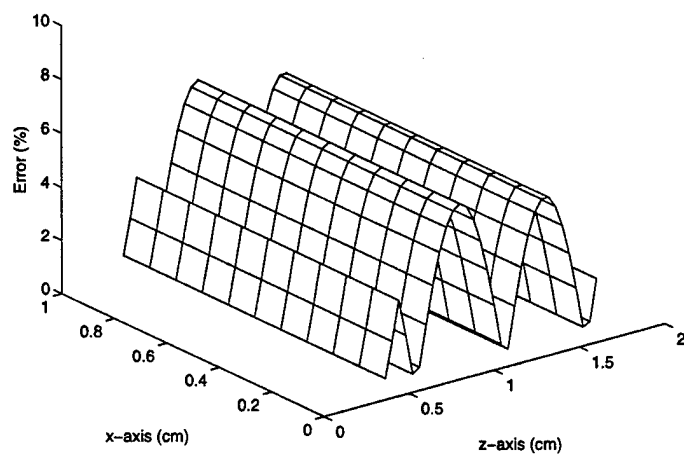


(a)

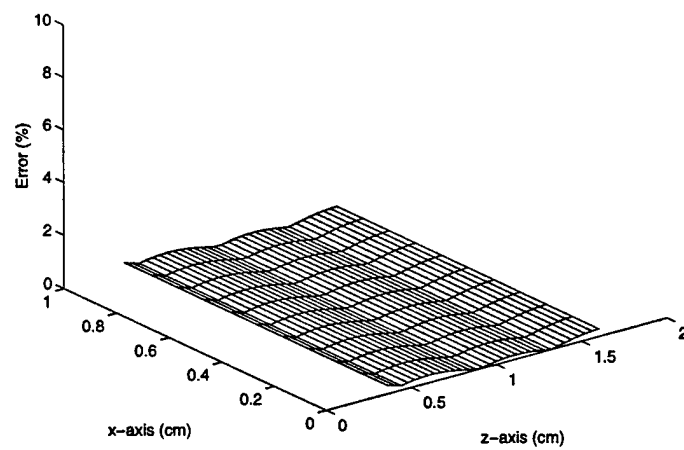


(b)

Fig. 1



(a)



(b)

Figure 2

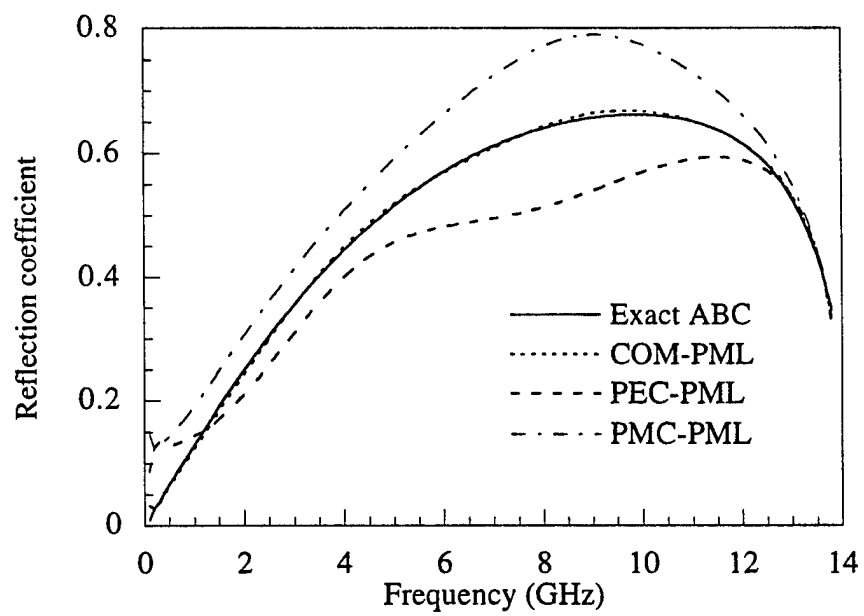


Fig. 3

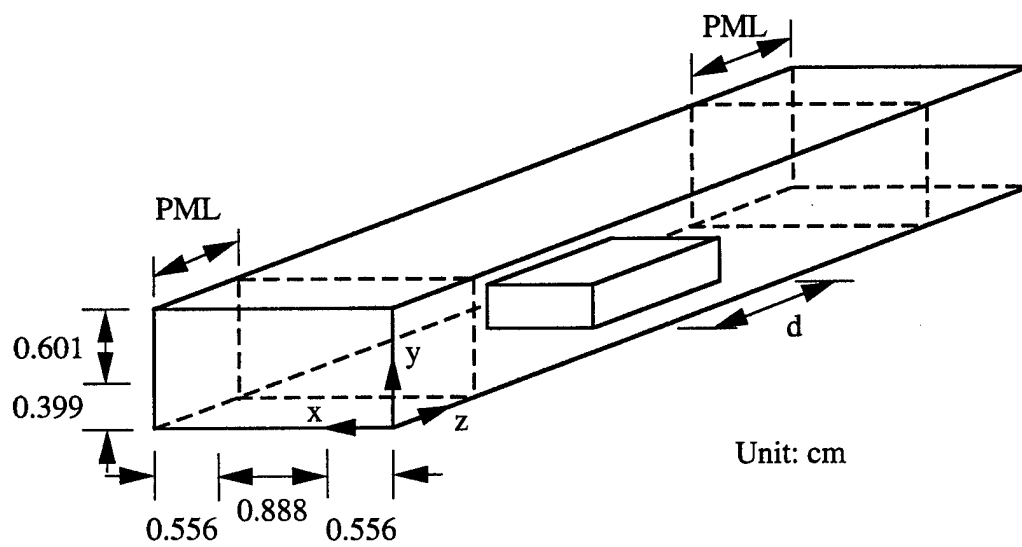
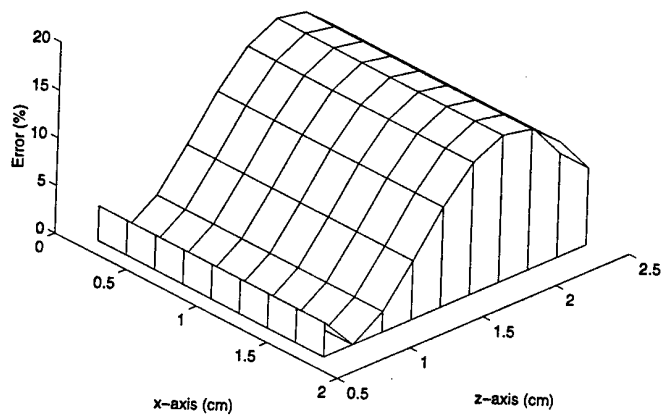
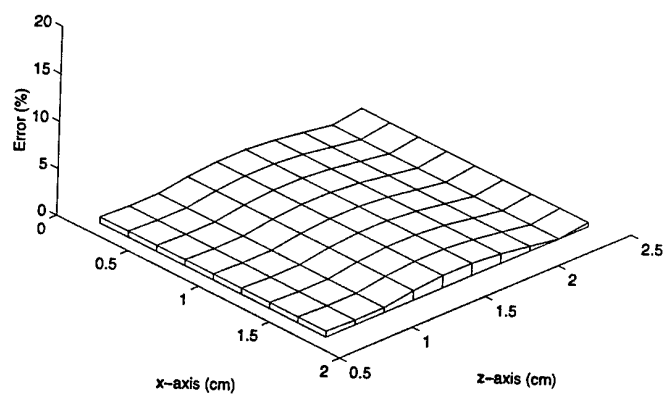


Fig. 4

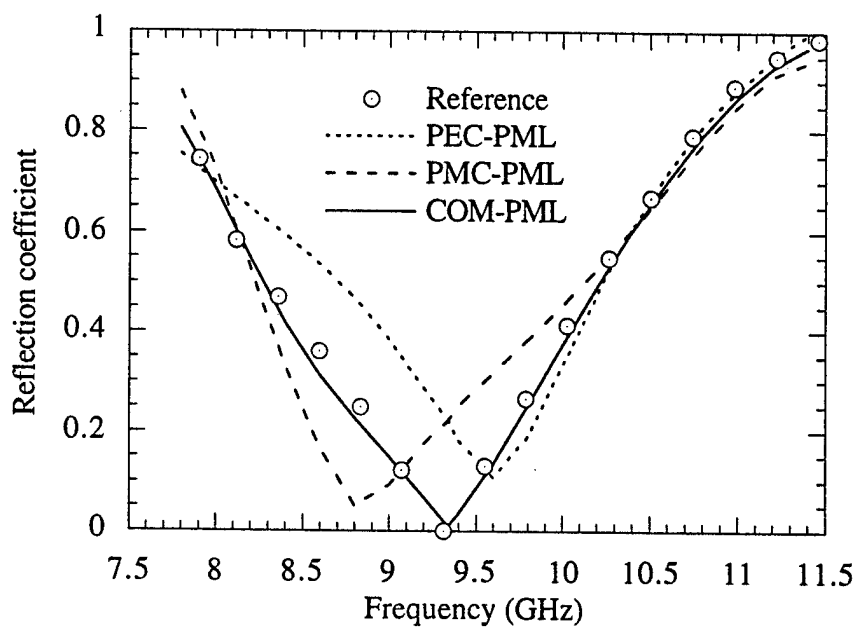


(a)

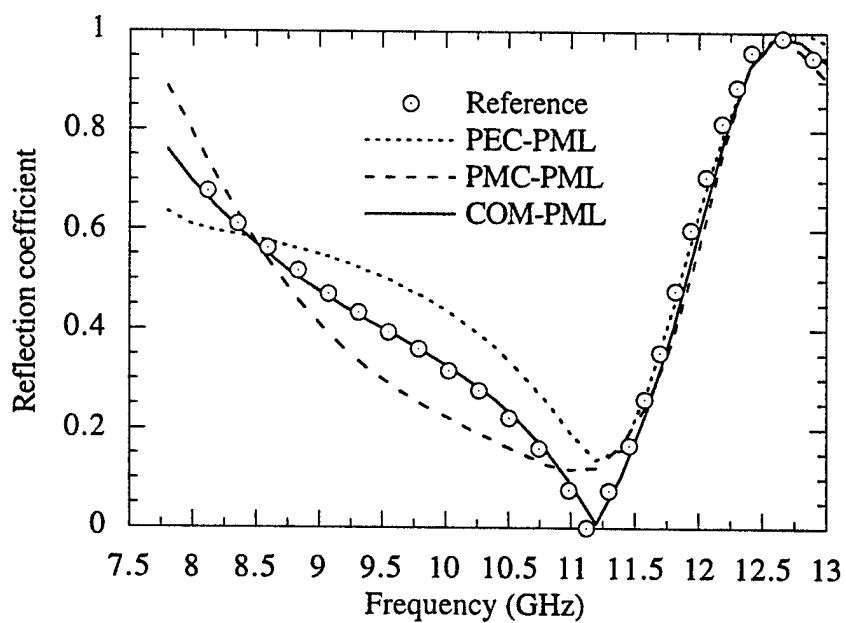


(b)

Figure 5



(a)



(b)

Figure 6. Reflection coefficient for different dielectric lengths. (a) $d = 1.2$ cm. (b) $d = 0.8$ cm.

Simple and Efficient Computation of Electromagnetic Fields in Arbitrarily-Shaped, Inhomogeneous Dielectric Bodies Using Transpose-Free QMR and FFT

C. F. Wang and J. M. Jin

Center for Computational Electromagnetics
Department of Electrical and Computer Engineering
University of Illinois at Urbana-Champaign
Urbana, Illinois 61801-2991

Abstract

A simple and efficient numerical method is presented for computing electromagnetic fields in three-dimensional inhomogeneous dielectric bodies. The method employs a two-stage discretization to convert an integro-differential equation into an implicit system of linear algebraic equations. This discrete system is then solved using a transpose-free quasi-minimal residual (TFQMR) algorithm, which avoids the complicated calculation of the multiplication between the transpose of the system matrix and a vector. The simple multiplication between the system matrix and a vector required in the TFQMR algorithm is calculated efficiently using only six fast Fourier transforms (FFT). Numerical results for strongly inhomogeneous and lossy spheres show that the method has a stable convergence behavior and excellent numerical performance.

I. Introduction

Efficient computation of electromagnetic fields in arbitrarily-shaped, inhomogeneous dielectric bodies in a three-dimensional (3D) space plays an important role in many applications such as nondestructive testing, microwave imaging, scattering control, target identification, electromagnetic hyperthermia, and magnetic resonance imaging. The well-known method of moments (MoM) [1]–[3] is one of the popular methods for this computation. In this method, an integro-differential equation is first formulated in terms of volumetric equivalent current that accounts for the effect of the permittivity and conductivity of an inhomogeneous body. This integro-differential equation is then discretized using mostly Galerkin's procedure. The discretization results in a matrix equation with a very large number of unknowns, whose solution using a direct solver, such as Gaussian elimination and LU decomposition method, is basically impractical, because a direct solver has a memory requirement of $O(N^2)$ and computational complexity of $O(N^3)$, where N denotes the

number of unknowns. This difficulty can be circumvented by solving the matrix equation using an iterative solver and in each iteration the required matrix-vector multiplication is evaluated using the fast Fourier transform (FFT) [4]. In the past, the conjugate gradient (CG) and the biconjugate gradient (BCG) methods have been employed as such an iterative solver, and the resultant methods are often referred to as the CG-FFT and BCG-FFT methods [5]–[7]. The use of the so-called CG-FFT or BCG-FFT method reduces the memory requirement to $O(N)$ and computational complexity to $O(N_{iter}N \log N)$, where N_{iter} denotes the number of CG or BCG iterations.

There is a large body of literature on the CG-FFT and BCG-FFT methods for a variety of electromagnetics problems and it is not our intention to review it here. Instead, we shall focus on those for 3D volumetric material problems. The first application of the CG-FFT method to such problems can be found in the analysis of the absorption of electromagnetic power by human bodies [5]. However, the use of pulse basis functions yielded slow convergence and poor results when dealing with materials with high dielectric contrast. Better formulations were later proposed [8]–[12], and most used mixed-order (linear in one direction and constant in the other two directions) basis functions. Among these, the methods proposed by Zwamborn and van den Berg [10] and Gan and Chew [11] are the most accurate for materials with high dielectric contrast. In both methods, one is required to calculate within each iteration the multiplication between the transpose of the system matrix and a vector, in addition to that between the system matrix and a vector, resulting in at least 12 FFTs per iteration. Furthermore, the multiplication between the transpose of the system matrix and a vector is found to be more complicated than that between the system matrix and a vector.

In this paper, we present an alternative and more efficient method for computing electromagnetic fields in arbitrarily-shaped, inhomogeneous dielectric bodies. In this method, a transpose-free quasi-minimal residual (TFQMR) algorithm [13] is employed to avoid the complicated multiplication between the transpose of the system matrix and a vector, resulting in a much simpler computer implementation. Moreover, the number of FFTs is reduced to only six per iteration. It is observed that the TFQMR-FFT method yields excellent results even for highly inhomogeneous dielectric objects.

II. Formulation

Consider the problem of scattering by a lossy inhomogeneous dielectric object with a complex permittivity

$$\epsilon(\mathbf{x}) = \epsilon_r(\mathbf{x})\epsilon_0 - j\frac{\sigma(\mathbf{x})}{\omega} \quad (1)$$

where ϵ_r denotes the relative permittivity and σ denotes the electric conductivity of the

object, which is in a free-space having a permittivity ϵ_0 . The incident electric field is denoted as $\mathbf{E}^{inc} = (E_1^{inc}, E_2^{inc}, E_3^{inc})^T$. The scattering problem can be formulated as the following domain integral equation over the object domain \mathbf{V} :

$$\mathbf{E}^{inc}(\mathbf{x}) = \frac{\mathbf{D}(\mathbf{x})}{\epsilon(\mathbf{x})} - (k_0^2 + \nabla \nabla \cdot) \mathbf{A}(\mathbf{x}), \quad \mathbf{x} \in \mathbf{V} \quad (2)$$

where $k_0 = \omega \sqrt{\epsilon_0 \mu_0}$ and

$$\mathbf{A}(\mathbf{x}) = \frac{1}{\epsilon_0} \int_{\mathbf{V}} G(\mathbf{x} - \mathbf{x}') \chi(\mathbf{x}') \mathbf{D}(\mathbf{x}') d\mathbf{x}' \quad (3)$$

with

$$\chi(\mathbf{x}) = \frac{\epsilon(\mathbf{x}) - \epsilon_0}{\epsilon(\mathbf{x})}, \quad G(\mathbf{x} - \mathbf{x}') = \frac{\exp(-jk_0|\mathbf{x} - \mathbf{x}'|)}{4\pi|\mathbf{x} - \mathbf{x}'|}.$$

To discretize this equation, we place the object in a uniform mesh with grid widths of Δx_1 , Δx_2 , and Δx_3 in the x_1 , x_2 , and x_3 directions, respectively. Therefore, the object is modelled approximately as a collection of small grids. The center of each grid is denoted as $\mathbf{x}_{M,N,P} = \{(M - \frac{1}{2})\Delta x_1, (N - \frac{1}{2})\Delta x_2, (P - \frac{1}{2})\Delta x_3\}$ and within each grid the complex permittivity is assumed to be constant with value $\epsilon_{M,N,P} = \epsilon(\mathbf{x}_{M,N,P})$.

To convert (2) into a matrix equation, we expand the generalized electric flux density and the electric-contrast vector potential as

$$\mathbf{D}(\mathbf{x}) = \epsilon_0 \sum_{q=1}^3 \sum_{I,J,K} d_{I,J,K}^{(q)} \Psi_{I,J,K}^{(q)}(\mathbf{x}), \quad \mathbf{x} \in \mathbf{V} \quad (4)$$

$$\mathbf{A}(\mathbf{x}) = \sum_{q=1}^3 \sum_{I,J,K} A_{I,J,K}^{(q)} \Psi_{I,J,K}^{(q)}(\mathbf{x}), \quad \mathbf{x} \in \mathbf{V} \quad (5)$$

where $\Psi_{I,J,K}^{(1)}(\mathbf{x})$, $\Psi_{I,J,K}^{(2)}(\mathbf{x})$, $\Psi_{I,J,K}^{(3)}(\mathbf{x})$ are vector volumetric rooftop functions in x_1 , x_2 and x_3 directions, respectively [10], [11]. We then apply the Galerkin's testing formulation to (2) and obtain

$$\begin{aligned} \langle \Psi_{M,N,P}^{(q)}(\mathbf{x}), \mathbf{E}^{inc}(\mathbf{x}) \rangle &= \langle \Psi_{M,N,P}^{(q)}(\mathbf{x}), \frac{\mathbf{D}(\mathbf{x})}{\epsilon(\mathbf{x})} \rangle - k_0^2 \langle \Psi_{M,N,P}^{(q)}(\mathbf{x}), \mathbf{A}(\mathbf{x}) \rangle \\ &\quad + \langle \nabla \cdot \Psi_{M,N,P}^{(q)}(\mathbf{x}), \nabla \cdot \mathbf{A}(\mathbf{x}) \rangle \end{aligned} \quad (6)$$

for $q = 1, 2, 3$, where $\langle \cdot \rangle$ denotes the inner product of two vector functions. Substituting (4) and (5) into (6), we obtain the following weak form of domain integral equation

$$[e_{M,N,P}^{inc,(p)}] = [u_{M,N,P;I,J,K}^{(p,q)}][d_{I,J,K}^{(q)}] - [k_0^2 v_{M,N,P;I,J,K}^{(p,q)} - w_{M,N,P;I,J,K}^{(p,q)}][A_{I,J,K}^q] \quad (7)$$

where

$$\begin{aligned} e_{M,N,P}^{inc,(p)} &= \langle \Psi_{M,N,P}^{(p)}, \mathbf{E}^{inc} \rangle, \quad u_{M,N,P;I,J,K}^{(p,q)} = \langle \Psi_{M,N,P}^{(p)}, \frac{\epsilon_0}{\epsilon(\mathbf{x})} \Psi_{I,J,K}^{(q)} \rangle, \\ v_{M,N,P;I,J,K}^{(p,q)} &= \langle \Psi_{M,N,P}^{(p)}, \Psi_{I,J,K}^{(q)} \rangle, \quad w_{M,N,P;I,J,K}^{(p,q)} = \langle \nabla \cdot \Psi_{M,N,P}^{(p)}, \nabla \cdot \Psi_{I,J,K}^{(q)} \rangle. \end{aligned}$$

The relationship between $d_{M,N,P}^{(q)}$ and $A_{M,N,P}^{(q)}$ can be found by substituting (4) and (5) into (3), yielding

$$\begin{aligned} A_{M,N,P}^{(q)} &= \Delta V \sum_{M',N',P'} G_{M-M',N-N',P-P'} \chi_{M',N',P'}^{(q)} d_{M',N',P'}^{(q)} \\ &= \Delta V DFT^{-1} \{ DFT\{G_{M,N,P}\} \cdot DFT\{\chi_{M,N,P}^{(q)} d_{M,N,P}^{(q)}\} \} \end{aligned} \quad (8)$$

where $\Delta V = \Delta x_1 \Delta x_2 \Delta x_3$. Substituting (8) into (7), we obtain a system of linear algebraic equations, which can be symbolically written as

$$\mathbf{e}^{inc} = \mathbf{L} \mathbf{d}. \quad (9)$$

The formulation described above was first proposed by Zwamborn and van den Berg [10]. Its major advantage is the simplicity in treating the singularity of the integrals in (2) and, more important, in calculating the right-hand side of (7), which is accomplished through two stages. The first stage is to calculate $A_{M,N,P}^{(q)}$ from (8) and the second stage is to substitute it into (7). Note that the matrices implied in (7) are sparse matrices and their product with a vector can be evaluated with $O(N_T)$ operations, where N_T denotes the number of unknowns. Although the matrix implied in (8) is a dense matrix, the computation of its product with a vector can be evaluated with $O(N_T \log N_T)$ operations with the aid of the FFT.

III. TFQMR-FFT Iterative Algorithm

Once (9) is formulated, its solution yields a numerical solution to the original problem. However, since the number of unknowns in (9) is usually very large, its solution using a direct solver, such as Gaussian elimination and LU decomposition method, is basically impractical, because a direct solver has a memory requirement of $O(N_T^2)$ and computational complexity of $O(N_T^3)$. This difficulty can be circumvented by solving (9) using an iterative solver and in each iteration the required matrix-by-vector product is evaluated using the FFT, as pointed out earlier. In the past, the CG and BCG methods have been employed as such an iterative solver, and the resultant methods are referred to as the CG-FFT and BCG-FFT methods [5]–[12]. The use of these methods reduces the memory requirement to $O(N_T)$ and computational complexity to $O(N_{iter} N_T \log N_T)$, where N_{iter} denotes the number of CG or BCG iterations. However, both CG-FFT and BCG-FFT algorithms require the calculation of a matrix-by-vector product with the conjugate transpose of the system matrix, which is not an easy task since the system matrix in (9) is nonsymmetric. Furthermore, the CG method has a problem of slow convergence although it converges monotonically, and the BCG method does not guarantee convergence although it usually

converges quickly. Although this problem can be alleviated by using the quasi-minimal residual (QMR) method [14], which converges monotonically with a convergence rate similar to the BCG method, the QMR still requires the calculation of a matrix-by-vector product with the conjugate transpose of the system matrix. Here, we consider other alternatives.

There are four algorithms that do not require the calculation of the transpose of the system matrix. The first one is the conjugate gradient squared (CGS) algorithm [15], which is the transpose-free variant of the BCG algorithm. However, like the BCG method, it also exhibits a rather irregular convergence behavior with wild oscillations in residual norm and does not guarantee convergence. The second method is the BCG stabilized (BCGSTAB) algorithm [16], which uses local steepest descent steps to obtain a more smoothly convergent CGS-like process. While this algorithm seems to work well in many cases, it still exhibits the irregular convergence behavior for some difficult problems. Also, its convergence is considerably slower than the CGS algorithm. The third method is the transpose-free QMR (TFQMR) method [13]. This algorithm can be implemented easily by changing only a few lines in the standard CGS algorithm. However, unlike the CGS algorithm, the iterations of the TFQMR algorithm are characterized by a quasi-minimization of the residual norm. This leads to smooth convergence with a convergence rate similar to the CGS algorithm. The TFQMR algorithm can be considered as a new version of the CGS algorithm which “quasi-minimizes” the residual in the space spanned by the vectors generated by the CGS iterations. Recently, a QMR variant of the BCGSTAB algorithm (QMRBCGSTAB) [17] is proposed. Our experimental calculation shows, however, that its convergence can be slower than the TFQMR for our problems. After a comprehensive comparison, the TFQMR algorithm is chosen for this work.

The TFQMR algorithm for solving (9) is given as follows [13], [18]:

1. Compute $\mathbf{w}_0 = \mathbf{u}_0 = \mathbf{r}_0 = \mathbf{e}^{inc} - \mathbf{L}\mathbf{d}_0$, $\mathbf{v}_0 = \mathbf{L}\mathbf{u}_0$, $\mathbf{g}_0 = 0$;
2. $\tau_0 = \|\mathbf{r}_0\|$, $\theta_0 = \eta_0 = 0$
3. Choose \mathbf{r}_0^* such that $\rho_0 \equiv \langle \mathbf{r}_0^*, \mathbf{r}_0 \rangle \neq 0$.
4. For $m = 0, 1, 2, \dots$, until convergence Do:
5. If m is even then
6. $\alpha_{m+1} = \alpha_m = \rho_m / \langle \mathbf{v}_m, \mathbf{r}_0^* \rangle$
7. $\mathbf{u}_{m+1} = \mathbf{u}_m - \alpha_m \mathbf{v}_m$
8. Endif
9. $\mathbf{w}_{m+1} = \mathbf{w}_m - \alpha_m \mathbf{L}\mathbf{u}_m$
10. $\mathbf{g}_{m+1} = \mathbf{u}_m + (\theta_m^2 / \alpha_m) \eta_m \mathbf{g}_m$
11. $\theta_{m+1} = \|\mathbf{w}_{m+1}\|_2 / \tau_m$; $c_{m+1} = (1 + \theta_{m+1}^2)^{-\frac{1}{2}}$
12. $\tau_{m+1} = \tau_m \theta_{m+1} c_{m+1}$; $\eta_{m+1} = c_{m+1}^2 \alpha_m$
13. $\mathbf{d}_{m+1} = \mathbf{d}_m + \eta_{m+1} \mathbf{g}_{m+1}$

14. If m is odd then
15. $\rho_{m+1} = \langle \mathbf{w}_{m+1}, \mathbf{r}_0^* \rangle; \beta_{m-1} = \rho_{m+1} / \rho_{m-1}$
16. $\mathbf{u}_{m+1} = \mathbf{w}_{m+1} + \beta_{m-1} \mathbf{u}_m$
17. $\mathbf{v}_{m+1} = \mathbf{L} \mathbf{u}_{m+1} + \beta_{m-1} (\mathbf{L} \mathbf{u}_m + \beta_{m-1} \mathbf{v}_{m-1})$
18. Endif
19. EndDo

The residual norm of the approximate solution \mathbf{d}_m is given by $\|\mathbf{r}_m\| \leq (m+1)^{\frac{1}{2}} \tau_m$. From the algorithm, it is easy to see that each odd iteration requires two matrix-by-vector products and each even iteration does not require a matrix-by-vector product. Therefore, on average the TFQMR algorithm requires only one matrix-by-vector product, which can be calculated using six FFTs.

IV. Numerical Results

To demonstrate the accuracy of the TFQMR-FFT algorithm, we analyze the scattering of a plane wave from two layered dielectric spheres and compare the results with the Mie series solution. In all simulations, we assume that the incident plane wave is polarized in the x_1 direction and propagates in the x_3 direction. The amplitude of the incident electric field is 1 V/m. The first sphere has two layers, whose inner layer has a radius $a_1 = 0.075$ m and $\epsilon_{1r} = 72.0 - j161.779$ and the outer layer has a radius $a_2 = 0.15$ m and $\epsilon_{2r} = 7.5 - j8.9877$. The frequency is 100 MHz. The second sphere has three layers, whose inner layer has a radius $a_1 = 0.3333\lambda_0$ and $\epsilon_{1r} = 1.2$, the middle layer has a radius $a_2 = 0.6667\lambda_0$ and $\epsilon_{2r} = 2.0$, and the outer layer has a radius $a_3 = \lambda_0$ and $\epsilon_{3r} = 2.4$. Figure 1 shows the field in the two-layer dielectric sphere and Fig. 2 gives the results for the three-layer sphere. The convergence criterion for these results is $rss = \|\mathbf{r}_m\| / \|\mathbf{r}_0\| < 10^{-3}$. Excellent agreement is observed between the exact solution and the numerical results obtained using $31 \times 31 \times 31$ grids. The relative error vs. the number of iterations is given in Fig. 3 for both cases for different grid sizes. As can be seen, the TFQMR-FFT algorithm exhibits a stable convergence behavior. The computation time needed to evaluate one iteration, the total number of unknowns, and the required computer storage are given in Table 1.

To demonstrate the efficiency of the algorithm, we consider again the problem illustrated in Fig. 1. As can be seen in Fig. 3(a), using the TFQMR-FFT algorithm with $31 \times 31 \times 31$ grids, it takes 112 iterations to reduce rss below 10^{-3} . Since each iteration requires six FFTs, the total number of FFTs is 672. This problem was also treated using the CG-FFT algorithm in [10] and the BCG-FFT algorithm in [11]. For the same grid size and accuracy, the CG-FFT algorithm takes about 360 iterations and, since each iteration requires 12 FFTs, the total number of FFTs is about 4320, which is 6.4 times that of the TFQMR-

Table 1: Computation Time and Storage on DEC Alpha

Mesh size	FFT size	Number of unknowns	CPU-time per iteration	Computer storage
$15 \times 15 \times 15$	$32 \times 32 \times 32$	10800	0.74 sec	2.2 Mb
$31 \times 31 \times 31$	$64 \times 64 \times 64$	92256	9.5 sec	16 Mb
$63 \times 63 \times 63$	$128 \times 128 \times 128$	762048	152 sec	105 Mb

FFT algorithm. When the BCG-FFT algorithm is used, it takes only 54 iterations and, since each iteration requires 18 FFTs, the total number of FFTs is 972, which is 1.4 times that of the TFQMR-FFT algorithm. Furthermore, the BCG-FFT algorithm has an irregular convergence behavior and does not guarantee convergence.

Finally, to demonstrate the capability of the TFQMR-FFT algorithm to treat strongly inhomogeneous dielectric object, we consider the plane wave scattering by a human head. The construction of the electromagnetic model of the head is discussed in [19] and the material property of the tissues of the head is given in [20]. The incident wave propagates in the $-x_3$ direction (from top) and the incident electric field is polarized in the x_1 direction (from the left ear to the right ear). The incident electric field has an amplitude of 1 V/m and the frequencies considered are 64 MHz and 256 MHz. The results are presented in the form of spatial absorption rate (SAR) defined as $SAR = \sigma|E|^2/2\rho$, where ρ denotes the density. Figures 4 and 5 show the SAR in the axial, sagittal, and coronal planes at the two frequencies. Figure 6 shows the relative error vs. the number of iterations for the two frequencies. Again, the TFQMR-FFT algorithm exhibits a stable convergence behavior.

VI. Conclusion

This paper presented a TFQMR-FFT algorithm for computing electromagnetic fields in a 3D arbitrarily-shaped, inhomogeneous dielectric body. It is observed that this algorithm yields excellent results and exhibits a very stable convergence behavior. Because of the use of the TFQMR method, the algorithm avoids the computation of the multiplication between the transpose of the system matrix and a vector, which is required in both the CG-FFT and BCG-FFT methods. As a result, the programming complexity is greatly reduced. Furthermore, since on average the TFQMR method requires only one matrix-by-vector multiplication, which can be evaluated using six FFTs, the TFQMR-FFT algorithm is more efficient than the currently available CG-FFT and BCG-FFT methods.

References

- [1] D. E. Livesay and K. M. Chen, "Electromagnetic fields induced inside arbitrarily shaped biological bodies," *IEEE Trans. Microwave Theory Tech.*, vol. 22, no. 12, pp. 1273-1280, 1974.
- [2] D. H. Schaubert, D. R. Wilton, and A. W. Glisson, "A tetrahedral modeling method for electromagnetic scattering by arbitrarily shaped inhomogeneous dielectric bodies," *IEEE Trans. Antennas Propagat.*, vol. 32, no. 1, pp. 77-85, 1984.
- [3] R. D. Graglia, P. L. E. Uslenghi and R. S. Zich, "Moment method with isoparametric elements for three-dimensional anisotropic scatters," *Proc. IEEE*, vol. 5, no. 7, pp. 750-760, 1989.
- [4] N. N. Bojarski, "K-Space formulation of the electromagnetic scattering problems," *Air Force Avionic Lab. Technical Report AFAL-TR-71-75*, 1971.
- [5] D. T. Borup and O. P. Gandhi, "Fast-Fourier transform method for calculation of SAR distributions in finely discretized inhomogeneous models of biological bodies," *IEEE Trans. Microwave Theory Tech.*, vol. 32, no. 4, pp. 355-360, 1984.
- [6] T. K. Sarkar, E. Arvas, and S. M. Rao, "Application of FFT and the conjugate gradient method for the solution of electromagnetic radiation from electrically large and small conducting bodies," *IEEE Trans. Antennas Propagat.*, vol. 34, no. 5, pp. 635-640, 1986.
- [7] J. M. Jin and J. L. Volakis, "A biconjugate gradient FFT solution for scattering by planar plates," *Electromagnetics*, vol. 12, no. 1, pp. 105-119, 1992.
- [8] M. F. Catedra, E. Gago, and L. Nuno, "A numerical scheme to obtain the RCS of three-dimensional bodies of size using the conjugate gradient method and the fast fourier transform," *IEEE Trans. Antennas Propagat.*, vol. 37, no. 5, pp. 528-537, 1989.
- [9] C. Y. Shen, K. J. Glover, M. I. Sancer, and A. D. Varvatsis, "The discrete Fourier transform method of solving differential-integral equations in scattering theory," *IEEE Trans. Antennas Propagat.*, vol. 37, no. 6, pp. 1032-1041, 1989.
- [10] P. Zwamborn and P. M. van der Berg, "The three-dimensional weak form of the conjugate gradient FFT method for solving scattering problems," *IEEE Trans. Microwave Theory Tech.*, vol. 40, no. 9, pp. 1757-1766, 1992.

- [11] H. Gan and W. C. Chew, "A discrete BCG-FFT algorithm for solving 3D inhomogeneous scattering problems," *J. Electromag. Wave Appl.*, vol. 9, no. 10, pp. 1339–1357, 1995.
- [12] J. H. Lin and W. C. Chew, "BiCG-FFT T-matrix method for the scattering solution from inhomogeneous bodies," *IEEE Trans. Microwave Theory Tech.*, vol. 44, no. 7, pp. 1150–1155, 1996.
- [13] R. W. Freund, "A transpose-free quasi-minimal residual algorithm for non-hermitian linear systems," *SIAM J. Sci. Comput.*, vol. 14, no. 2, pp. 470–482, 1993.
- [14] R. W. Freund and N. M. Nachtigal, "A quasi-minimal residual method for non-Hermitian linear systems," *Numer. Math.*, vol. 60, pp. 315–339, 1991.
- [15] P. Sonneveld, "CGS, a fast Lanczos-type solver for nonsymmetric linear systems," *SIAM J. Sci. Statist. Comput.*, vol. 10, pp. 36–52, 1989.
- [16] H. A. van Der Vorst, "BI-CGSTAB: A fast and smoothly converging variant of BI-CG for the solution of nonsymmetric linear systems," *SIAM J. Sci. Statist. Comput.*, vol. 13, pp. 631–644, 1992.
- [17] T. F. Chan, E. Gallopoulos, V. Simoncini, T. Szeto, and C. H. Tong, "A quasi-minimal residual variant of the BI-CGSTAB algorithm for nonsymmetric systems," *SIAM J. Sci. Comput.*, vol. 15, no. 2, pp. 338–347, 1994.
- [18] Y. Saad, *Iterative Method for Sparse Linear Systems*. New York: PWS Publishing Company, 1995.
- [19] P. J. Dimbylow and S. M. Mann, "SAR calculations in an anatomically realistic model of the head for mobile communication transceivers at 900 MHz and 1.8 GHz," *Phys. Med. Biol.*, vol. 39, pp. 361–368, 1994.
- [20] J. M. Jin, J. Chen, H. Gan, W. C. Chew, R. L. Magin, and P. J. Dimbylow, "Computation of electromagnetic fields for high-frequency magnetic resonance imaging applications," *Phys. Med. Biol.*, vol. 41, pp. 2719–2738, 1996.

Figure Captions

Fig. 1 The magnitude of the total electric field inside a two-layer dielectric sphere along the x_1 , x_2 , and x_3 axes. The inner layer has a radius $a_1 = 0.075$ m and $\epsilon_{1r} = 72.0 - j161.779$ and the outer layer has a radius $a_2 = 0.15$ m and $\epsilon_{2r} = 7.5 - j8.9877$ and the frequency is 100 MHz. The solid line is from the Mie series solution and the dash-dot line is from the TFQMR-FFT solution with grids $31 \times 31 \times 31$.

Fig. 2 The magnitude of the total electric field inside a three-layer dielectric sphere along the x_1 , x_2 , and x_3 axes. The inner layer has a radius $a_1 = 0.3333\lambda_0$ and $\epsilon_{1r} = 1.2$, the middle layer has a radius $a_2 = 0.6667\lambda_0$ and $\epsilon_{2r} = 2.0$, and the outer layer has a radius $a_3 = \lambda_0$ and $\epsilon_{3r} = 2.4$. The solid line is from the Mie series solution and the dash-dot line is from the TFQMR-FFT solution with grids $31 \times 31 \times 31$.

Fig. 3 The relative error vs. the number of iterations for different grid sizes. (a) For the case of the two-layer sphere. (b) For the case of the three-layer sphere.

Fig. 4 SAR (W/kg) in the axial, sagittal, and coronal slices at 64 MHz for a uniform plane wave excitation polarized in the x_1 direction and propagating in the $-x_3$ direction using $63 \times 63 \times 63$ grids.

Fig. 5 SAR (W/kg) in the axial, sagittal, and coronal slices at 256 MHz for a uniform plane wave excitation polarized in the x_1 direction and propagating in the $-x_3$ direction using $63 \times 63 \times 63$ grids.

Fig. 6 The relative error vs. the number of iterations for different frequencies with $63 \times 63 \times 63$ grids. (a) For the case of 64 MHz. (b) For the case of 256 MHz.

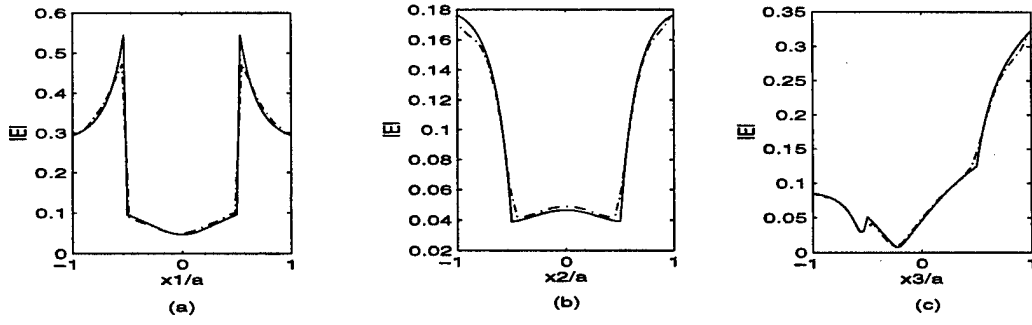


Figure 1: The magnitude of the total electric field inside a two-layer dielectric sphere along the x_1 , x_2 , and x_3 axes. The inner layer has a radius $a_1 = 0.075$ m and $\epsilon_{1r} = 72.0 - j161.779$ and the outer layer has a radius $a_2 = 0.15$ m and $\epsilon_{2r} = 7.5 - j8.9877$ and the frequency is 100 MHz. The solid line is from the Mie series solution and the dash-dot line is from the TFQMR-FFT solution with grids $31 \times 31 \times 31$.

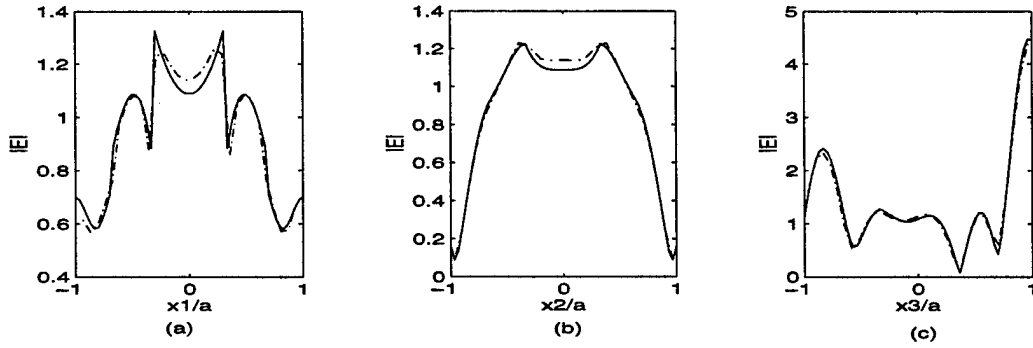


Figure 2: The magnitude of the total electric field inside a three-layer dielectric sphere along the x_1 , x_2 , and x_3 axes. The inner layer has a radius $a_1 = 0.3333\lambda_0$ and $\epsilon_{1r} = 1.2$, the middle layer has a radius $a_2 = 0.6667\lambda_0$ and $\epsilon_{2r} = 2.0$, and the outer layer has a radius $a_3 = \lambda_0$ and $\epsilon_{3r} = 2.4$. The solid line is from the Mie series solution and the dash-dot line is from the TFQMR-FFT solution with grids $31 \times 31 \times 31$.

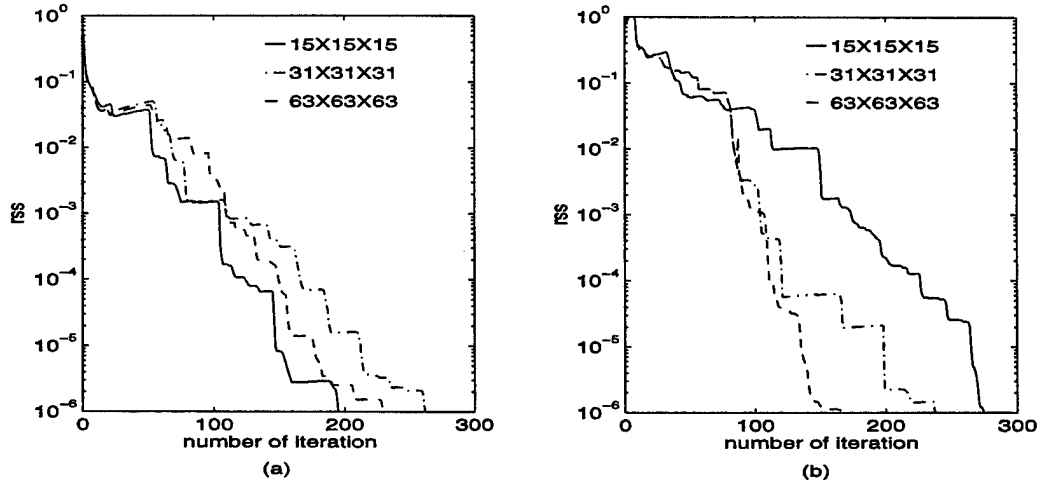


Figure 3: The relative error vs. the number of iterations for different grid sizes. (a) For the case of the two-layer sphere. (b) For the case of the three-layer sphere.

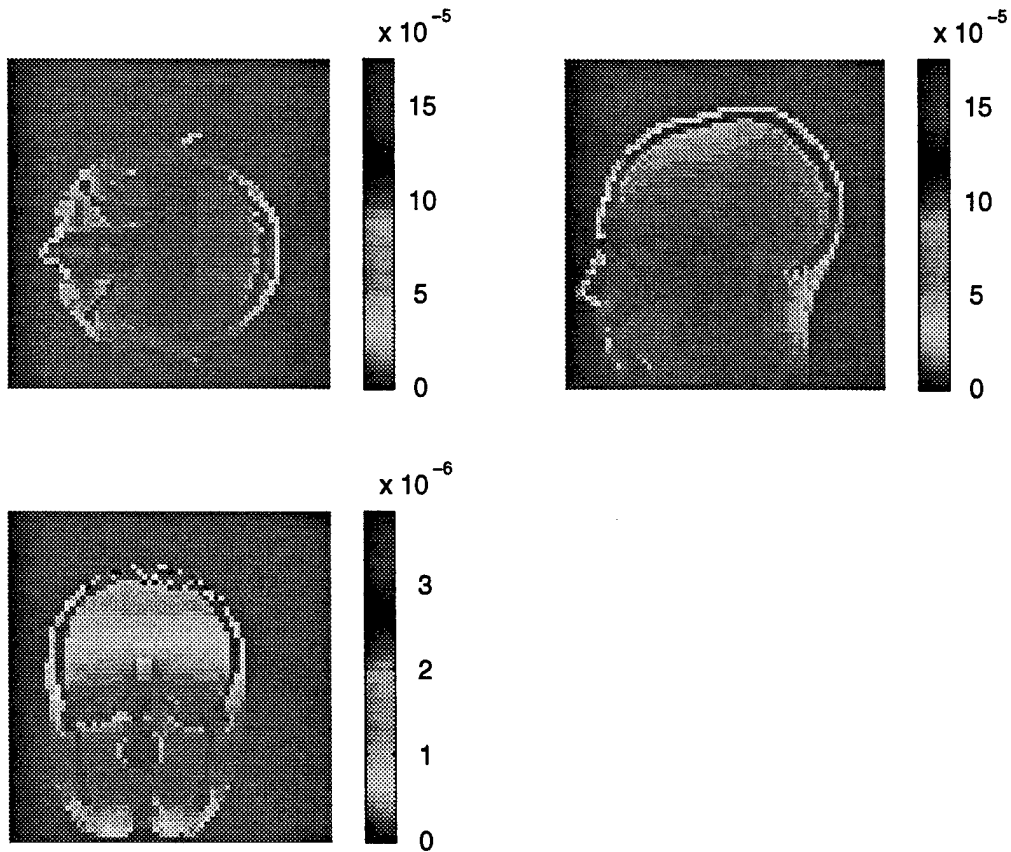


Figure 4: SAR (W/kg) in the axial, sagittal, and coronal slices at 64 MHz for a uniform plane wave excitation polarized in the x_1 direction and propagating in the $-x_3$ direction using $63 \times 63 \times 63$ grids.

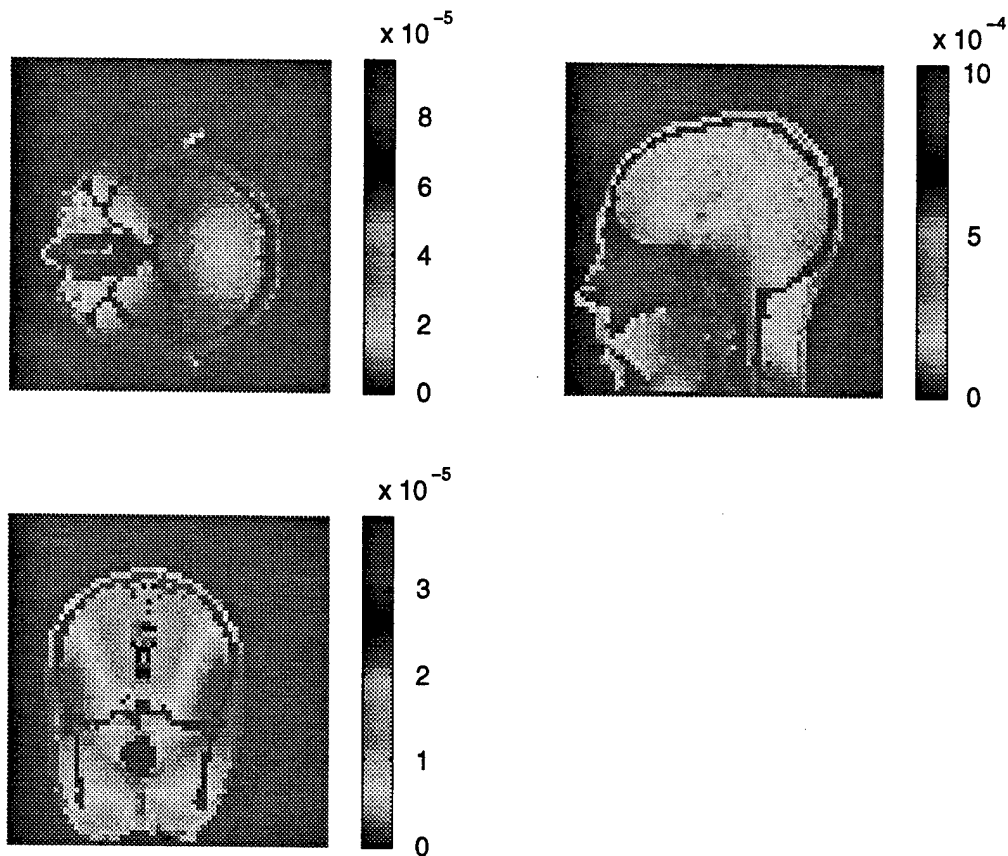


Figure 5: SAR (W/kg) in the axial, sagittal, and coronal slices at 256 MHz for a uniform plane wave excitation polarized in the x_1 direction and propagating in the $-x_3$ direction using $63 \times 63 \times 63$ grids.

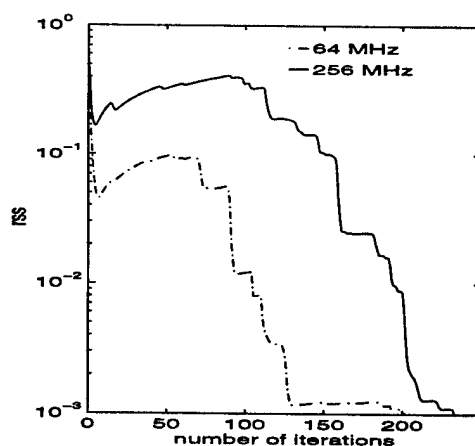


Figure 6: The relative error vs. the number of iterations for different frequencies with $63 \times 63 \times 63$ grids. (a) For the case of 64 MHz. (b) For the case of 256 MHz.